Optimized Implementation of Secondary Shielding for Irregular Fields Treated ON A 4MV Linear Accelerator

by

Mazen A. Soubra

A Thesis

presented to the University of Manitoba

in partial fulfillment of the requirements

for the degree of

Master of Science

in

Department of Physics

January 1984

OPTIMIZED IMPLEMENTATION OF SECONDARY SHIELDING FOR IRREGULAR FIELDS TREATED ON A 4MV LINEAR ACCELERATOR

by

Mazen A. Soubra

A thesis submitted to the Faculty of Graduate Studies of the University of Manitoba in partial fulfillment of the requirements of the degree of

MASTER OF SCIENCE

TO MY MOTHER AFAF AND MY WIFE SANDRA

ACKNOWLEDGEMENTS

I would like to thank my supervisor Mrs. Karen Breitman for her assitance and support,George Sandison for his advice and help ,Dr. Gerd Froese for his criticism and Dr.Shlomo Shalev for his permission to use the facilities at the Medical Physics Department.
This work was partly funded by Manitoba Health Research Council.

ABSTRACT

The effectiveness of lead acrylic as an electron filter has been demonstrated for a 4 MV photon beam. It has been shown to be less effective than lead glass for reducing surface and build-up doses and far superior to acrylic. Lead acrylic exhibits physical characteristics comparable with acrylic making it suitable for use as a shadow tray or shielding block bridge. Build-up curves superior to open beam conditions may be produced with a lead acrylic tray placed at a tray to skin distance between 30 and 40 cm. The magnitude of scattered radiation from acrylic and lead acrylic supporting trays outside the field boundary was measured as a function of distance outside the field boundary, depth in a phantom, field size, and tray to skin (phantom surface) distance. The penumbra formed by the edge of lead blocks used for shielding in large irregular fields has been measured for a diverging and straight edge blocks. Results show the dominant factor affecting penumbra size is the block to skin distance. The major effect of block edge shape is the location of the 50% dose level relative to the geometrical edge. The optimum block to skin distance for reducing penumbra size without a significant increase in the skin dose was found to be between 30 and 40 cm.

CONTENTS

List of Figures

List of Tables

Table

Chapter 1. Introduction

1.1 INTRODUCTION TO RADIOTHERAPY

Radiotherapy treatment for malignant disease involves the application of radiation beams to areas of known disease and to suspected avenues of spread so as to deliver a lethal dose to all cancer cells. At the same time, the radiation dose to normal tissues must be minimized to reduce radiation injury. High energy photon beams are commonly used because of their deep penetration into tissue and the skin sparing attributes of these beams.

Figure 1.1 illustrates the variation of dose occurring along the central axis of a high energy photon beam. The maximum dose occurs at a depth d_{max} rather than at the surface (skin-sparing effect). An exponential decrease in dose beyond d_{max} results from the attenuation of the radiation by tissue. The slope is characteristic of the effective beam energy used. The region from the surface to the depth d_{max} is called the build-up region. It is described further in Chapter 5. The characterization of this region depends on the design of the treatment head (Chapter 2) and on the location and composition of other materials (e.g. for shielding) placed in the beam.

Figure 1.2 illustrates a dose profile across the beam at constant depth d, for a radiation field size S. Note, however, that the region S' in which tumoricidal doses are achieved (90% - 100%) is smaller. Healthy tissue in the region irradiated by the penumbra receives between 90% and 20% of the maximum dose.

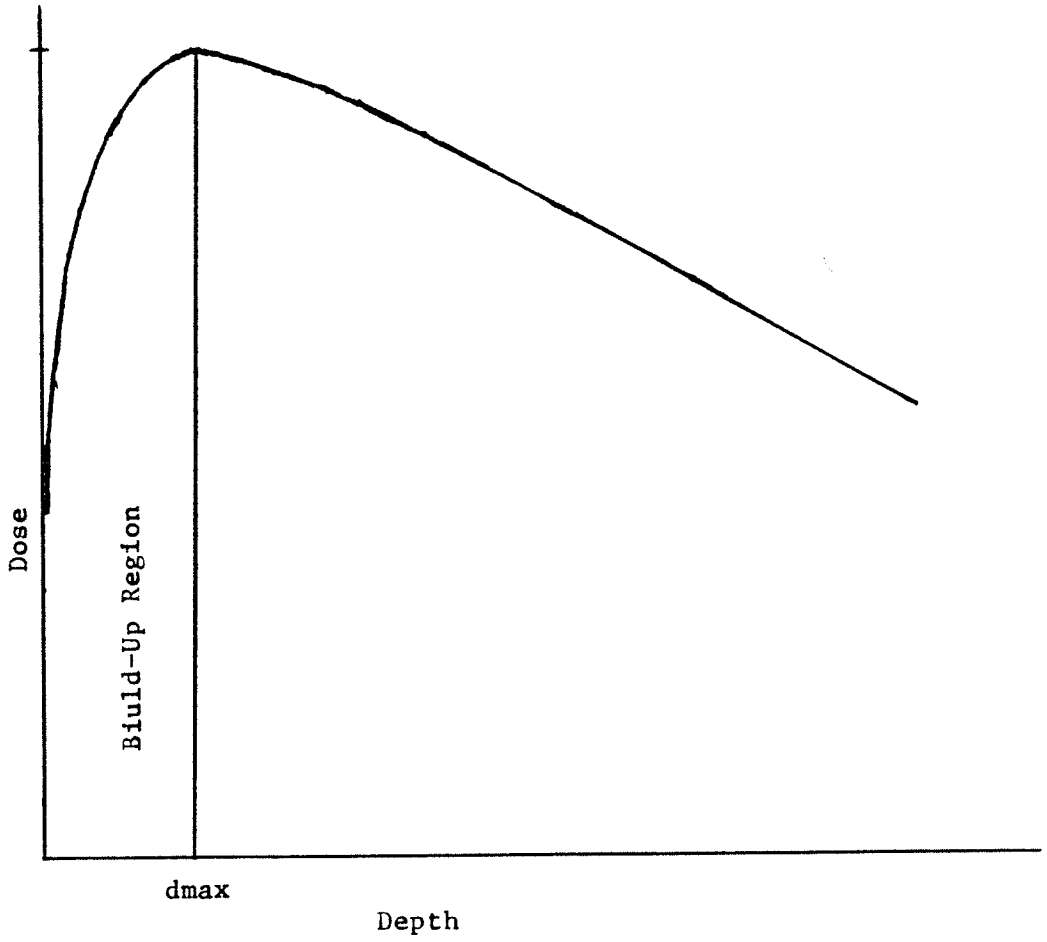

Figure 1.1 The variation of dose with depth in a material occuring along the central axis of a high energy beam.

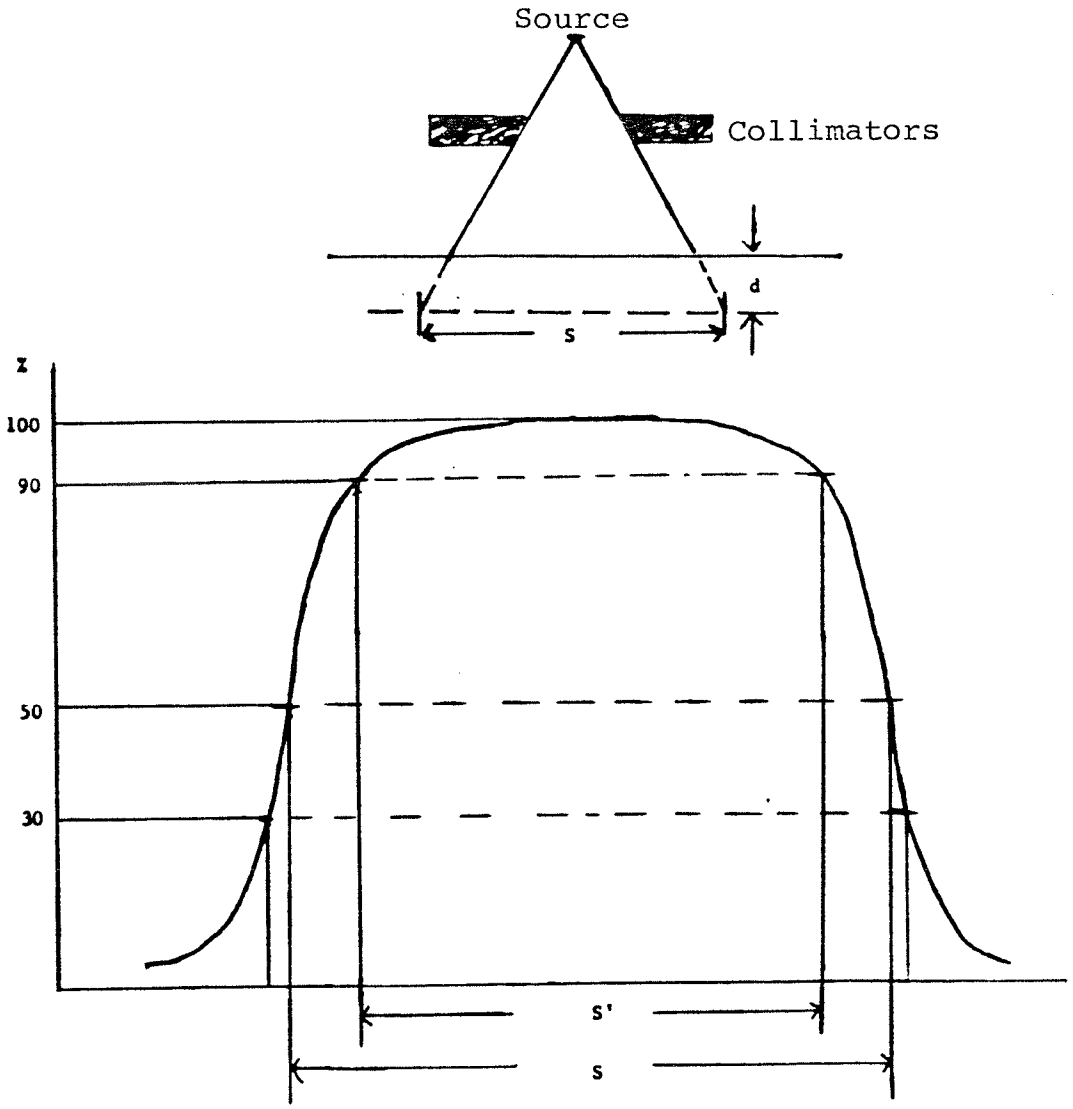

Figure 1.2 Dose profile across the beam at constant depth d.

Figure 1.3 illustrates the use of a large irregularly shaped radiation field, referred to as a Mantle field, used to treat Hodgkin's disease. The entire lymph node system above the diaphragm must be irradiated while at the same time preserving lung function. This is achieved by placing individually designed lead shielding blocks in the beam to shield part of the lungs and the larynx.

In order to obtain the large field sizes required for this type of treatment, the distance from the x-ray source to the skin (SSD) must be larger than the normally used distance of 80 cm.

1.2 OBJECT OF THIS WORK

It is the object of this work to investigate the conditions necessary to improve the characteristics of the x-ray beam by:

(a) reducing the dose in the build-up region

(b) reducing the width of the penumbra region around shielding blocks.

As will be discussed in later chapters, an improvement in one parameter often results in a degradation of the other. Therefore, an optimized condition must be determined.

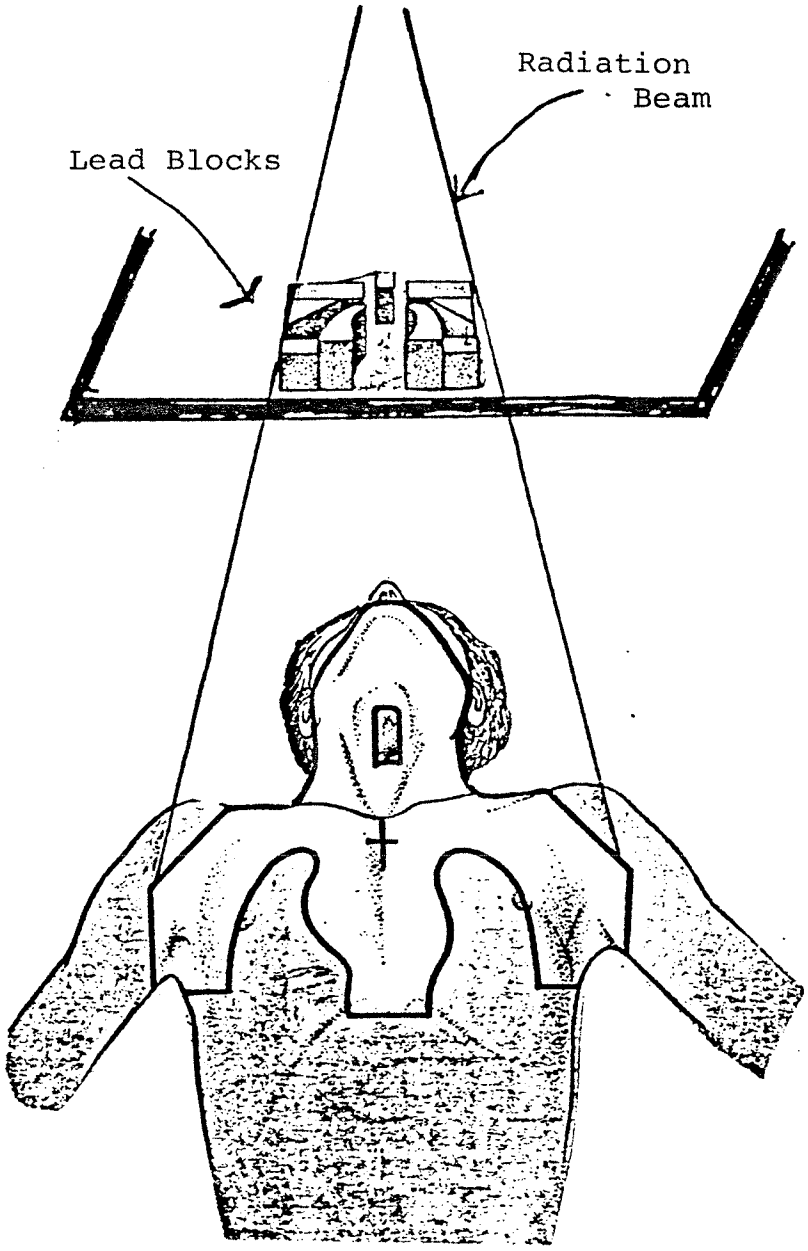

Figure 1.3 The figure shows a typical 'mantle' field set-up.Individually designed lead block are placed in a large radiation field to shield radiation sensitive area from the radiation beam.Bright sights seen on the patient are the treatment areas.

Chapter 2. The 4MV Medical Linac

2.1 PHYSICAL DESCRIPTION

The photon beam used in this work was produced by a medical electron linear accelerator (linac), the Therapi 4, manufactured commercially by SHM Nuclear Corporation and operating at 4 MV. An overall view of the Therapi 4 system is shown in Figure 2.1. The central console is physically located outside the treatment room. The boom assembly, which houses the electron gun, accelerator structure, magnetron and beam handling system is attached to the modulator cabinet. The modulator cabinet is located in the treatment room and houses the accelerator high voltage circuits, the freon bottle and the water supply controls.

2.2 ELECTRON LINAC OPERATION

The electron linear accelerator is a device which uses microwave power to accelerate electrons to high energies. The electrons travel through the device in a straight line. X-rays (bremsstrahlung) are produced when the high energy electrons are incident on a high Z target.

The Therapi 4 linac has a standing wave accelerator structure that consists of a linear array of microwave cavities resonant at 3000 MHz. Microwave power produced by a magnetron is fed into the structure and sets up electric fields within the cavities. The summation of the electric fields produced by the forward and the reflected waves gives rise to an alternating electric field pattern which is spatially stationary along the structure.

THE 4MV LINAC

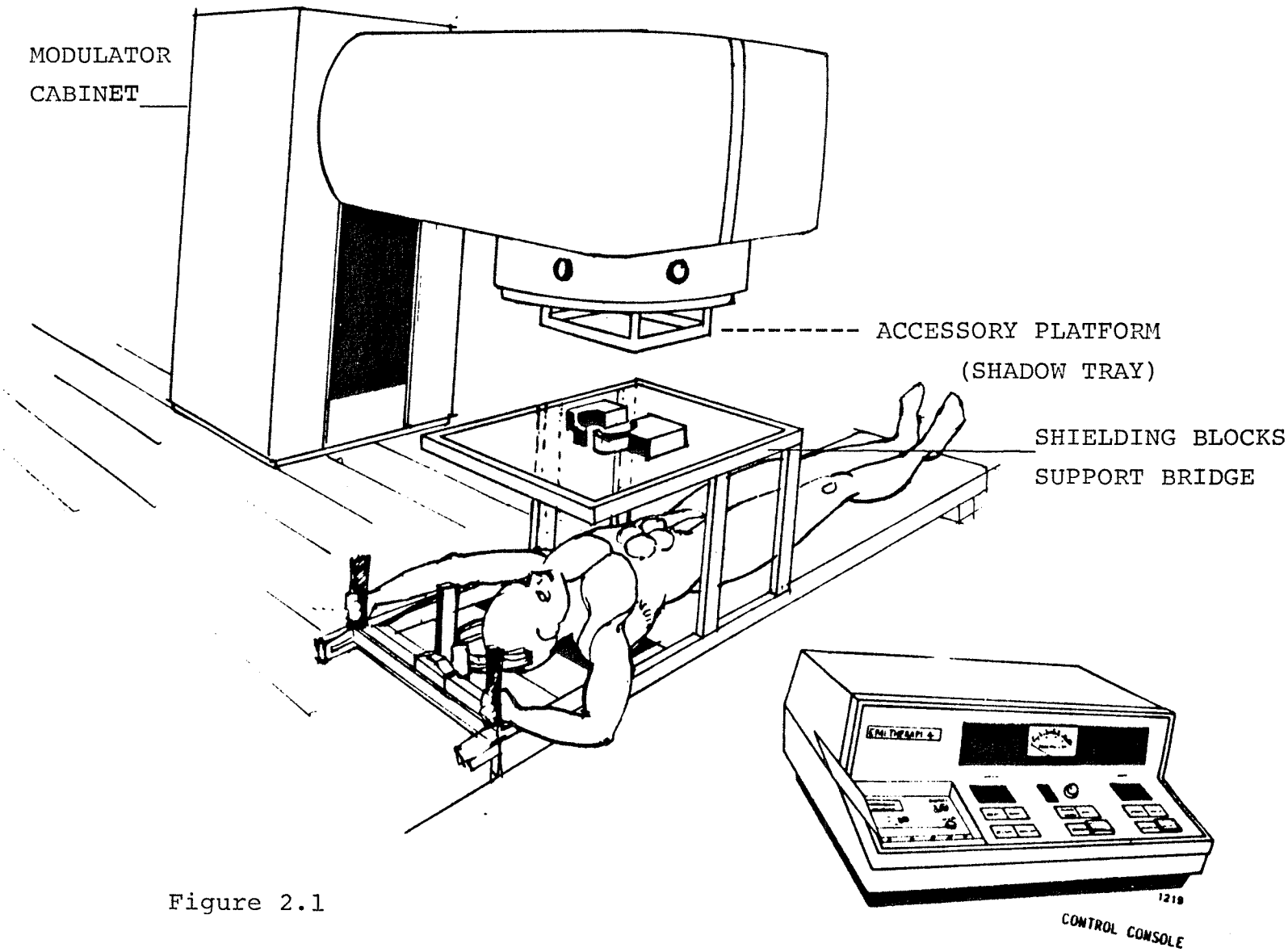

Figure 2.1

An electron gun injects electrons into a buncher cavity which is situated at the beginning of the accelerating structure. In this cavity the electrons are accelerated to a velocity approaching the speed of light and grouped into bunches. Electron bunches with the correct velocity will be in phase with the alternating electric field and will experience only the accelerating electric field during its passage through the linear array of cavities.

2.3 THE X-RAY TREATMENT BEAM

The 4 MV linac produces a parallel beam of 4 MeV electrons, approximately 3 mm in diameter. Bremsstrahlung x-rays are produced when the electron beam is incident on the high Z target. This target is attached to the end of the accelerator structure in a straight through design and is water cooled. The thickness of the target is large enough to stop most of the incident electrons. The x-ray intensity is forward peaked as shown in Figure 2.2. The x-ray output is approximately 0.01 cGY per radiation pulse at a distance of 80 cm in air from the target with a pulse rate equal to 240 per second. This output is monitored by an ion chamber (Figure 2.3).

Radiation therapy requires a treatment beam that satisfies the following conditions:

(a) Well defined limits to the treatment beam

(b) A relatively uniform and known distribution of intensity of radiation within the beam and

(c) Minimum radiation outside the beam.

Components required to satisfy these conditions are shown in Figure 2.3 and are situated in the x-ray treatment head.

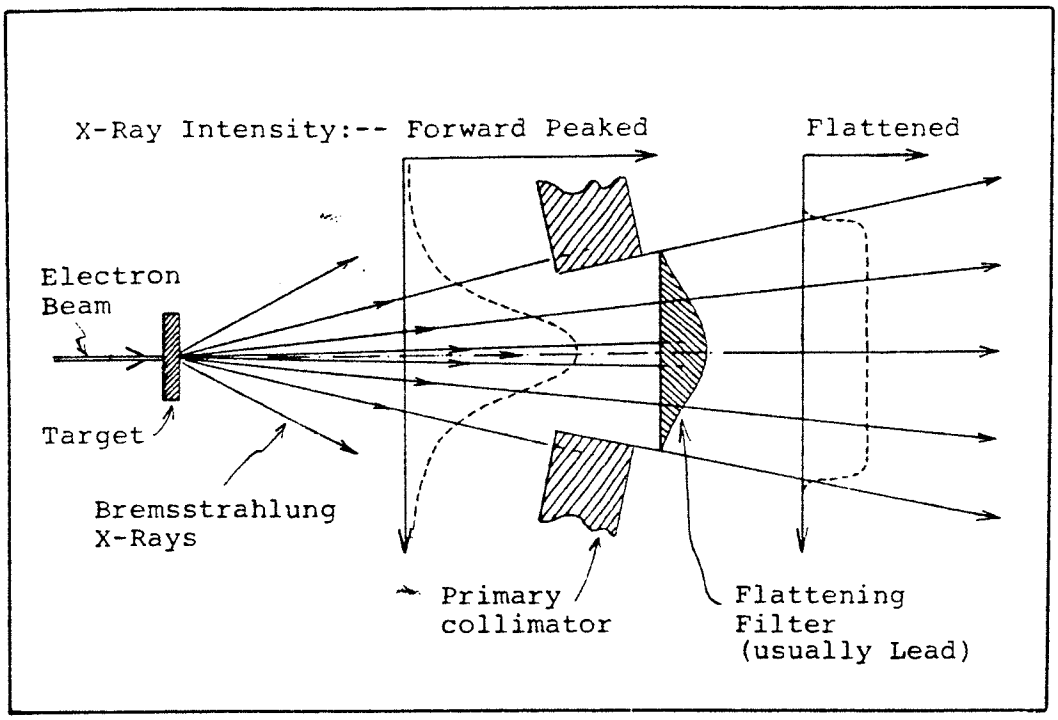

Figure 2.2 X-ray Production

2.3.1 X-ray Treatment Head

Figure 2.3 illustrates schematically the components of the x-ray treatment head for the 4 MV linac. The accelerator structure is mounted in the treatment head collinear with components associated with producing, controlling and monitoring a clinically useful beam of x-rays.

2.3.2 Primary Collimator

Primary collimation of the treatment beam occurs immediately beyond the x-ray target. A fixed high Z collimator is accurately positioned relative to the central axis of the beam to prevent asymmetry. This collimator determines the maximum size of the useful treatment beam for a given SSD.

2.3.3 Field Flattener

To ensure a relatively uniform beam intensity over a cross sectional area, an x-ray flattening filter made of lead is inserted in front of the primary collimator. The flattening filter resembles a conical shape (Figure 2.2) and provides considerable attenuation to the forward peak beam intensity with minimum attenuation to off-axis beam intensity. It is designed to produce optimim field flatness at a depth of 10 cm. The 4 MV linac provides a uniform ($\pm$3%) field over the central 80% of a 32 cm x 32 cm field size at 80 cm SSD. Therefore for a treatment area greater than 25 cm x 25 cm uniform irradiation can only be achieved by increasing SSD.

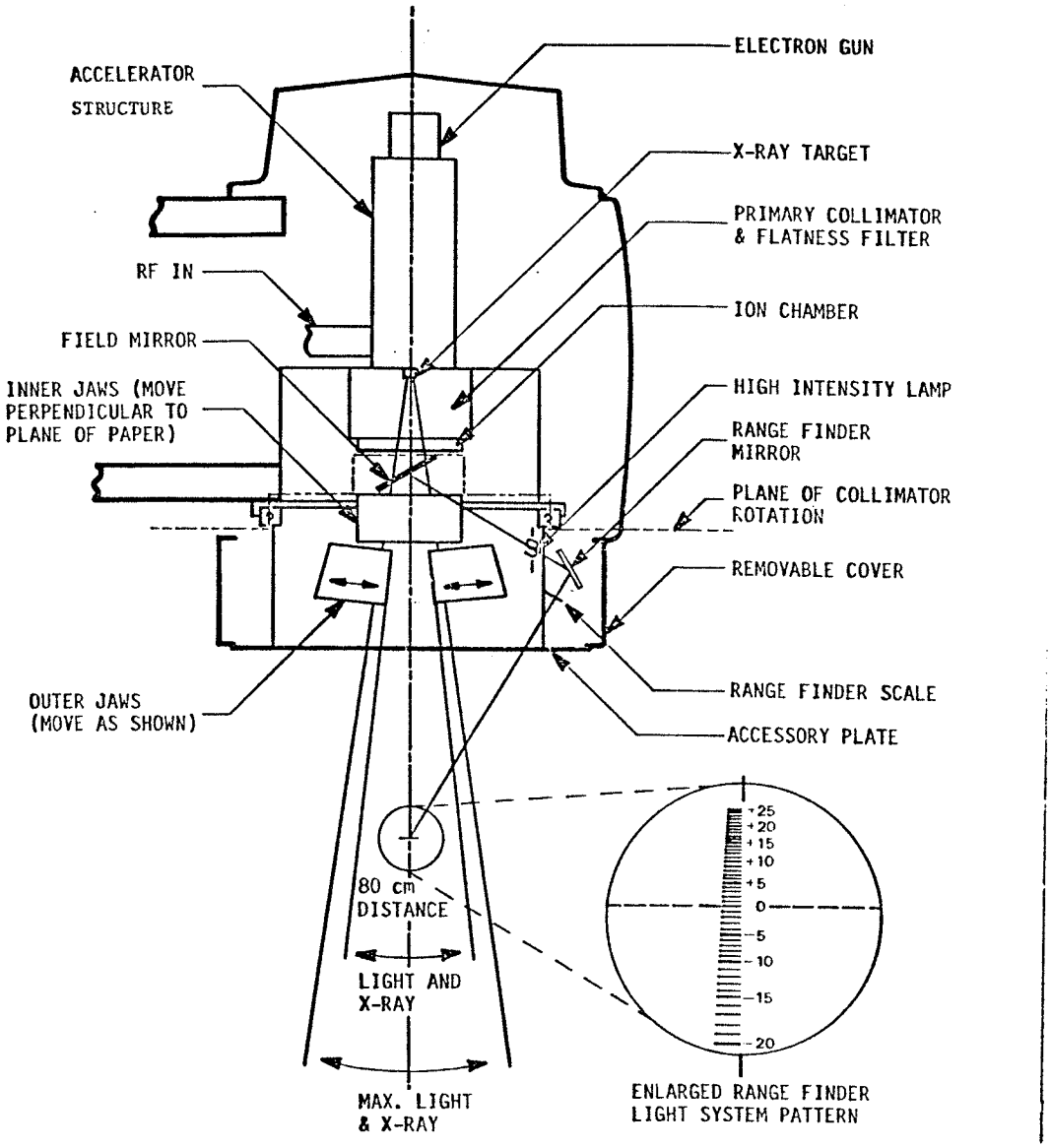

Figure 2.3 X-ray head detail arrangement

2.3.4 X-Ray Field Collimator

Field size definition is provided by two pairs of collimator jaws (Figure 2.3). To help provide sharp edges for treatment fields, the movement of each collimator jaw is confined to an arc so that the collimator face follows the beam divergence. The field size is indicated by a field illumination system with cross hairs provided to indicate the center of field.

2.3.5 Accessory Platform

Figure 2.1 indicates the accessory platform. This acts as a holder for beam modifying devices which are placed in the path of the beam in order to produce isodose surfaces of a specific shape, to screen off certain parts of the patient or to compensate for the modifying effect of the patient contour.

2.4 ADDITIONAL COMPONENTS FOR LARGE SOURCE SKIN DISTANCE TECHNIQUES

For treatments using large irregular shaped fields the patient surface is usually positioned at 150 cm or 160 cm SSD. A special couch is provided with a bridge attached. This bridge provides support for the individually designed lead shielding blocks (Figure 2.1).

2.5 SPECTRAL DISTRIBUTION OF 4 MV X-RAYS

No measured 4 MV spectra are available for the different 4 MV linear accelerators in clinical use. However, calculated spectra using various methods, such as Monte Carlo or an attenuation analysis (see Figure 2.4), are presently published for 4 MV photon beams (HUA). Figure 2.4 shows the different spectra for a 4 MV beam calculated by various methods.

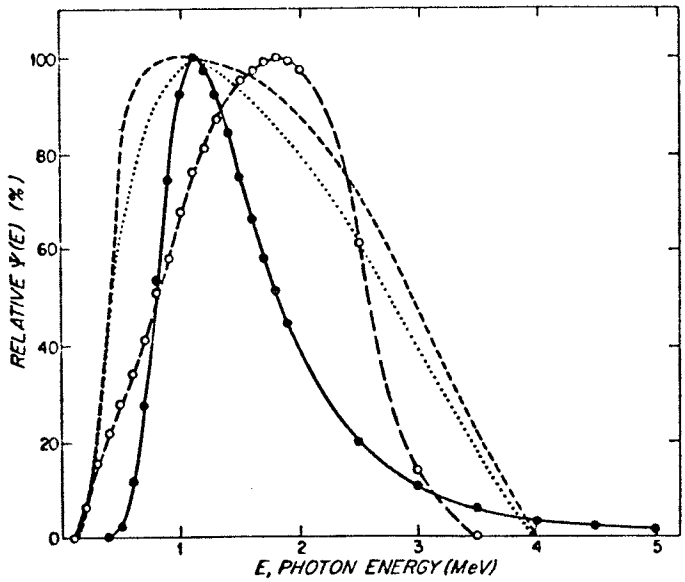

Figure 2.4 Relative energy fluence as a function of photon energy for 4MV linac.Solid curve and long dashed curve are determined by attenuation analysis method.The short dashed spectrum is extrapolated from measured spectrum of higher energy linacs.The dotted spectrum is calculated by Monte Carlo method.
Reproduced from Huang et al. (HUA.)

Chapter 3. Interaction of Photons and Electrons with Matter

3.1 PHOTON INTERACTIONS

Photons are electromagnetic radiations that are involved in the production of energetic secondary particles, positrons or electrons, upon interacting with matter. It is the interaction of these charged particles with matter that imparts energy to the absorbing material, through the ionization and excitation of atoms and the breaking of molecular bonds in the absorber. Chemical changes and therefore biological damage will occur when the absorbing medium is human tissue.

In the photon energy domain of 0.01 to 30 MeV, photons interact with an absorber to produce high speed electrons by three distinct mechanisms known as the photoelectric effect, the Compton effect and pair production.

3.1.1 Photoelectric Effect

In the photoelectric process illustrated in Figure 3.1, a photon with energy $h\nu$ collides with an atom and ejects one of the bound electrons from K, L, M or N shells. The ejected electron is called a photoelectron and emerges with energy $h\nu - E_s$ where E_s is the binding energy of the shell from which the electron is ejected. For high energy photons, the photoelectrons tend to be ejected in the forward direction. Following photoelectron emission a vacancy is created which is filled by transitions from other shells. The transitions result in the isotropic emission of photons called "characteristic radiation" of energies E_K-E_L, E_K-E_M, etc. Altern-

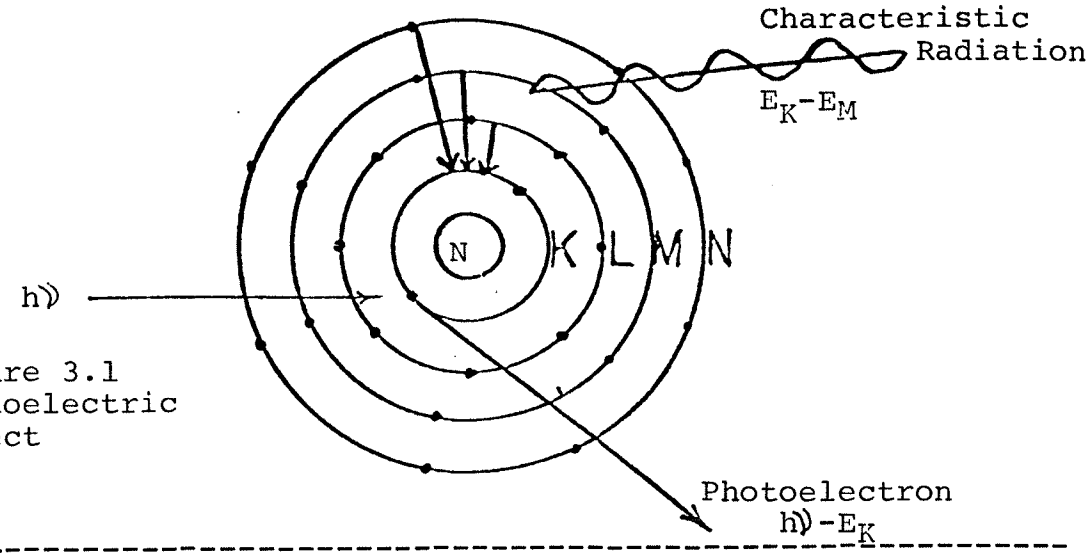

Figure 3.1
Photoelectric
Effect

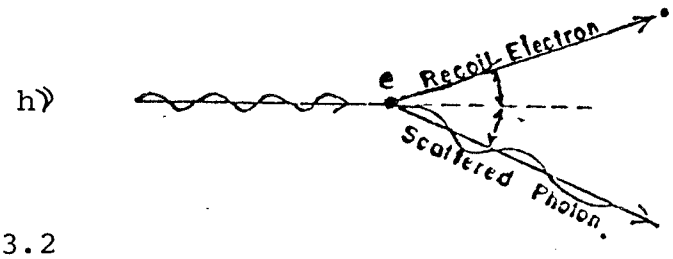

Figure 3.2
Compton Effect

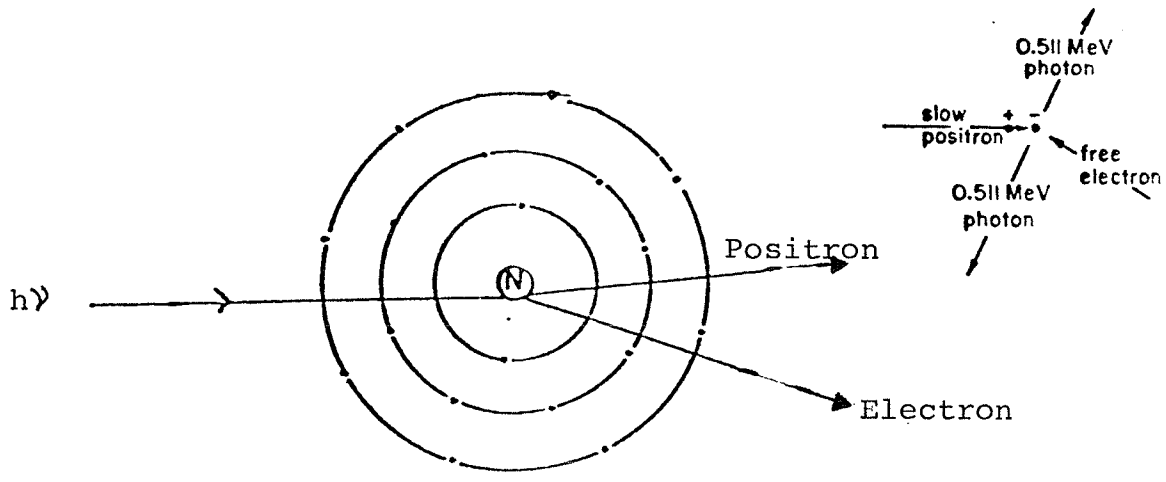

Figure 3.3 Pair Production

atively, in a process favored for low Z materials, an Auger electron may be ejected from the atom with energy $E_K - E_L - E_M$ for example.

3.1.2 Variation of Photoelectric Effect with Atomic Number and Energy

The variation of the mass attenuation coefficient for photoelectric interactions, τ/ρ (cm^2g^{-1}) as a function of photon energy is shown in Figure 3.4 for water and lead, representative of low and high Z materials respectively.

For water, τ/ρ varies with about $1/h\nu^3$

For lead, τ/ρ varies with about $1/h\nu^3$ between the sharp discontinuities for energies less than 1 MeV. At very high energies the coefficient varies as $h\nu$.

The sharp discontinuities or absorption edges appear at photon energies equal to binding energies of the atomic shells and subshells.

3.1.3 Energy Transfer in the Photoelectric Effect

In the photoelectric process for low Z material the photoelectron acquires an energy approximately equal to the incident photon energy, since the binding energy for low Z materials is small. The resulting characteristic radiation is of low energy and is therefore absorbed locally. For high Z material the energy transfer to the photoelectron is less and the energy of the characteristic radiation is much greater in comparison to low Z materials, resulting in distant deposition of the characteristic radiation energy.

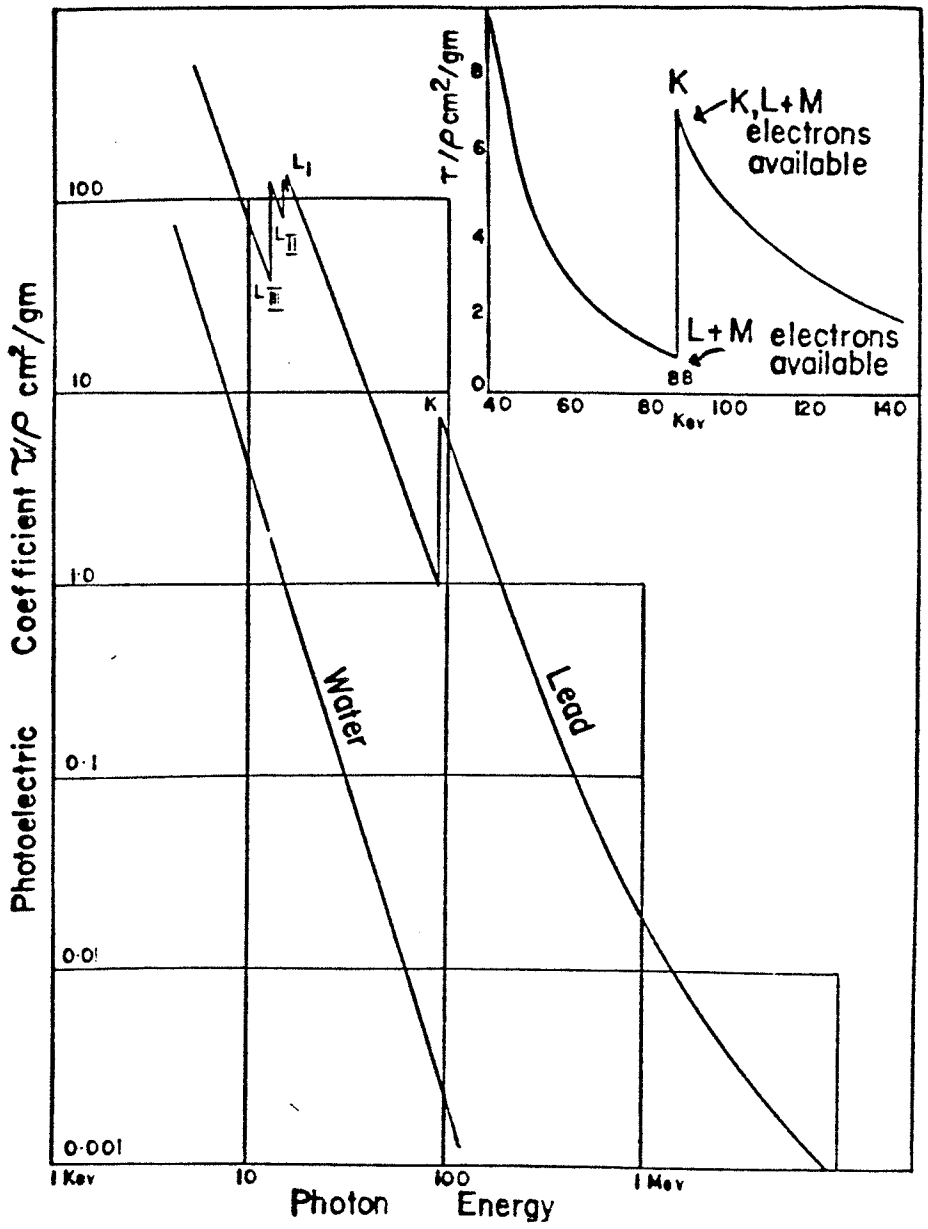

Figure 3.4 Photoelectric mass attenuation coefficient in lead and water as a function of photon energy.

Reproduced from Johns and Cummingham (JO.)

3.1.4 Compton Effect

In a Compton collision as shown in Figure 3.2, an incident photon of energy $h\nu$ collides with an unbound or free electron (i.e. incident photon energy is much greater than the binding energy of the atomic electron) to produce a recoil electron at an angle θ with kinetic energy E and a scattered photon with reduced energy $h\nu'$ at an angle ϕ.

Considerations of conservation of momentum and energy may be applied to derive a relationship between $h\nu$, ϕ, E and $h\nu'$ (EV.)

$$E = h\nu \cdot \alpha \frac{(1-\cos\phi)}{1+\alpha(1-\cos\phi)} \qquad (3.1)$$

$$h\nu' = h\nu \cdot \frac{1}{1+\alpha(1-\cos\phi)} \qquad (3.2)$$

$$\cot\theta = (1+\alpha)\tan\frac{\phi}{2} \qquad (3.3)$$

where $\alpha = h\nu/MoC^2$ and MoC^2 = 0.511 MeV, the rest mass energy of an electron.

The probability of photon scattering at angle ϕ was calculated by Klein-Nishina (JO.) using quantum mechanical considerations. A graph of this equation (Figure 3.5) for various photon energies (JO.) illustrates preferred scattering in the forward directions for photon energies of interest in this work.

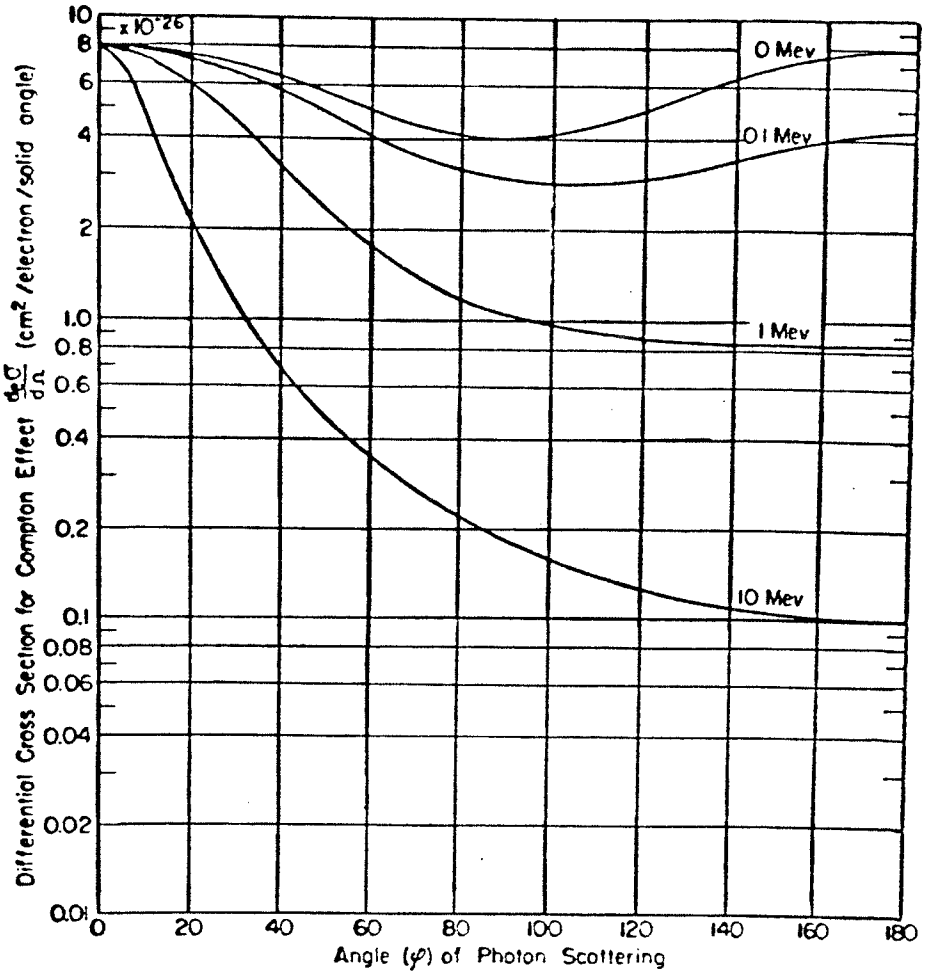

Figure 3.5 Klein-Nishina differential cross section for various photon energies.
Reproduced from Johns and Cummingham (JO.)

3.1.5 Total Compton Cross Sections

The total probability that a photon will interact with a free electron is given by (EV.)

$$ {}_e\sigma = 2\pi r_0^2 \left\{ \frac{1+\alpha}{\alpha^2}\left[\frac{2(1+\alpha)}{1+2\alpha} - \frac{\ln(1+2\alpha)}{\alpha} \right] + \frac{\ln(1+2\alpha)}{2\alpha} - \frac{1+3\alpha}{(1+2\alpha)^2} \right\} \quad cm^2 electron^{-1} \tag{3.4} $$

where r_o is the classical electron radius and is equal to 2.81794 x 10^{-13}cm.

The total energy scattering cross section ${}_e\sigma_s$, which deals with the scattered photon energy $h\nu'$, is smaller than ${}_e\sigma$ by this amount

$$ {}_e\sigma_s = \frac{h\nu'}{h\nu} {}_e\sigma \tag{3.5} $$

The total energy transfer coefficient, ${}_e\sigma_{tr}$, is simply given by

$$ {}_e\sigma_{tr} = {}_e\sigma - {}_e\sigma_s \tag{3.6} $$

and represents the probability for the recoil kinetic energy, E, to be imparted to an electron in the course of a Compton collision.

Figure 3.6 shows the variation of ${}_e\sigma$, ${}_e\sigma_s$ and ${}_e\sigma_{tr}$ with photon energy (50.).

The scatter coefficient ${}_e\sigma_s$, is equal to the total coefficient at photon energies less than 0.01 MeV, since at these energies the photon is scattered with nearly the same energy as the incident photon

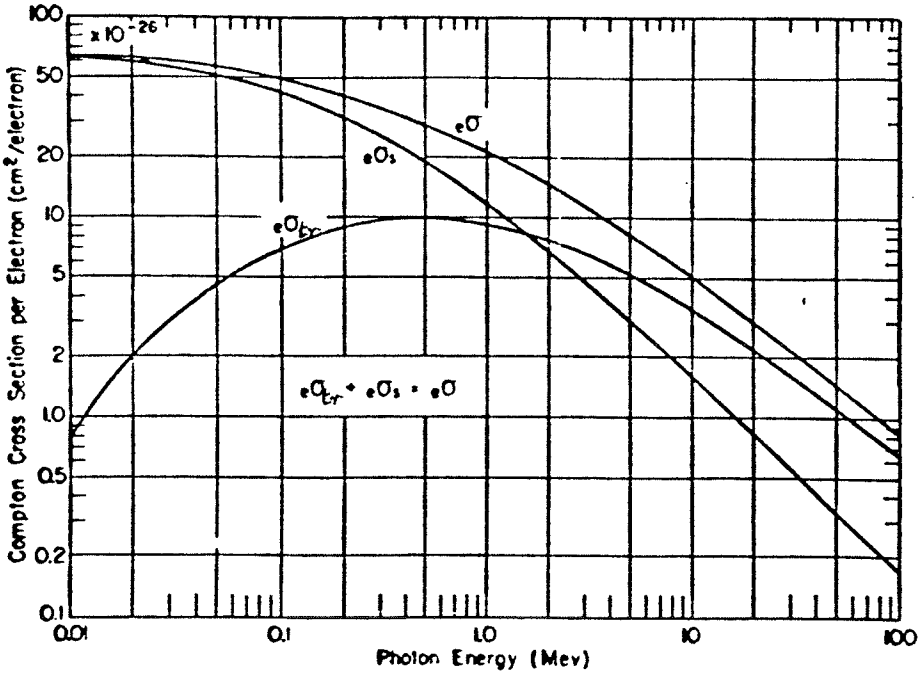

Figure 3.6 The total Compton coefficient $_e\sigma$, the scatter coefficient $_e\sigma_s$ and the transfer coefficient as a function of photon energy.

Reproduced from Johns and Cummingham(JO.)

and the recoil electron gets little energy. At very high energies $\sigma_s \ll \sigma_a$ since at these energies the scattered photon gets very little energy.

3.1.6 Dependence of Compton Effect on Z

Since the Compton process involves free electrons and since most materials have approximately the same number of electrons per gram, the probability of a Compton interaction is independent of atom number Z. Hence, all materials absorb essentially the same amount of radiation per electron and per gram from this process.

3.1.7 Pair Production

In the field of the nucleus of an atom, as shown in Figure 3.3, a photon may be totally absorbed and a positron-electron pair produced. A minimum incident photon energy $2\ m_o c^2$ or 1.022 MeV is required for pair production. The remaining energy $h\nu$ - 1.022 MeV is shared between the positron and the electron.

Pair production is accompanied by the emission of annihilation radiation consisting of two 0.511 MeV photons ejected in essentially opposite directions, produced when a low energy combines with a free electron (Figure 3.3). Triplet production may occur in the field of an orbital electron. The minimum energy needed for this process is $4\ Mo c^2$ = 2.04 MeV. Figure 3.7 (J01.) illustrates the variation of pair production cross-section K with photon energy and atomic number Z.

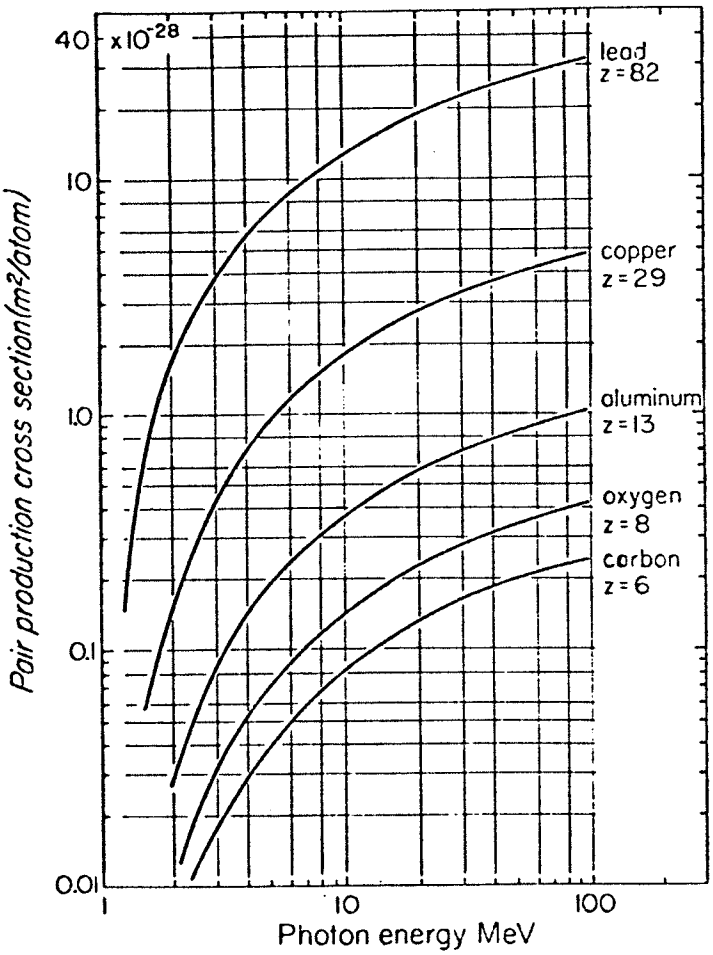

'Figure 3.7 Pair production cross section for various material as a function of photon energy.

Reproduced from Johns and Cummingham (JO1.)

3.1.8 Relative Importance of the Three Mechanisms

Figure 3.8 summarizes the relative importance of the principal interactions, photoelectric effect, Compton effect and pair production, over a broad range of photon energies and absorbers. The lines are obtained by plotting the values of energy and atomic number for which the cross-sections of two processes are equal.

For low Z materials such as soft tissues, Compton effect is dominant over a wide range of photon energies. For intermediate and high Z materials the photoelectric is dominant for low energy and pair production interaction is dominant at high energy.

3.2 INTERACTION OF ELECTRONS WITH MATTER

Electrons incident on an absorber lose energy by essentially three processes, namely:

(a) Inelastic scattering by atomic electrons (Collision losses)

(b) Elastic scattering by atoms (Multiple scattering)

(c) Inelastic nuclear scattering with emission of bremsstrahlung (Radiation losses).

In case (a) the energy of the electron is attenuated by a multitude of inelastic collisions with orbital electrons until thermal levels are reached. In these inelastic collisions excitation and ionization of the atoms in the medium will occur. Some of the secondary electrons energized along the track of the primary electron will have sufficient energy to produce ionizations (delta tracks).

In case (b) the electrons moving in the medium are deflected as a result of their interaction with the electric fields of the nuclei

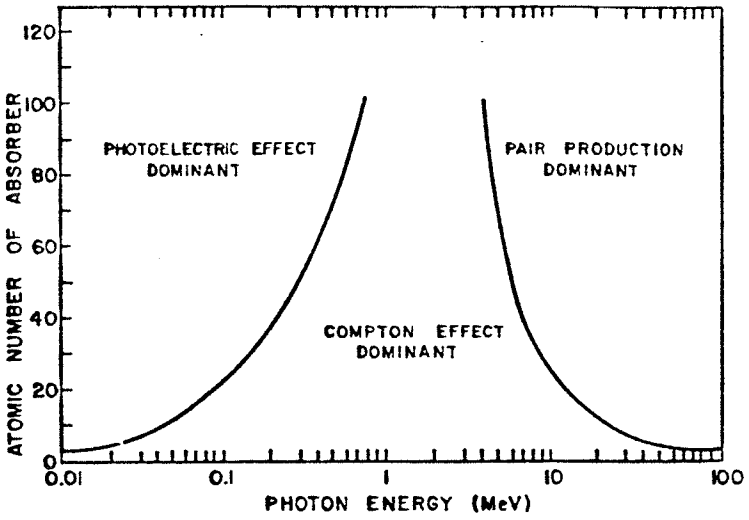

Figure 3.8 Relative importance of the three principle photon interactions over a broad range of photon energies and absorbers.
Reproduced from Evans (EV.)

and orbital electrons. Because of their light mass, electrons are easily deflected and experience frequent elastic scattering. In passing through a foil electrons experience many single elastic scattering events (multiple scattering) which results in a net angle of scattering. The mean square angle of $\overline{\theta^2}$, is obtained in a statistical treatment of the single scattering events. An approximate relation for $\overline{\theta^2}$ is (Hll.)

$$\overline{\theta^2} = \frac{4\pi N Z(Z+1)e^4 t}{p^2 v^2} \cdot \log\left[4\pi Z^{4/3} N t \left(\frac{\hbar}{m_0 v}\right)^2\right] \qquad (3.7)$$

Where:

N is the number of atoms per cubic centimeter = N_o /A

t is the foil thickness in grams per square centimeter

Z atomic number of material

e is the electron charge

p is the electron momentum

v velocity of electron

h is Plank's constant divided by 2

The mean square angle is seen to vary approximately as Z^2 and E^{-2}. Equation 3.7 has been approximately represented (Hll.). with the following simple numerical formulas for lead and air.

$$\overline{\theta^2} \sim \frac{6\times10^8}{E^2} \cdot d \qquad \text{(Lead)}$$

$$\overline{\theta^2} \sim \frac{7\times10^3}{E^2} \cdot d \qquad \text{(Air)}$$

Where d is the thickness of material in cm and E is the kinetic energy of the incident electrons in KeV.

In case (c), electromagnetic radiation, bremsstrahlung, with a continuous energy spectrum is emitted when electrons experience a sudden decceleration in the field of the nucleus. The amount of energy lost by an electron as radiation per unit length is approximately proportional to its energy and to the square of the nuclear charge (Z^2). Characteristic radiation may also be emitted as a result of ionization of inner orbital electrons.

3.3 SECONDARY ELECTRON EMISSION FROM VARIOUS ATOMIC NUMBER MATERIALS

Whenever photons are absorbed by a layer of material, secondary electrons are produced. If the layer of material has a thickness comparable with the range of the secondary electrons or even thicker, the original energy and intensity distribution of the secondary electrons will be altered considerably. The secondary electrons will lose energy by collision and radiation processes and will change their direction of passage through the absorber as a result of single and multiple nuclear scattering (see section 2.2).

The variation in the number of secondary electrons emitted from various materials in the forward and backward directions is the combined result of the different photon cross sections and the different magnitude of electron scattering in the material (HI.). The scattering probability is proportional to $N(Z^2+Z)$ or $1/A.(Z^2+Z)$. N is the number of atoms per cubic centimeter and is equal to $No\rho/A$ where No is Avogadro's number, ρ the density of the material and A is the atomic

mass. (See Equation 3.7). With the approximation Z/A = constant, the scattering of electrons is proportional to (Z + 1) of the medium (HI.).

In 1951 Hine (HI.) performed the first systematic study of the effect for various atomic numbers and gamma energies on forward and back scattered secondary electron emission. His work agreed with the above theoretical analysis and his results are shown in Figures 3.9 and 3.10. Figure 3.9 shows the effect of atomic number on backscattered secondary electron emission for χ-rays of various nuclides. The rapid increase in backscattering emissions observed with increasing log (Z + 1) is due to the production of photoelectrons in addition to the Compton electrons. This effect is pronounced for lower energy gamma rays.

The emission of secondary electrons in the forward direction is shown in Figure 3.10. Because of the increased backscattering with increasing Z, the intensity of Compton electrons emitted in the forward direction decreases with log (Z + 1), reaching minimum levels for intermediate Z materials. For high atomic number materials the additional emission of photoelectrons again becomes apparent.

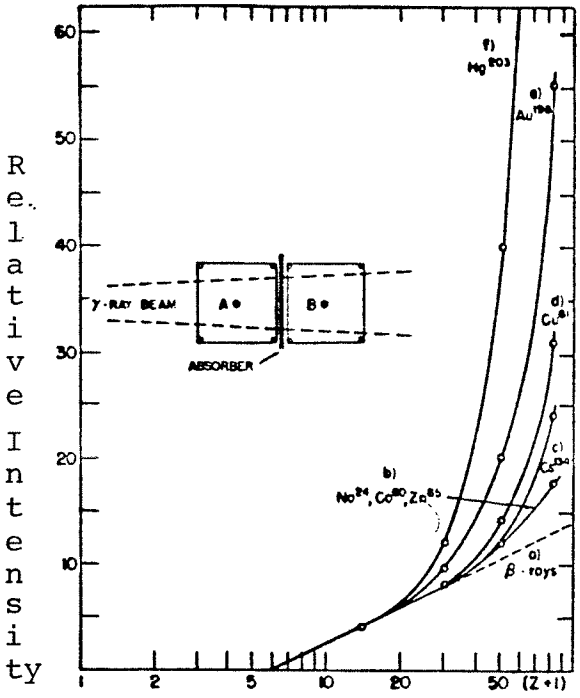

Figure 3.9 Effect of atomic number on backscattered secondary electron emission for x-rays of various nuclides.

Reproduced from Hine (HI.)

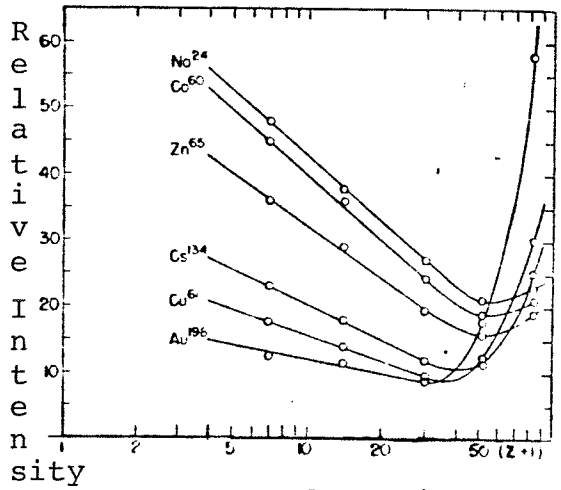

Figure 3.10 Effect of atomic number on forward secondary electron emmission.

Chapter 4. Measurement of Radiation Dose

4.1 UNIT OF DOSE

The quantity of ionizing radiation, expressed in terms of the amount of radiation energy imparted to a medium, is the 'absorbed dose'. Absorbed dose D, is defined by ICRU (IC.) as:

$$D = \frac{d\bar{E}}{dm} \tag{4.1}$$

$\overline{dE}$ is the mean energy imparted by the ionization to a mass, dm, of matter.

The special name for the unit of absorbed dose is the Gray (Gy) where 1 Gy = 1 $JKg.^{-1}$.

In this work relative dose rather than absolute dose was measured. Dose measurements were made using ionization chambers and thermoluminescent dosimeters (TLDS).

4.2 IONIZATION DOSIMETRY

4.2.1 Basis of Ionization Measurements

The absorbed dose, D, in an irradiated medium in the immediate vicinity of a small gas filled cavity may be determined from the ionization in the cavity by the Bragg-Gray equation (IC1):

$$D = J_g (\bar{W}/e) \bar{S}_{mg} \tag{4.1}$$

Where

Jg is the ratio of the ionization charge by the mass of gas.

$\overline{W}$ is the average energy expended by electrons in the gas per ion pair formed,

e is the elementary charge, and

$\bar{S}_{mg}$ is a weighted mean ratio of the mass collision stopping power of the medium to that of gas for the incident x-ray spectrum and its resulting secondary electron spectrum.

The gas ionization chamber is essentially a gas cavity of known volume surrounded by a solid wall. When photons are absorbed either in the chamber wall or in the medium surrounding the chamber, secondary electrons are set in motion which lose their energy by ionization of the medium and the gas in the cavity.

The total number of charge pairs produced in the gas volume is proportional to the total energy absorbed in the volume and consequently to the absorbed dose within the medium. Application of a potential difference across the gas in the chamber results in charge separation and collection. An electrometer connected to the electrodes is used to measure the quantity of charge produced. The gas cavity may be spherical, cylindrical, disc-shaped, etc., the choice governed by the intended use.

4.2.2 Characteristic of the Ionization Chamber Employed

In this work, build-up region and skin dose measurements were made with a parallel plate chamber with a thin (2.3 mg cm^{-2}) graphited plastic film window and 1.5 mm electrode separation. The sensitive volume (air) is approximately 0.3 cm^3 (Nuclear Enterprises Model 2536), Figure 4.1). The chamber body is made of acrylic. The ionization chamber was connected to a Keithly 610 digital electrometer and was operated at 300V DC. At this operating voltage the chamber

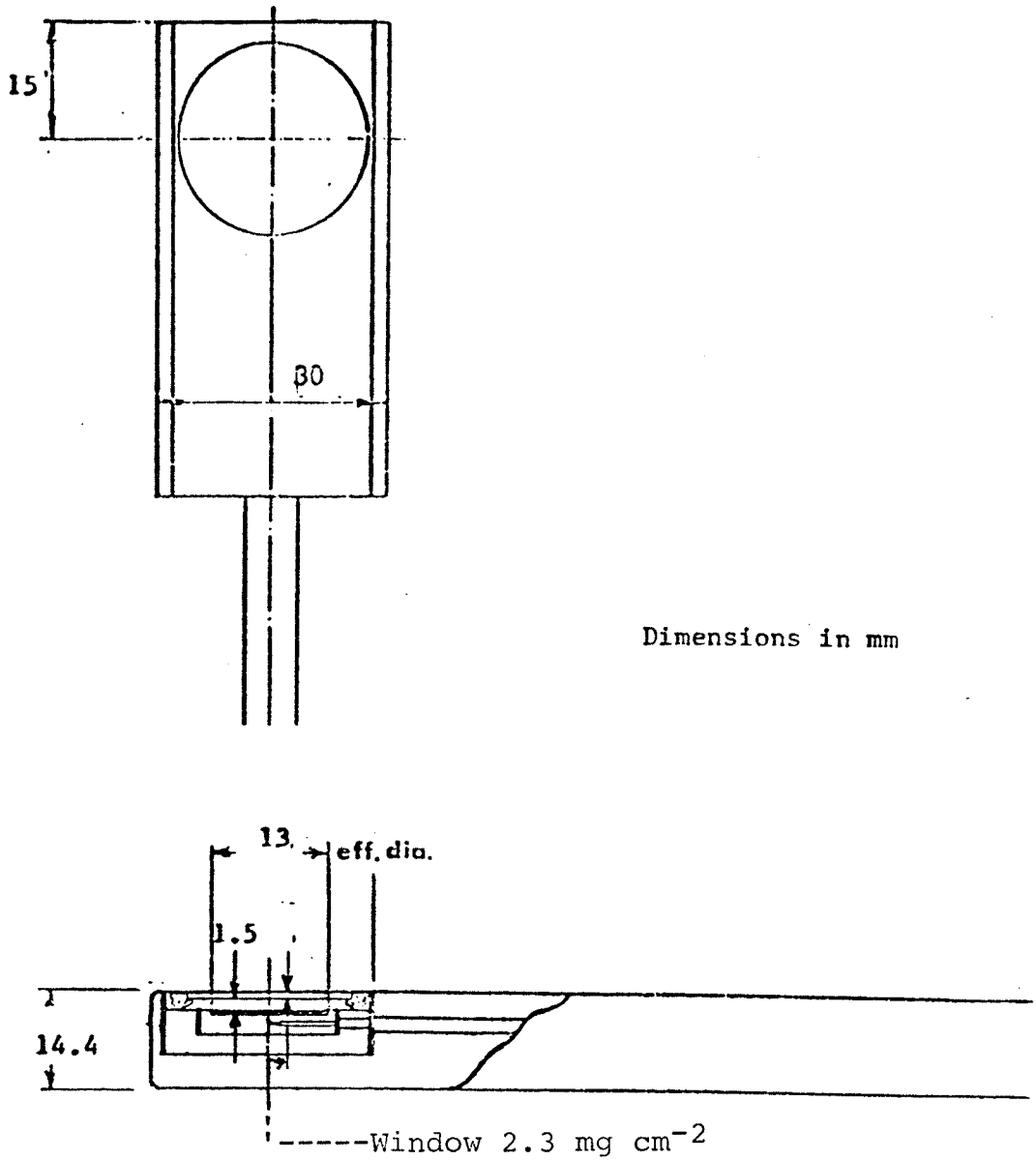

Figure 4.1 Ionization chamber used in dose measurements.
(Nuclear Enterprises Model 2536)

has 99.5% collection efficiency (manufacturer's specification) for an air dose of 0.10 cGy per radiation pulse.

4.3 THERMOLUMINESCENT DOSIMETRY

4.3.1 Theory

Thermoluminescence (TL) is a property of certain materials such as ceramics, glasses and crystalline substances (e.g. LiF). The mechanism of TL may be summarized as follows. Impurity atoms or other crystal lattice defects provide metastable electron states several eV above the valance band. Some of the electrons freed from the valance band by ionizing radiation may become trapped in these states (Figure 4.2). When the crystal is heated to a sufficient temperature, thermal excitation energy releases electrons from the traps and they return to the valance band, radiating light in the visible and near visible spectrum. The traps generally fall into several groups, each group releasing its electrons at a different temperature. The temperature of release is characteristic of the type of crystal and impurities (ZI). The total light emitted is a function of the absorbed dose. The crystal may be returned to its original state and re-used by a high temperature annealing and cooling procedure. The lower energy metastable electron states tend to be less stable and spontaneous transitions may occur at room temperature before readout. This process is known as fading.

4.3.2 TLD Reader

Figure 4.3 shows in block diagram the major components of a TL reader system. A TLD sample is heated in a planchet at a

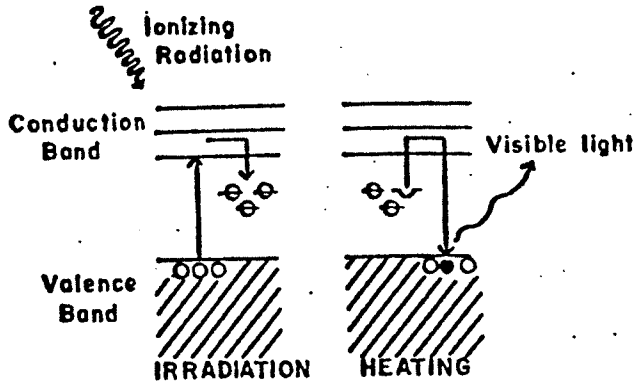

Figure 4.2 Schematic diagram illustrating Thermoluminescence mechanism.

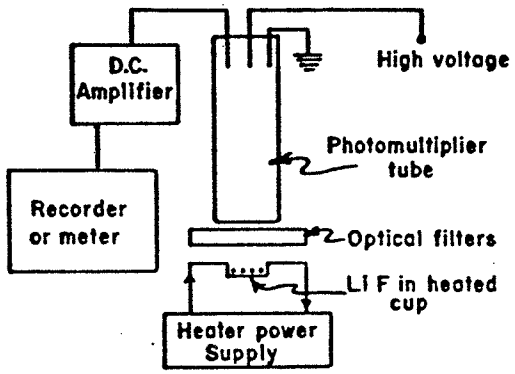

Figure 4.3 Schematic representation of TLD reader.

constant temperature rate. Light emitted from the sample is incident upon the photocathode of a photomultiplier tube. The signal from the photomultiplier tube may be amplified and recorded as a function of heating time or temperature of the TLD sample. The resulting 'glow curve' encloses an area which is proportioned to the radiation dose (Figure 4.4).

For routine dosimetry, the photomultiplier signal is directed to a charge integrator and the total charge is displayed on a digital readout. A built in carbon activated sodium iodide light source is used to monitor photo multiplier stability.

Optical filters between the sample heater and photomultiplier reduce the background contributed by infrared radiation from the sample heater.

A constant flow of N_2 gas across the sample heater significantly reduces chemiluminescence induced by oxygen and water vapour (HOR) and oxidation of the planchet.

4.3.3 TL Dosimeters

Dosimeters consisting of thermoluminescent material, specially formulated to intensify the TL response, are commonly available in a wide variety of shapes for differing applications. LiF is widely used in radiotherapy departments since its effective atomic number (8.31) and its energy response are close to that of tissue. Figure 4.5 shows the measured energy response of LiF TLD (CA.).

The TLD sensitivity (nC/cGY) is affected by various parameters

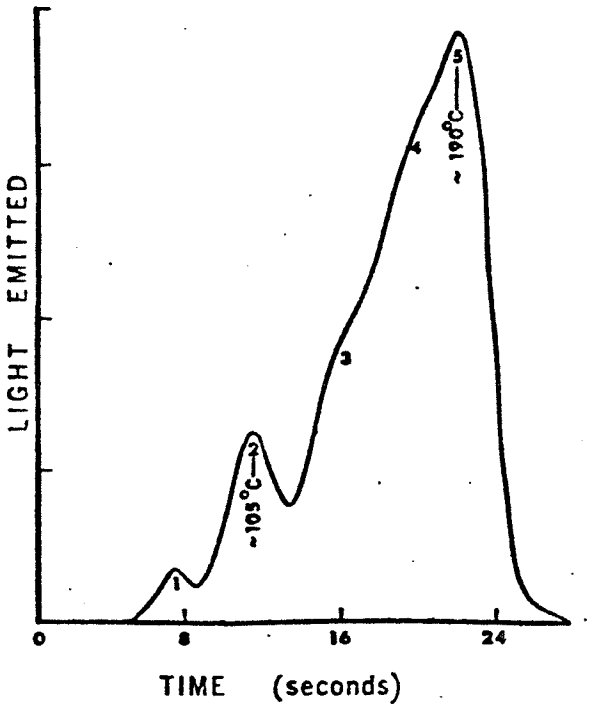

Figure 4.4 Glow curve for Lif-100 showing relative light output as a function of heating time. Reproduced from Cameron et al. (CA.)

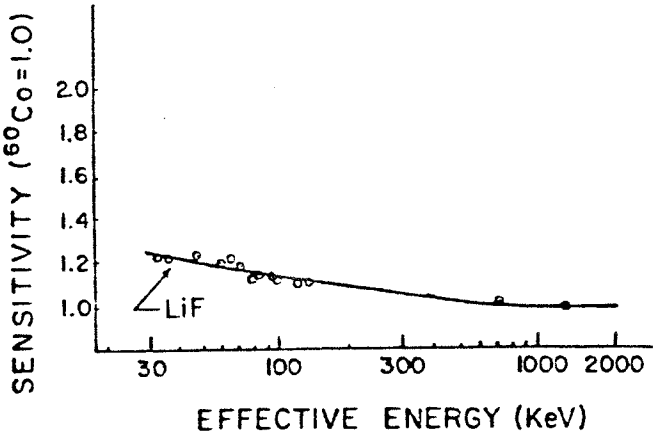

Figure 4.5 Experimental energy response for Lif-100 TLD. Reproduced from Cameron et al.(CA.)

such as pre and post radiation annealing, time and temperature and cooling rate. It is therefore necessary to follow a reproducible heating and cooling procedure for all dosimeters.

4.3.4 Materials and Methods

Three types of TL dosimeters are employed in this work. Their characteristics are summarized in Table 4.1. The requirement of good spatial resolution when measuring in regions of steep dose gradient, necessitate the use of a small detector. The small physical dimensions (Table 4.1) of LiF-100 extruded rods satisfy the criteria of small detectors and consequently were used for dose measurements in the penumbral region.

LiF-100 chips were used for eye dose measurements performed on patients and on an anthropomorphic phantom (Alderson Rando).

LiF-Teflon discs were used to measure surface dose outside beam edge because of their small thickness (0.13 mm). The annealing procedures (and equipment employed) in this work are summarized in Appendix A.

When Teflon discs were readout, a specially designed metal ring holder was attached to the heating planchet to keep the discs in good contact with the planchet. Consequently, uniform heating across the disc surface area was obtained. This was verified by measuring the sensitivity variation across a sample of Teflon discs, irradiated to a known dose from Co-60 source and readout with and without the ring holder being attached to the heating planchet.

Characteristics of LiF TLD's

Type	Physical Form	Dimensions (cm)	LiF Content Weight (%)	Effective Atomic Number
LiF-100 (Harshaw)	Extruded Rods	.1 x .1 x .6	100	8.14
LiF-100 (Harshaw)	Chips	.3 x .3 x .09	100	8.14
D-LiF-0.13 (Teledyne Isotope)	Teflon Discs	1.27 dia. x .013 thick	30%	8.25

TABLE 4.1

4.3.5 Calibration of TLD

The TL dosimeters were irradiated to a known dose from a Co-60 source. The source dose rate was verified by a calibrated thimble ionization chamber. After read out the TLD's were divided into groups such that the standard deviation (SD) of the sensitivity in each group did not exceed 2% of the group mean. Calibration factors between group means were obtained. One or two of these groups were used for each set of dose measurements. After two annealing-irradiation readout cycles all TLD's were re-calibrated against the Co-60 source.

Variations in SD of the group was observed but the change did not exceed 5% of the group mean. The TLD's were then re-grouped with 2% SD for each group and new calibration factors between group means were obtained.

By using the above calibration procedure 2-5% reproducibility in results was obtained for the data measured using LiF TLD's.

4.3.6 LiF TLD Response vs Dose

In this work the response of LiF TLD-100 extruded rods was measured as a function of dose from a Co-60 source. A linear response was observed in the dose range of 2-200 cGy (Figure 4.6). Similar results have been obtained by other workers (CA.)

DOSE RESPONSE FOR LiF-100

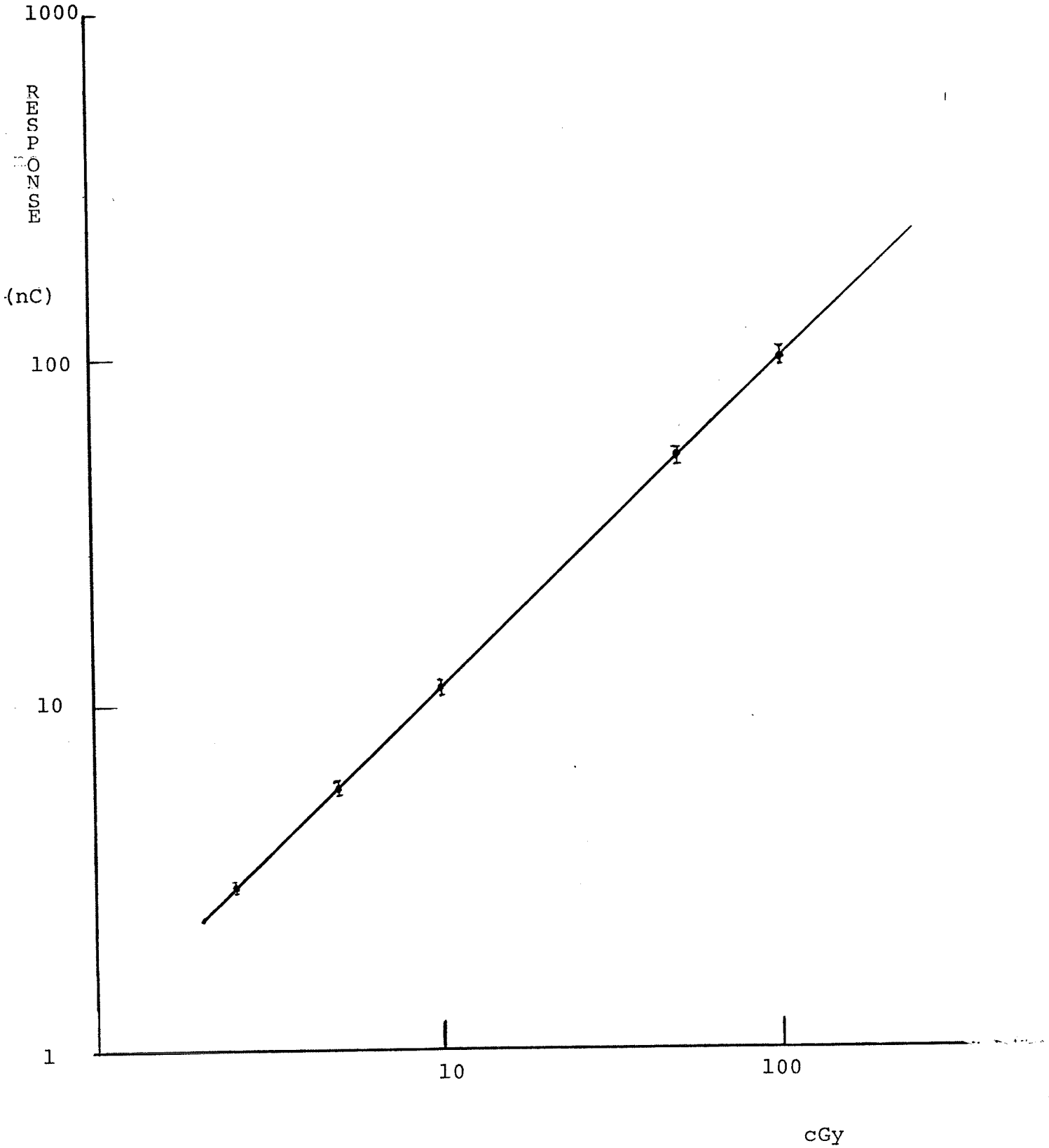

Figure 4.6

Chapter 5. Evaluation of the Effectiveness of Lead Acrylic as an Electron Filter

5.1 THE BUILD-UP REGION OF A HIGH ENERGY PHOTON BEAM

One of the important advantages of high energy photon beams for radiotherapy is the "skin sparing" that results from the initial increase of absorbed dose with depth immediately beyond the entrance surface of the body. This allows the delivery of a larger tumour dose at a depth for a given surface dose, D_s to the skin. The dose increases to a broad maximum D_{max} at a depth d_{max} (Figure 5.1). The dose at a point at a given depth is proportional to the electron fluence at the point. Near the surface, the electron fluence increases with depth as additional forward-directed secondary electrons are set in motion by photon interactions in succeeding layers of material in the body or phantom. At the position of D_{max} the number of electrons set in motion by photons is balanced by the number of electrons reaching the end of their tracks. At depths greater than d_{max} the absorbed dose decreases, reflecting the attenuation of the photon beam.

For a clean photon beam (i.e. uncontaminated by incident electrons), D_{max} is observed to occur at a depth somewhat less than the maximum penetration of the most energetic electrons originating in the phantom surface layer.

Higher energy photons tend to give a dose maximum deeper in the phantom, while producing a lower value of D_s.

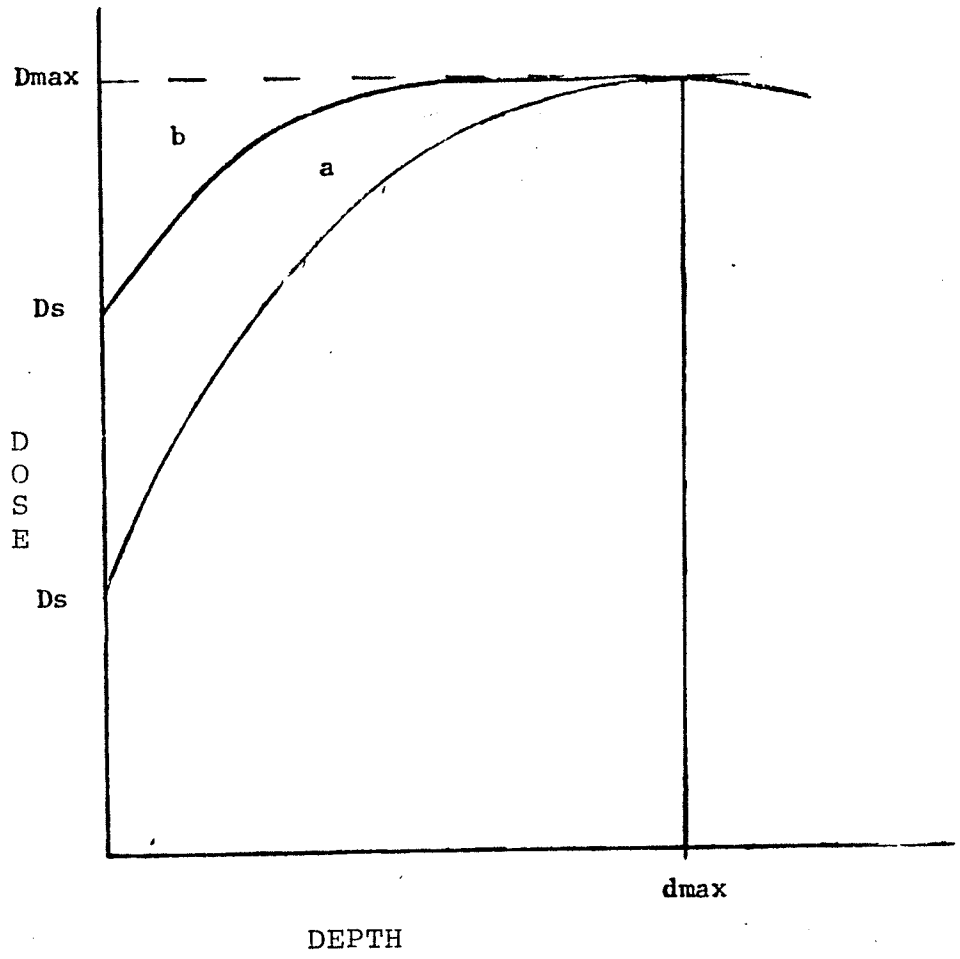

Figure 5.1 Curve 'a' shows a typical build-up of dose for a high energy photon beam. Curve'b' shows the effect of electron contamination where an increase in the surface dose Ds occurs and the position of Dmax is shifted towards the surface.

5.1.1 The Effect and Sources of Electron Contamination

The presence of significant electron contamination in the incident beam tends to increase the dose at the surface and in the build-up region, thus reducing or even losing the skin sparing of high energy photon beams (see Figure 5.1). In addition, D_{max} has been reported (LE., PA.,) to shift closer to the surface as a result of electron contamination. This shift is more apparent for large field sizes.

There has been a wide disagreement concerning the origin of the contamination electrons. Photon interaction with the collimator jaws (PA.,GR.,VE.), field flattering filter (Figure 5.2), (GR.,JA) and intervening air (AT.,HO.,NI) between the source and the entrance phantom surface has been cited as possible sources. It is generally agreed that the presence of scattering material in the field of the phantom beam will increase the magnitude of electron contamination.

In radiotherapy practice, it is often necessary to introduce additional scattering material into the beam such as beam modifying devices and their supporting fixtures (Figure 5.2).

The beam modifying devices are usually supported by an accessory platform commonly known as a shadow tray, which is made of low atomic number plastic material. This shadow tray in turn acts as an electron source (see Figure 5.2). For large SSD treatments the bridge (also made of low Z plastic material) is ued to support lead shielding and acts as an additional source of electron contamination.

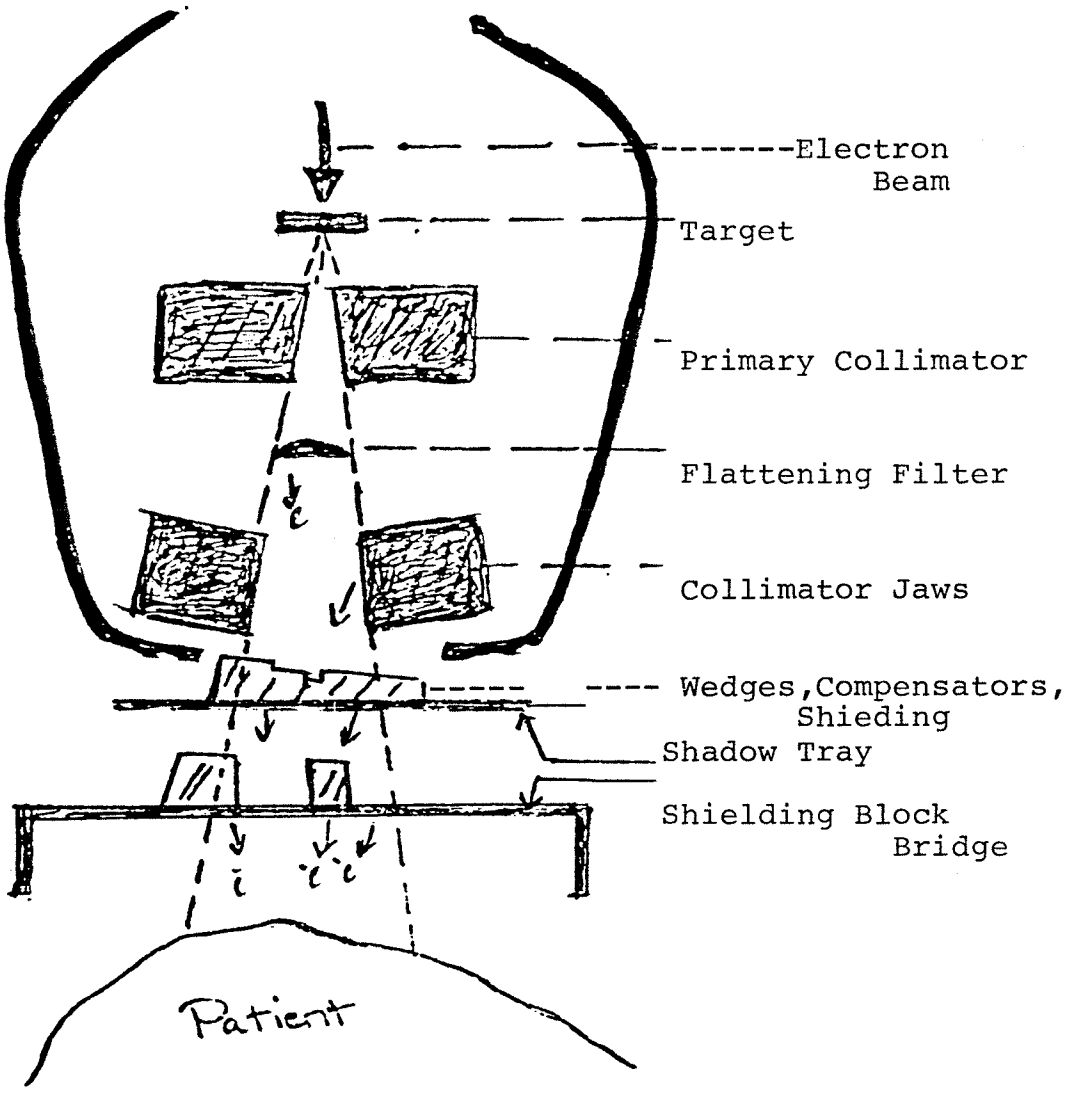

Figure 5.2 Possible electron sources.

5.1.2 Methods of Reduction of Electron Contamination

(i) Adequate distance (JO2.,IB.) between the scattering material and the entrance surface has been suggested for minimizing electron contamination. This technique is feasible for small field sizes but much larger distances from the entrance surface are needed for larger fields. This is impractical due to the constraint imposed by the treatment head (see Figure 5.2). Moreover, the penumbra width of shielding blocks supported by a shadow tray far from the skin surface will be large.

(ii) Magnetic fields with sufficient strength can be applied to remove electrons from the photon beam as demonstrated by several workers (PA.,BI.,LI). These investigators proved conclusively that electrons were the principle beam contaminant, rather than low eneregy scattered photons as had been alternatively suggested (MA.). However, the routine removal of electron contamination by magnetic means is an impractical procedure due to space, weight and cost consideration.

(iii) An alternative to methods 1 and 2, which was investigated in this work, is the use of solid electron filters, placed between the source of electrons and the entrance surface. Various electron filters have been described. They all suffer from various drawbacks that are discussed in the next section.

5.1.3 Optimum Filter Material

In 1951 Hine (HI.) had shown that the emission in the forward direction of secondary electrons for high energy x-rays decreases with atomic number of the material, reaches a minimum for

medium Z materials, then increases for high Z materials due to the additional emission of photoelectrons. Consequently, for an electron filter, medium atomic number materials have been suggested to minimize the surface dose.

Medium Z metallic material (LE.,RA.) and leaded glass (LE.,AM.) have been reported to be efficient electron filters. Metallic filters are opaque and therefore have the disadvantage of interfering with the light localization of the treatment field. Transparent lead glass is fragile, not readily obtainable in custom shapes and sizes and not machinable. Both are considered as a major inconvenience. Because of above disadvantages, metallic filters or lead glass filters are not widely used resulting in unnecessarily high skin doses.

This study evaluates the filtering effectiveness of lead acrylic, a relatively new material that overcomes the major disadvantages hindering routine use of the above discussed electron filters. Moreover, this filter can serve the dual purpose of acting as the supporting structure for lead shielding blocks, compensators or other beam modifying devices as well as the electron filter.

5.2 MATERIALS AND METHODS

The radiation dose in the buildup region of a 4 MV x-ray was measured for various field sizes and filter skin distances. Comparisons were made with the open beam values (i.e. no additional scatter in the beam), with an acrylic filter, a lead acrylic filter and a lead glass filter. The acrylic filter represents the usual case where acrylic shadow tray supports the shielding blocks, compensators or other beam modifying devices.

Build-up region and surface dose measurements were made with the thin window parallel plate ionization chamber. The chamber was embedded in tissue equivalent rubber phantom , Temex, whose physical characteristics are summarized in Table 5.1 (WH.).

The phantom dimensions were 20x40 x 40 cm. This provides effectively full scattering conditions on the central axis of even the largest field. The chamber thin window was perpendicular to and facing the direction of the central ray of the beam and in the same plane as the front surface of the phantom. Acrylic sheets of different thicknesses were placed on top of the chamber to provide surface build-up (Figure 5.3).

A surface ionization measurement was taken with no absorber on the top of the chamber. By placing acrylic sheets upon the chamber, a series of ionization measurements was made until maximum ionization was found. The relative dose (RD) was defined as the ratio of ionization for a given thickness of build-up material to the maximum ionization and quoted as a percentage. In the measurement of surface dose, the depth of measurement is determined by the thickness of the ioniza-

Characteristics of Temex Rubber

Density g cm^{-3}	$(\mu_{en}/\rho)^a$ Temex / (μ_{en}/ρ) Tissue		$(S/\rho)^b$ Temex / (S/ρ) Tissue	
	Energy (MeV)		Energy (Mev)	
	0.1	1	0.1	1
1.01	1.01	0.99	1.00	0.99

a) μ_{en}/ρ mass absorption coefficient
b) S/ρ mass stopping power

Data from White (WH)

TABLE 5.1

Physical Characteristics of Various Trays

	Density (g cm^{-3})	Thickness (cm)
Acrylic	1.19	.7
Lead Acrylic (30% Pb)	1.6	2.2
Lead Glass	5.0	.63

TABLE 5.2

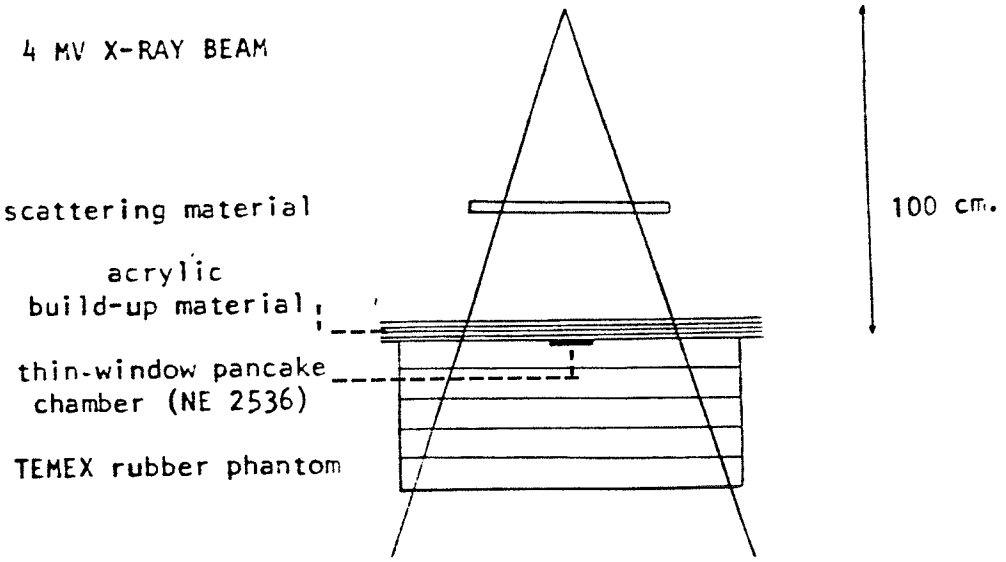

EXPERIMENTAL SET-UP

Figure 5.3

tion chamber window employed (0.0023 gcm^{-2}). The clinically significant depth for skin dose measurement is 0.0055 ± 0.0024 gcm^{-2} (WHI.).

Relative surface dose (RSD) is defined as the ratio of ionization with no build-up material (i.e. 0.0023 gcm^{-2} depth) to the maximum ionization.

Data was accumulated for the open beam (i.e. no tray in the beam) and for the case when acrylic, lead acrylic and lead glass trays were introduced into the beam. The physical characteristics of the above trays are shown in Table 5.2.

In order to investigate the effects of field size and tray to surface distance (TSD), RD measurements were made for the following conditions:

Field sizes 10 x 10, 20 x 20, 30 x 37.5 cm

Tray to surface distances - 10, 20, 30 and 40 cm

5.3 RESULTS

5.3.1 Build-up Curves

Figures 5.4, 5.5 and 5.6 show the build-up curves for field sizes 10 x 10, 20 x 20 and 30 x37.5 cm respectively at 100 cm source to chamber distance. The RD is plotted as a function of gcm^{-2} of build-up material.

5.3.2 Characteristics of the Open Beam Build-up Curves

The RSD for the open beam increases with field size, from 22% to 39% for the 10 x 10 and 30 x 37.5 cm field sizes respectively, illustrating the increase in electron contamination with increasing field size. As build-up thickness increases the RD

increases reaching 100% at approximately 1.0 gcm^{-2} depth. A broad maximum of about 3 mm width is observed.

5.3.3 Characteristics of Beam Build-up Curves with Trays in the Field

The RSD increases with field size, to over 34% and 70% for field sizes 10 x 10 and 30 x 37.5 cm respectively when acrylic, lead glass and lead acrylic trays are introduced into the beam at a distance of 10 cm away from phantom surface (Figures 5.4 and 5.6). A shift in the position of maximum dose to shallower depths and a loss of skin sparing is evident when the trays are placed in the beam. These effects are most apparent for large field size and for acrylic scattering material. Due to the difficulty of specifying the depth at which maximum dose is attained, the depth of the 90% dose was selected as a parameter to investigate the shift in d_{max}.

5.3.4 The Effect of Tray to Surface Distance

(i) On build-up curves. Figures 5.7 to 5.12 illustrate the change in build-up curve shape for various tray to surface distances (TSD). The build-up curves are seen to return to the open beam build-up curve when the trays are at large distances away from the phantom surface. The acrylic tray is seen to reproduce the open beam build-up curve when it is at 40 cm away from the surface for small field sizes 10 x 10 cm (Figure 5.7). However, for large field sizes (30 x 37.5) a greater distance is required (Figure 5.10). For a 10 x 10 cm field size, lead acrylic and lead glass show build-up curves superior to open beam conditions when the trays are at a

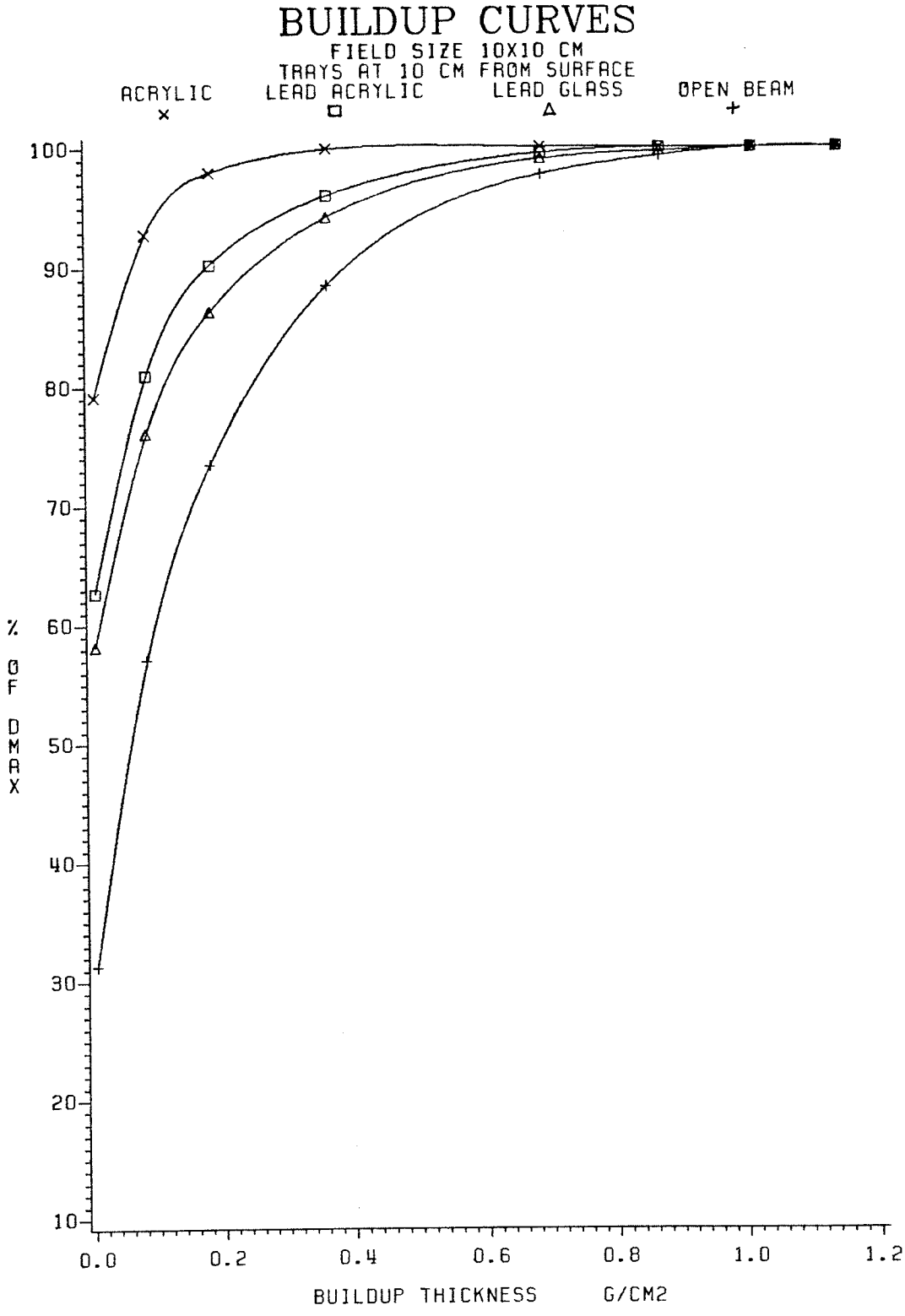
BUILDUP CURVES
FIELD SIZE 10X10 CM
TRAYS AT 10 CM FROM SURFACE
ACRYLIC
LEAD ACRYLIC
LEAD GLASS
OPEN BEAM
100
90
80
70
60
50
40
30
20
10
% OF DMAX
0.0
0.2
0.4
0.6
0.8
1.0
1.2
BUILDUP THICKNESS G/CM2

Figure 5.4

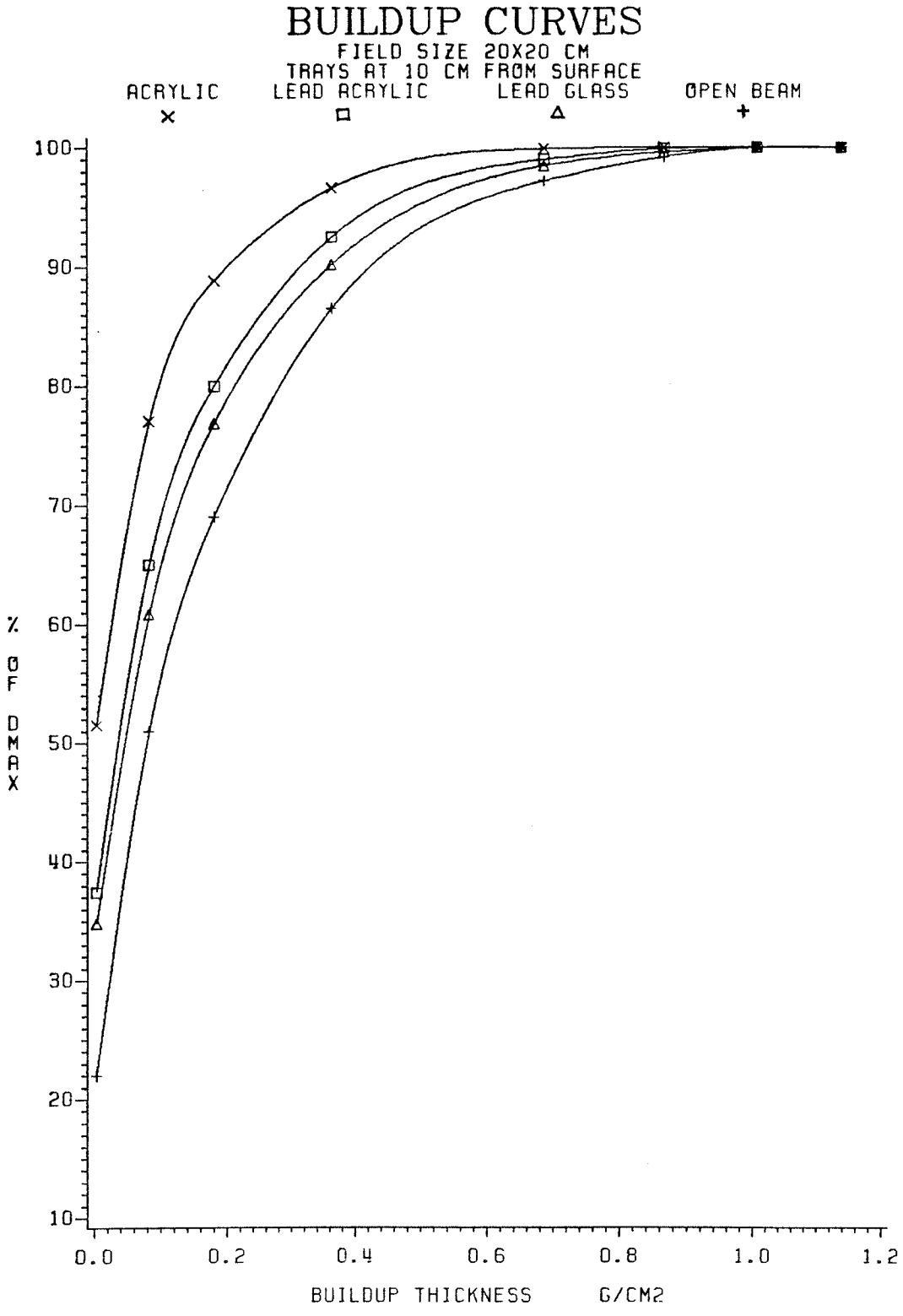
BUILDUP CURVES
FIELD SIZE 20X20 CM
TRAYS AT 10 CM FROM SURFACE
ACRYLIC
LEAD ACRYLIC
LEAD GLASS
OPEN BEAM
100
90
80
70
60
50
40
30
20
10
% OF DMAX
0.0
0.2
0.4
0.6
0.8
1.0
1.2
BUILDUP THICKNESS G/CM2

Figure 5.5

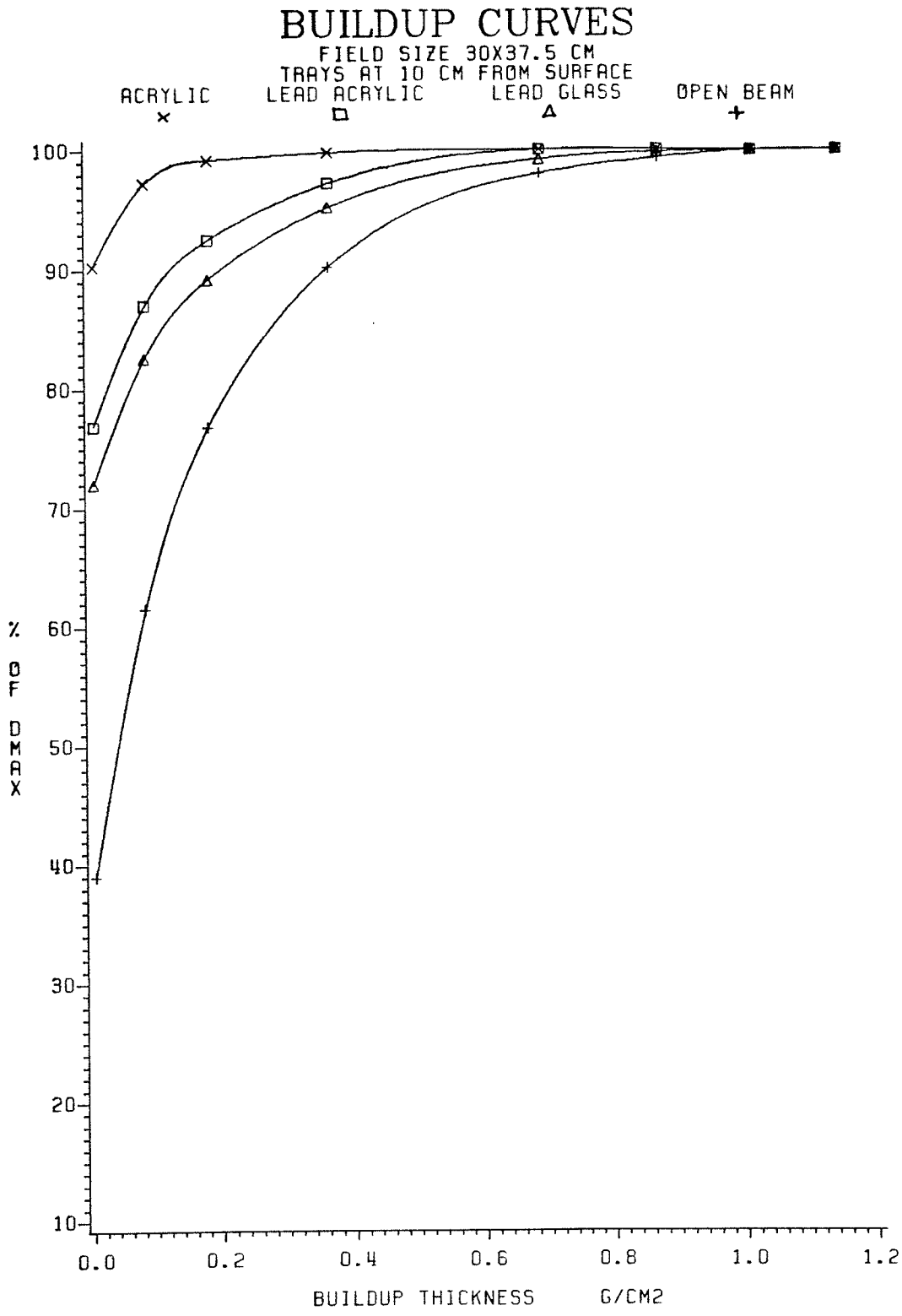
BUILDUP CURVES
FIELD SIZE 30X37.5 CM
TRAYS AT 10 CM FROM SURFACE
ACRYLIC
LEAD ACRYLIC
LEAD GLASS
OPEN BEAM
100
90
80
70
60
50
40
30
20
10
% OF DMAX
0.0
0.2
0.4
0.6
0.8
1.0
1.2
BUILDUP THICKNESS G/CM2

Figure 5.6

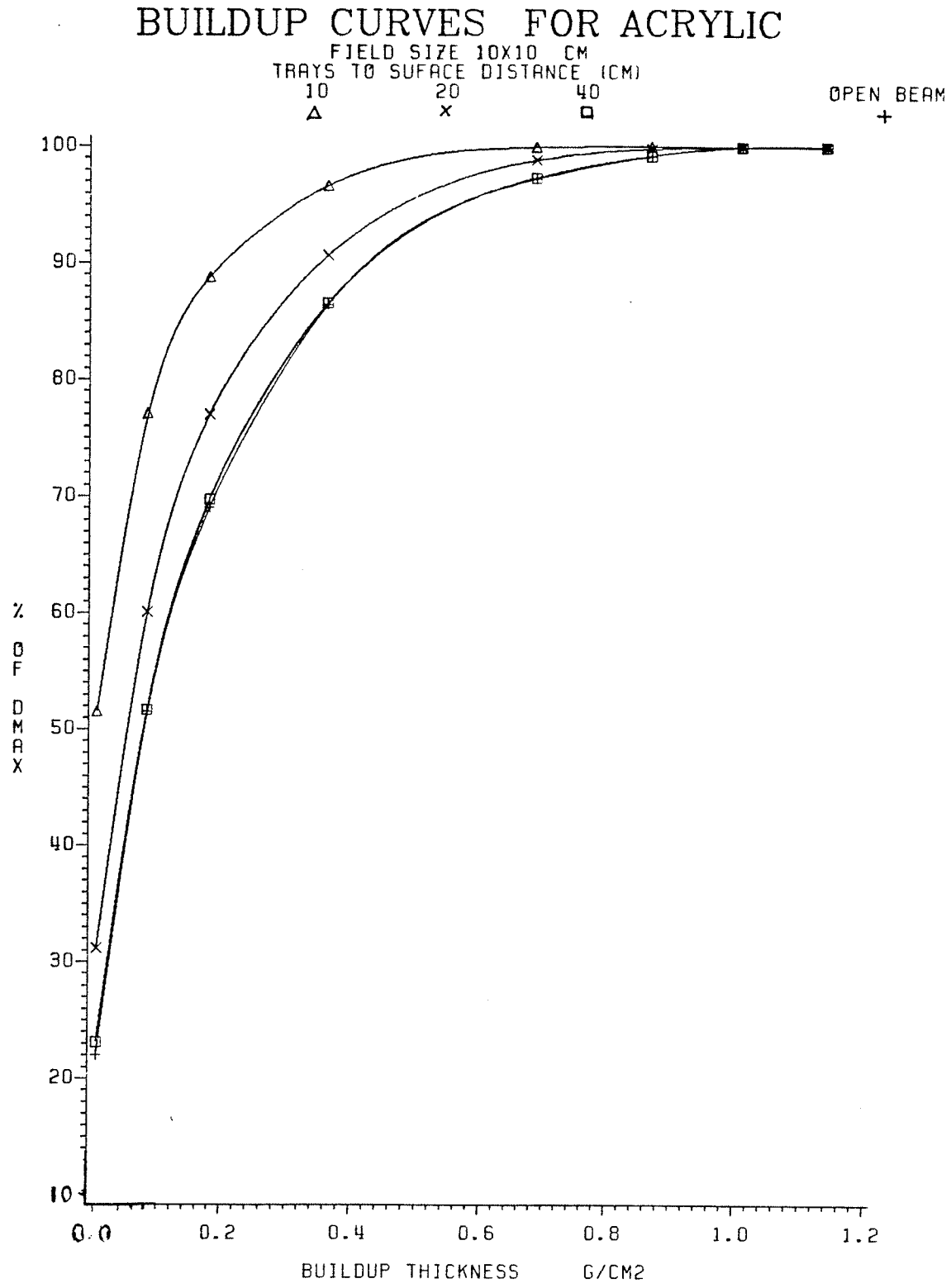
BUILDUP CURVES FOR ACRYLIC
FIELD SIZE 10X10 CM
TRAYS TO SUFACE DISTANCE (CM)
10
20
40
OPEN BEAM
100
90
80
70
60
50
40
30
20
10
% OF DMAX
0.0
0.2
0.4
0.6
0.8
1.0
1.2
BUILDUP THICKNESS G/CM2

Figure 5.7

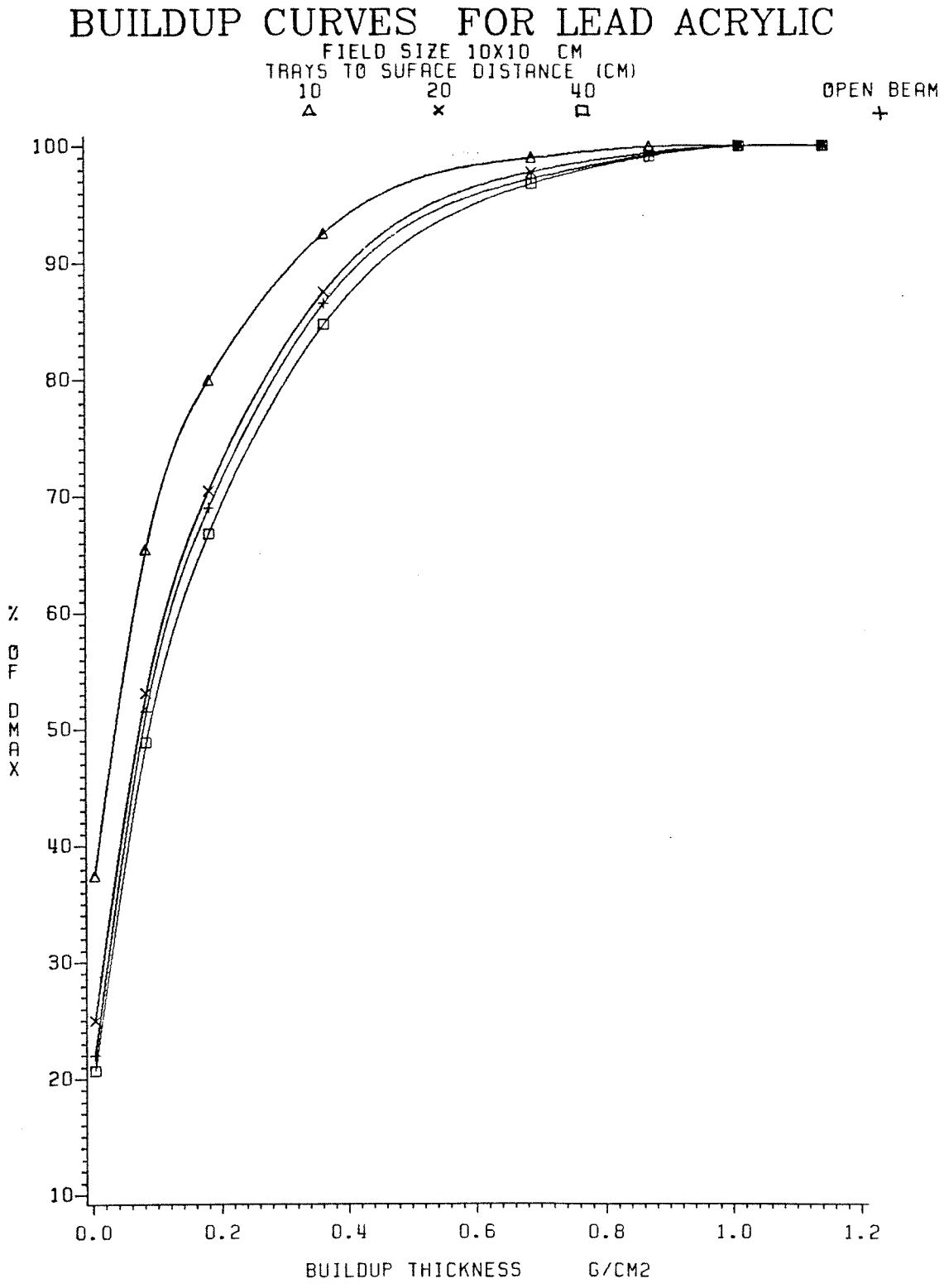
BUILDUP CURVES FOR LEAD ACRYLIC
FIELD SIZE 10X10 CM
TRAYS TO SUFACE DISTANCE (CM)
10
20
40
OPEN BEAM
100
90
80
70
60
50
40
30
20
10
% OF DMAX
0.0
0.2
0.4
0.6
0.8
1.0
1.2
BUILDUP THICKNESS G/CM2

Figure 5.8

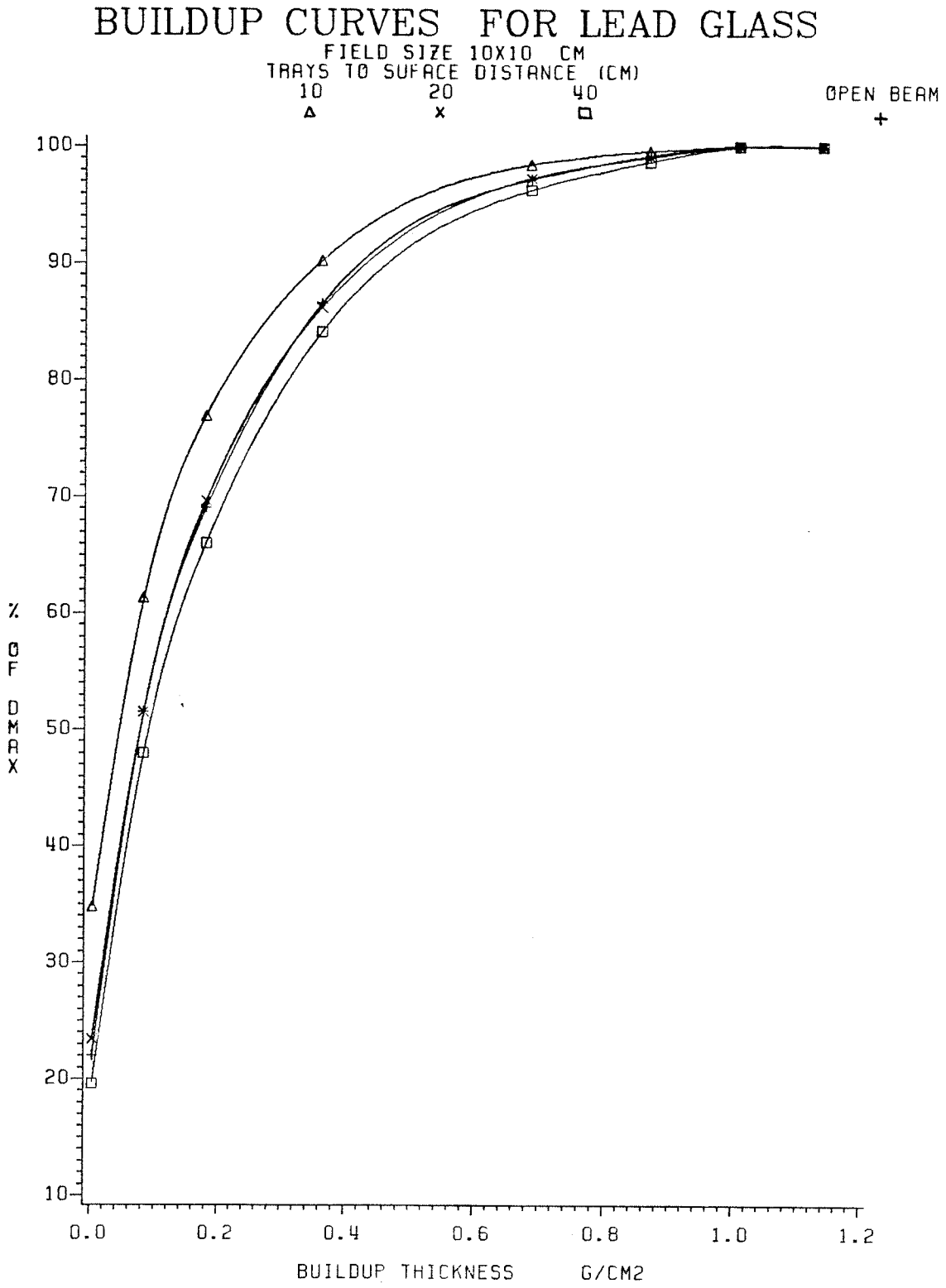
BUILDUP CURVES FOR LEAD GLASS
FIELD SIZE 10X10 CM
TRAYS TO SURFACE DISTANCE (CM)
10
20
40
OPEN BEAM
100
90
80
70
60
50
40
30
20
10
% OF DMAX
0.0
0.2
0.4
0.6
0.8
1.0
1.2
BUILDUP THICKNESS G/CM2

Figure 5.9

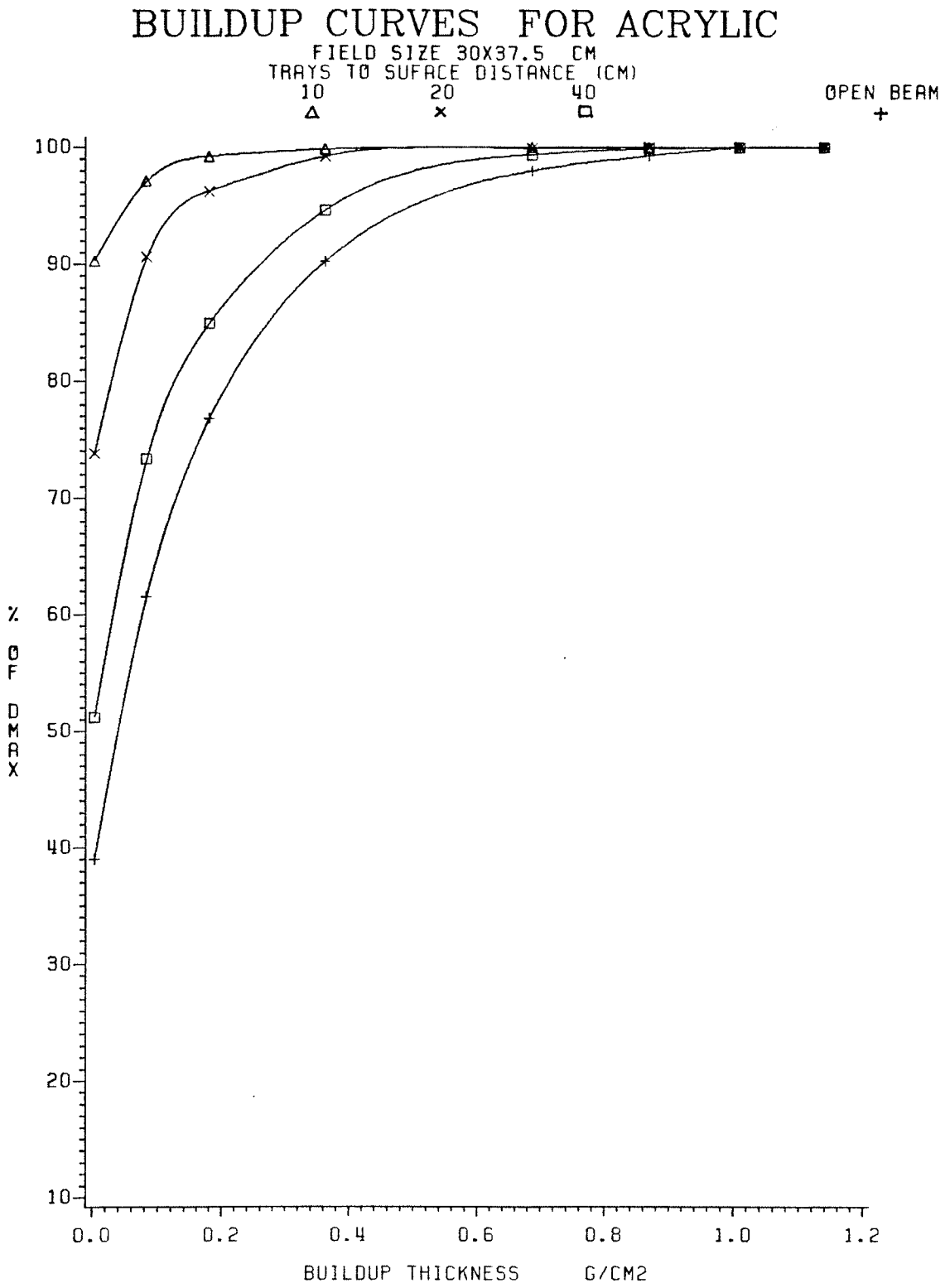
BUILDUP CURVES FOR ACRYLIC
FIELD SIZE 30X37.5 CM
TRAYS TO SUFACE DISTANCE (CM)
10
20
40
OPEN BEAM
100
90
80
70
60
50
40
30
20
10
% OF DMAX
0.0
0.2
0.4
0.6
0.8
1.0
1.2
BUILDUP THICKNESS G/CM2

Figure 5.10

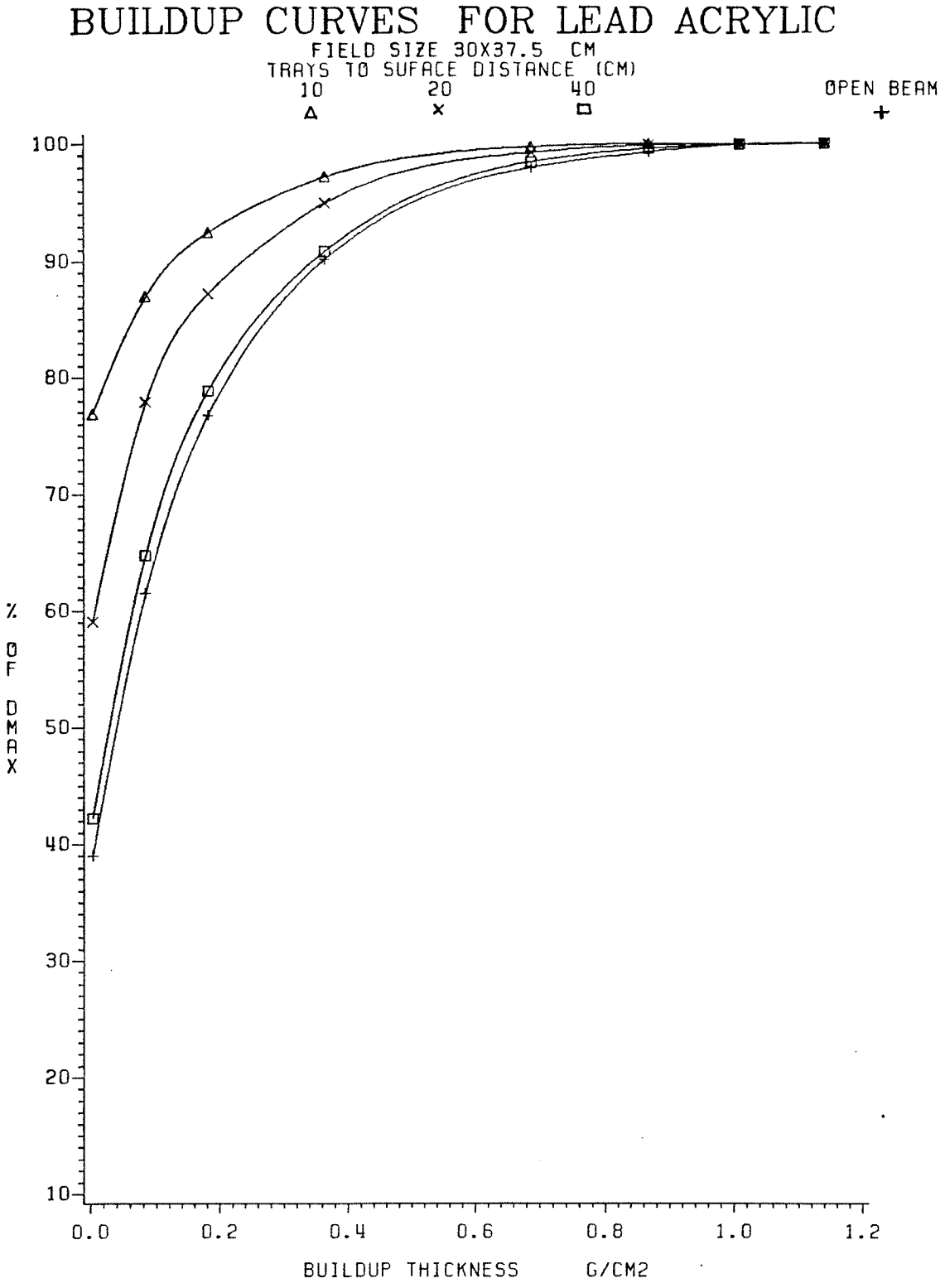
BUILDUP CURVES FOR LEAD ACRYLIC
FIELD SIZE 30X37.5 CM
TRAYS TO SUFACE DISTANCE (CM)
10
20
40
OPEN BEAM
100
90
80
70
60
50
40
30
20
10
% OF DMAX
0.0
0.2
0.4
0.6
0.8
1.0
1.2
BUILDUP THICKNESS G/CM2

Figure 5.11

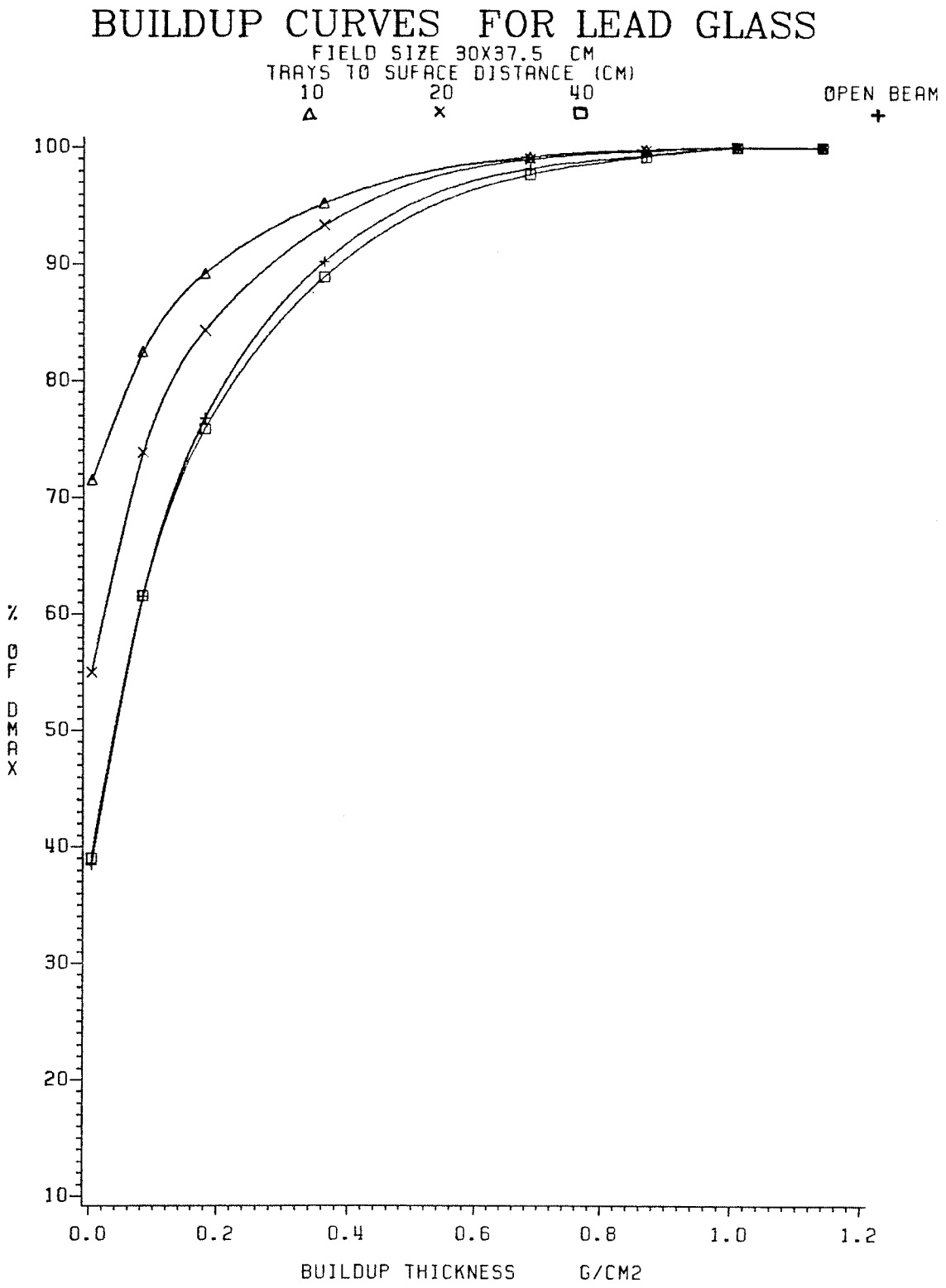
BUILDUP CURVES FOR LEAD GLASS
FIELD SIZE 30X37.5 CM
TRAYS TO SUFACE DISTANCE (CM)
10
20
40
OPEN BEAM
100
90
80
70
60
50
40
30
20
10
% OF DMAX
0.0
0.2
0.4
0.6
0.8
1.0
1.2
BUILDUP THICKNESS G/CM2

Figure 5.12

distance > 30 cm from the surface (Figures 5.8 and 5.9).

(ii) On Surface Dose. The variation of RSD as a function of TSD for large and small fields 10 x 10 and 30 x 37.5 cm is shown in Figure 5.13). The surface dose decreases as TSD increases. Lead glass and lead acrylic trays effectively reduce the surface dose to lower levels than open beam conditions. This situation occurs for a 10 x 10 cm field when lead glass and lead acrylic trays are at TSD's greater than 23 and 30 cm respectively. For a 30 x 37.5 cm field size, the RSD is equal to the open beam value when lead glass is at 40 cm from the surface. Table 5.3 shows the TSD required to limit the surface dose elevation to 10% of the open beam values.

(iii) On Depth of 90% dose. Figure 5.14 shows the change in the depth of the 90% dose as a function of TSD for a 20 x 20 cm field size. The acrylic tray shifted the 90% position from 0.4 gcm^{-2} (open beam) to 0.05 gcm^{-2} at 10 cm TSD. AS TSD increases, the depth of the 90% increases. The 90% depth retains its open beam position at 30 and 35 cm TSD for lead glass and lead acrylic respectively. A further TSD increase shifts the 90% dose to a greater depth than the open beam position. Table 5.4 shows the TSD required to retain the open beam 90% dose position.

5.3.5 Effect of Field Size

(i) On surface dose. The RSD as a function of size of equivalent square field is plotted in Figure 5.15 for open field and when the trays are at 20 cm away from the phantom surface. The

curves show that the surface dose increases with field size. The rate of increase is greatest for acrylic and smallest for the open beam case. Lead acrylic and lead glass are in intermediate positions.

(ii) On Depth of 90% Dose. Figure 5.16 illustrates the change in position of 90% dose with size of equivalent square field when the trays are at 10 cm TSD. For open beam conditions the depth of 90% shifts from 0.43 gcm^{-2} at 10 x 10 cm field size to 0.36 gcm^{-2} at 30 x 37.5 cm field size. Introduction of the trays into the beam shifts the 90% towards shallower depth, with the shift being greatest for large field size and the acrylic tray. Tables 5.3 and 5.4 illustrate the increases in TSD required to compensate for increasing field size in order to obtain good treatment field characteristics in the build-up region.

5.3.6 Effect of Tray thickness

Using a field size of 9.5 cm x 9.5 cm the surface dose was measured for tray thicknesses varying from 1.2 cm to 3.5 cm at 7 cm TSD. Surface dose was found to be independent of tray thickness.

5.3.7 Effect of Atomic Number

Figure 5.17 shows the RSD for materials of various Z. Measurements were made using LiF-teflon discs of 0.13 mm thickness). The surface dose initially decreases with Z reaching a minimum at Z equal 50. For higher Z material there is a slight increase due to increased photoelectric production. This agrees with the work of Hine (HI.) and Khan et al (KH.) on Co-60 and 10 MV photon beams. The

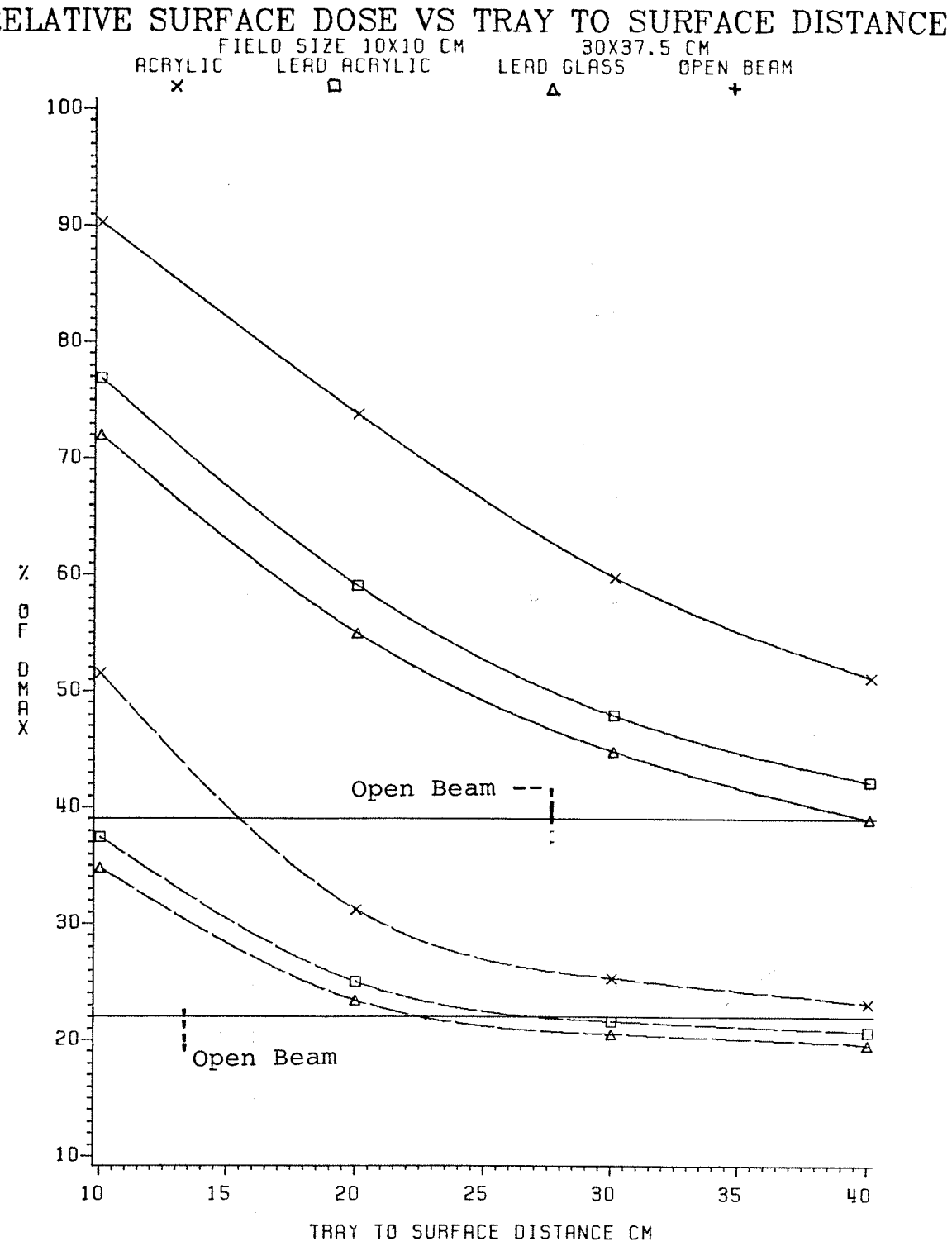
RELATIVE SURFACE DOSE VS TRAY TO SURFACE DISTANCE
FIELD SIZE 10X10 CM 30X37.5 CM
ACRYLIC
LEAD ACRYLIC
LEAD GLASS
OPEN BEAM
100
90
80
70
60
50
40
30
20
10
% OF DMAX
Open Beam
Open Beam
10
15
20
25
30
35
40
TRAY TO SURFACE DISTANCE CM

Figure 5.13

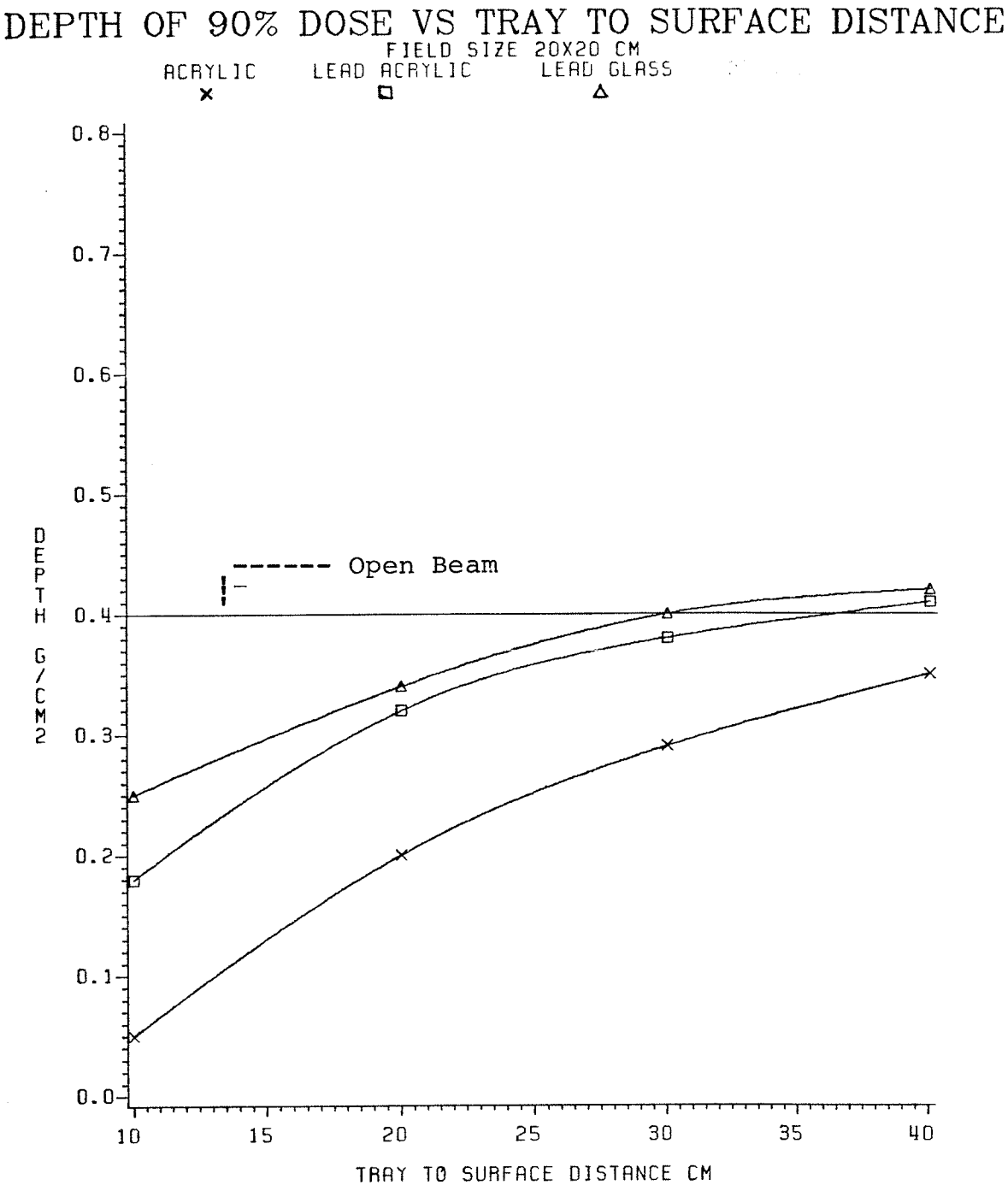
DEPTH OF 90% DOSE VS TRAY TO SURFACE DISTANCE
FIELD SIZE 20X20 CM
ACRYLIC
LEAD ACRYLIC
LEAD GLASS
0.8
0.7
0.6
0.5
0.4
0.3
0.2
0.1
0.0
DEPTH G/CM2
Open Beam
10
15
20
25
30
35
40
TRAY TO SURFACE DISTANCE CM

Figure 5.14

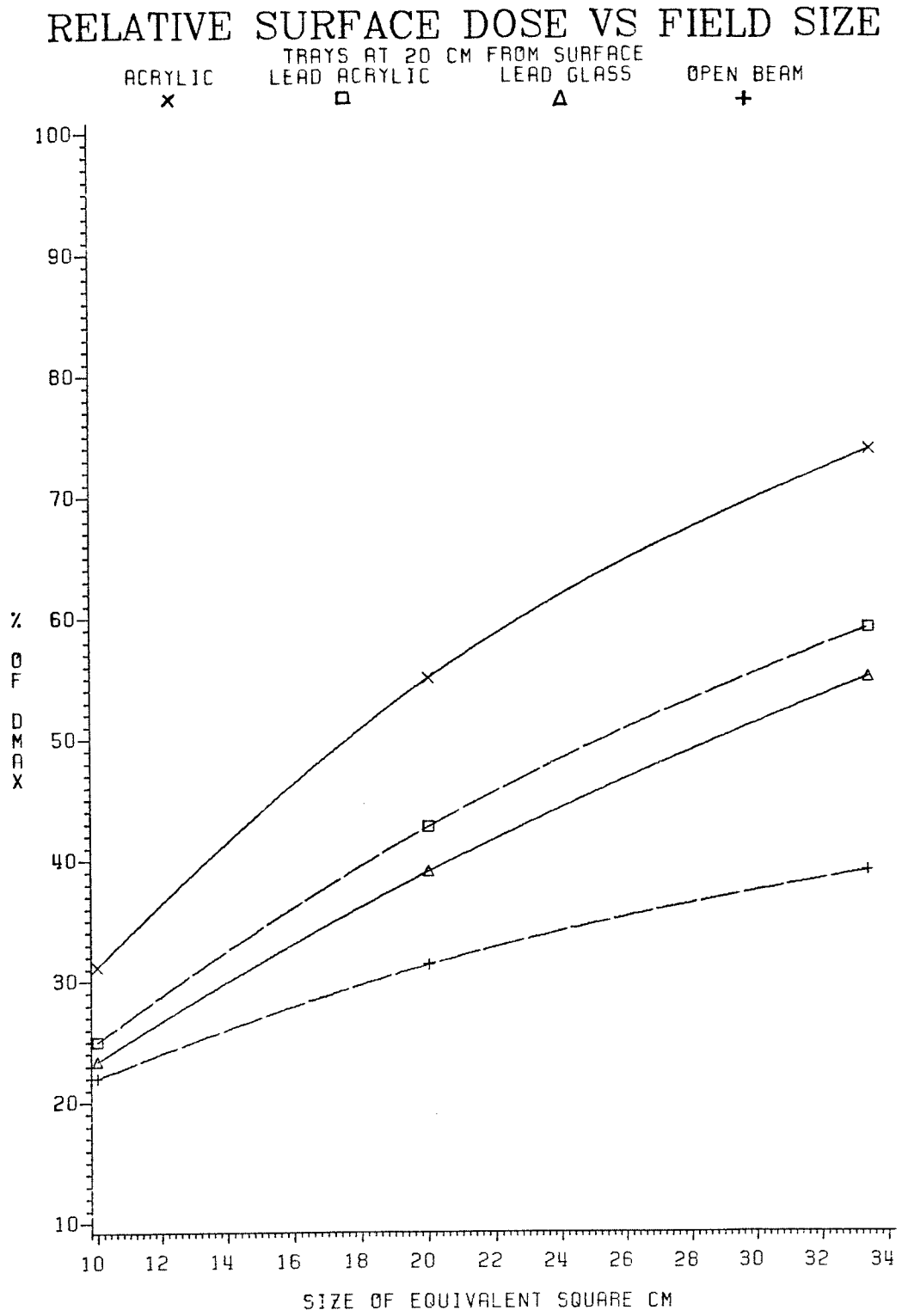
RELATIVE SURFACE DOSE VS FIELD SIZE
TRAYS AT 20 CM FROM SURFACE
ACRYLIC
LEAD ACRYLIC
LEAD GLASS
OPEN BEAM
% OF DMAX
100
90
80
70
60
50
40
30
20
10
10 12 14 16 18 20 22 24 26 28 30 32 34
SIZE OF EQUIVALENT SQUARE CM

Figure 5.15

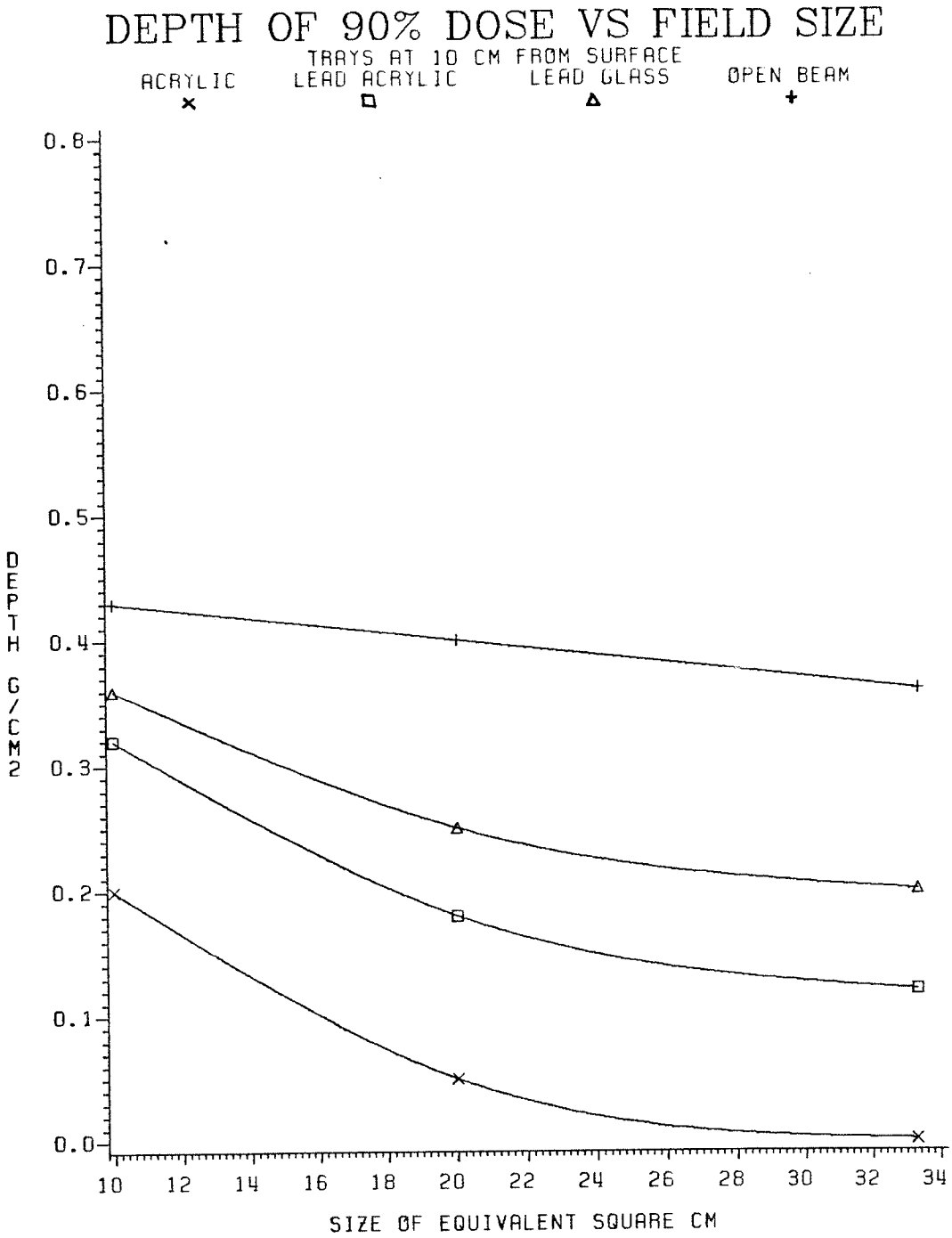
DEPTH OF 90% DOSE VS FIELD SIZE
TRAYS AT 10 CM FROM SURFACE
ACRYLIC
LEAD ACRYLIC
LEAD GLASS
OPEN BEAM
0.8
0.7
0.6
0.5
0.4
0.3
0.2
0.1
0.0
DEPTH G/CM2
10
12
14
16
18
20
22
24
26
28
30
32
34
SIZE OF EQUIVALENT SQUARE CM

Figure 5.16

FIELD SIZE (cm)	TRAY-SKIN DISTANCE NECESSARY TO LIMIT SURFACE DOSE ELEVATION TO 10% OF MAXIMUM DOSE (cm)		
	LEAD GLASS	LEAD ACRYLIC	ACRYLIC
10 x 10	12	13	19
20 x 20	19	21	31
30 x 37.5	25	29	44 (approx)

TABLE 5.3

FIELD SIZE (cm)	TRAY-SKIN DISTANCE (CM) REQUIRED FOR NO CHANGE IN THE DEPTH OF THE 90%		
	LEAD GLASS	LEAD ACRYLIC	ACRYLIC
10 x 10	20	23	40
20 x 20	30	35	45
30 x 37.5	40	45	50

TABLE 5.4

effective atomic number of lead acrylic and lead glass can be estimated from Figure 5.17 to be 28 and 69 respectively.

5.3.8 Empirical Expression for the Surface Dose

An empirical formula has been determined which describes the surface dose within the range of data measured for lead acrylic.

$$\text{Relative Surface Dose} = 22.4(S)^{0.666}(TSD)\exp^{(-0.454)} \%$$

when S = Side of Equivalent Square

TSD - Tray to Surface Distance

Table 5.5 shows the measured and calculated relative surface dose for various S and TSD. The % difference shown in Table 5.5 did not exceed $\pm$ 5%.

5.3.9 Further Investigations on Lead Acrylic

(i) Transmission Characteristics of Lead Acrylic. The half value layer (HVL) of lead acrylic was determined for the 4 MV beam under conditions approaching "good geometry" (JO.). Lead acrylic sheets of various thickness were placed midway at 100 cm between the radiation source and a thimble ionization chamber. A 10 x 10 cm field at chamber position (200 cm from source) was used.

Figure 5.1.8 shows the relative transmission as a function of lead acrylic thickness. The HVL was determined to be approximately .63 cm equivalent to a linear attenuation coefficient of 0.107 cm^{-1}.

(ii) Effects of high Dose. Samples of lead acrylic were irradiated to about 1 million CGy using a Co-60 source. A slight yellow tint was observed without any reduction in transparency.

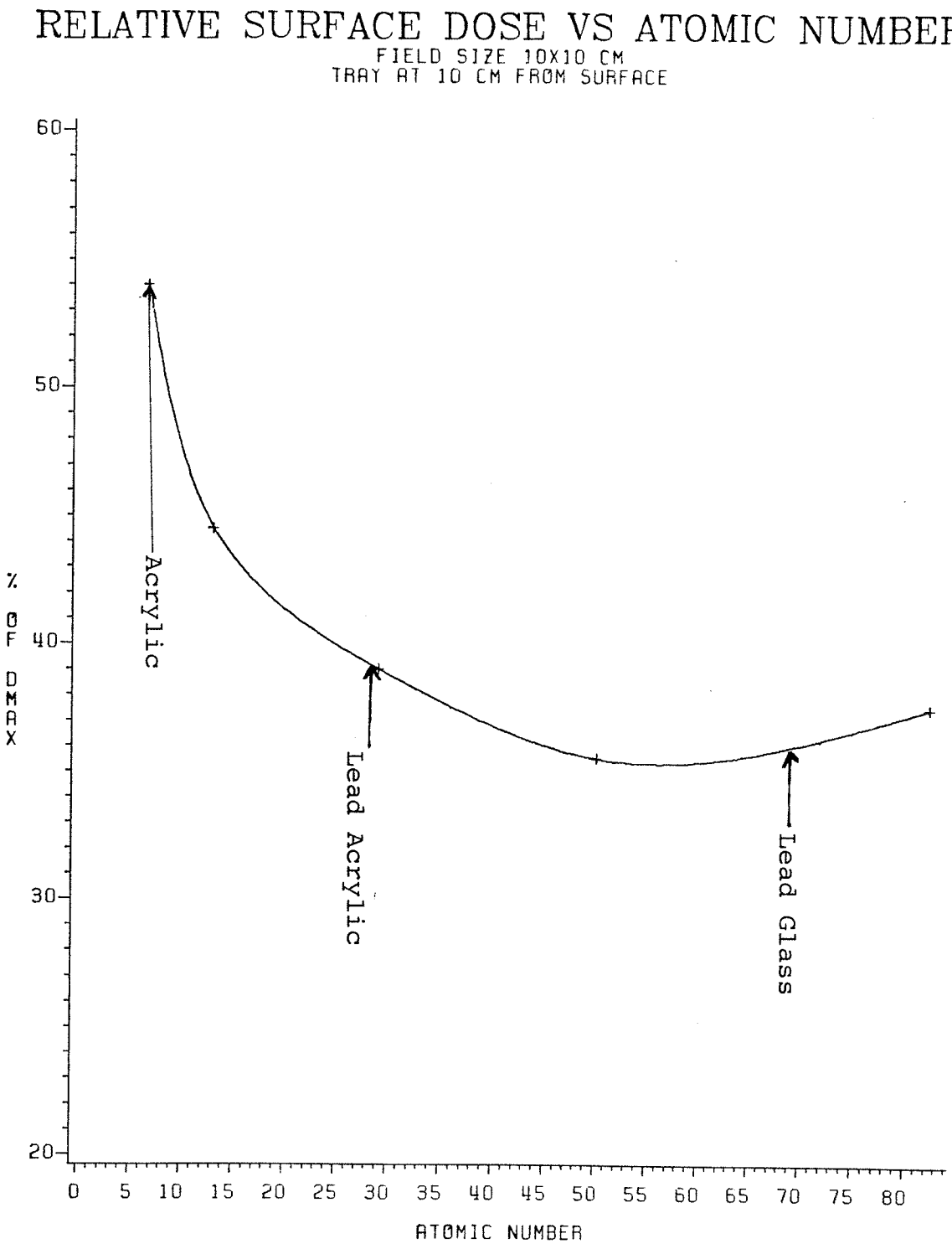
RELATIVE SURFACE DOSE VS ATOMIC NUMBER
FIELD SIZE 10X10 CM
TRAY AT 10 CM FROM SURFACE
% OF DMAX
60
50
40
30
20
0 5 10 15 20 25 30 35 40 45 50 55 60 65 70 75 80
ATOMIC NUMBER
Acrylic
Lead Acrylic
Lead Glass

Figure 5.17

Comparison Between Measured and Calculated RSD

S/cm	TSD/cm	Calculated RSD	Measured RSD	% Difference
5	10	23	22	+ 4.5
15	10	52	53	- 2
25	10	67	70	- 4
30	10	76	75	+ 1
5	20	17	16.5	+ 3
15	20	35	34	+ 3
25	20	49	50	- 2
30	20	55	57	- 3.5
5	40	123	13	- 5
15	40	26	26	0
25	40	36	36	0
30	40	40	40	0

TABLE 5.5

TRANSMISSION VS LEAD ACRYLIC THICKNESS

FIELD SIZE 10X10 CM
CHAMBER AT 200 CM FROM SOURCE
ACRYLIC SHEETS AT 100 CM FROM SOURCE

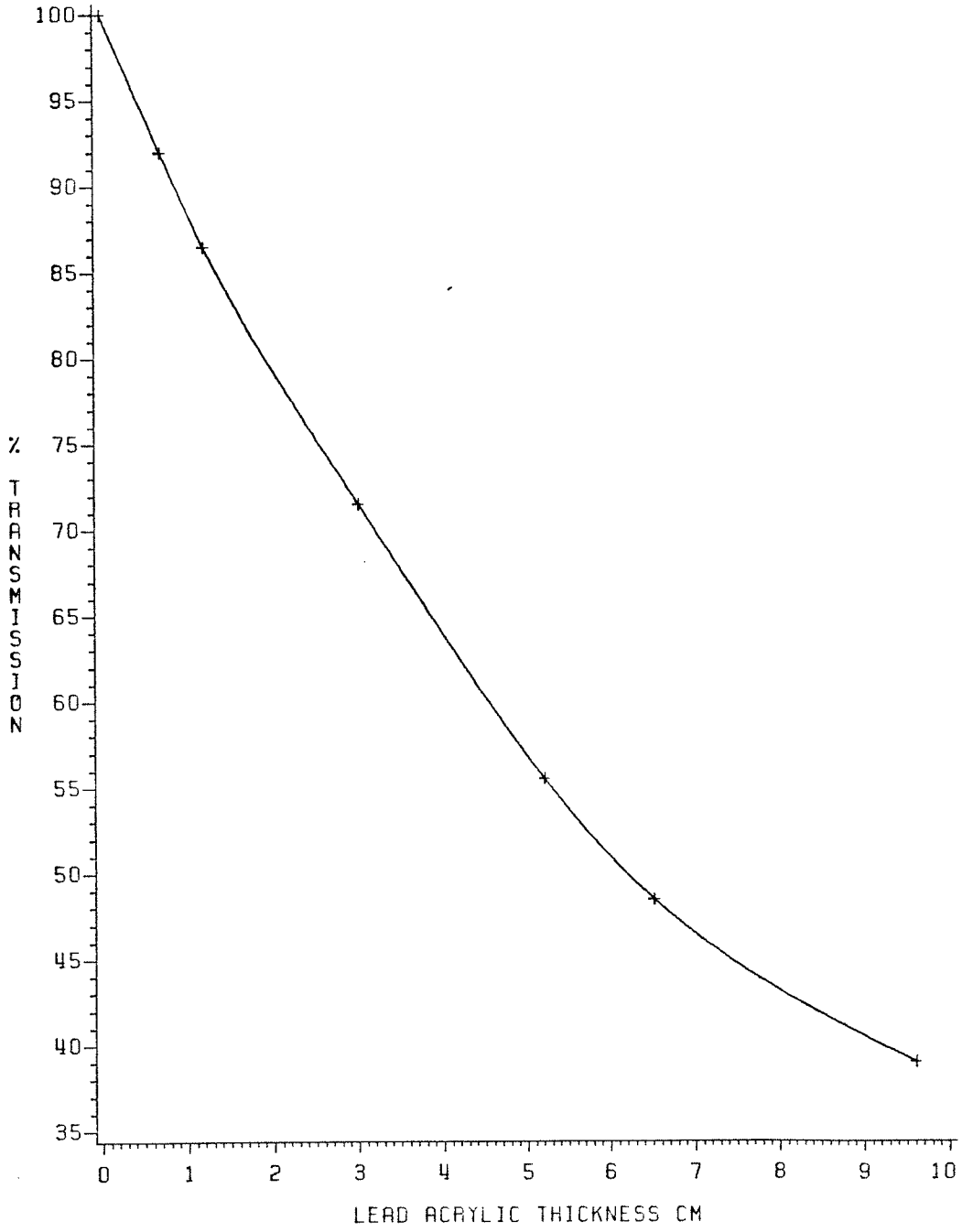

Figure 5.18

5.4 DISCUSSION

(i) The ionization at the surface of a phantom when no intervening material is present in the beam is due to secondary electrons originating from the flattening filter, the collimating system and the air through which the beam passes.

When a filter (tray) of thickness greater than the maximum range of the secondary electrons is introduced into the beam, all the incident electrons on the filter surface facing the beam source are completely absorbed. However, the photon beam transmitted through the filter becomes contaminated with electrons produced by photon interaction within the filter and in the air volume beyond the filter. Before reaching the skin surface (phantom surface), these electrons suffer further interactions in air with the result that some of them are absorbed or scattered. The remaining electrons deposit their energy on the skin surface and the underlying tissue layers.

The main interactions in air, copper and lead for photons of energies within the spectral distribution of 4 MV x-rays are shown in Table 5.6 (HU.). Compton interaction is the main mechanism for low and medium Z materials. For high Z materials the photoelectric effect is important (see Table 5.7). The maximum energy transferred to Compton electrons is given in Table 5.6.

Theoretically the range of 3 MeV electrons in acrylic material is approximately 1.3 cm (Table 5.7). However, it has been experimentally observed (GR.) that there is no change in RSD for a 4 MV

Photon Interactions In Air, Copper And Lead

Material	Energy MeV	% Interaction by* Compton	photo	pair	Maximum Energy Transferred To Compton Electron MeV
Air	0.5	99.6	0	0	0.4
	1.0	99.7	0	0	0.8
	1.5	99.8	0	0.2	0.85
	3.0	97.1	0	2.9	2.8
Copper	0.5	94.4	3.2	0	0.4
	1.0	98.4	0.7	0	0.8
	1.5	98.3	0.4	0.8	0.85
	3.0	88.0	0.2	11.6	2.8
Lead	0.5	42.5	51.1	0	0.4
	1.0	71.2	25	0	0.8
	1.5	79.2	16.0	3.1	0.85
	3.0	65.7	6.3	27.4	2.8

*Coherent Scattering is neglected from calculation

From Hubble (HU.)

Table 5.6

Range OF Electrons In Air And Acrylic For Variuos Electron Energies

Electron Energy (MeV)	Material	Electron Range* g cm^{-2}	cm
0.2	Air	5.07×10^{-2}	42.1
1	Air	4.91×10^{-1}	40.74×10^{1}
3	Air	1.65	13.72×10^{1}
0.2	Acrylic	4.52×10^{-2}	0.038
1	Acrylic	4.47×10^{-1}	.36
3	Acrylic	1.56	1.31

* From Bages et al (PAG.)

Table 5.7

photon beam when the thickness of acrylic is increased beyond 4 cm. Thus the 0.63 cm of lead glass, the 2.2 cm of lead acrylic and the 7.07 cm of acrylic used in this work were sufficient to absorb all incident electrons.

In this study no change in RSD was observed for lead acrylic tray thickness $\geq$ 1.2 cm. This indicates that electron contamination from the filter material has reached its maximum level and greater thickness will only serve to attenuate the x-rays.

(ii) Figure 5.14 clearly illustrates the rapid increase of relative surface dose with increasing field size. The increase in RSD for the open beam case is partially the result of Compton recoil electrons generated in the air. For smaller fields, these electrons tend to be scattered out of the field. For large field sizes, this out-scattering is compensated by other electrons scattering "in" toward the axis from the peripheral regions. More electrons are thus retained in larger beams.

A similar argument applies to the introduction of filters into the beam. That is an increase in field size increases the irradiated area of the filter resulting in greater numbers of electrons scattered towards the center of the beam.

(iii) Figure 5.7 - 5.12 show that a reduction in surface and buildup dose can be achieved if the filters are placed at greater distances from the skin surface. This reduction is due to a decrease in the solid angle subtended by the irradiated filter and an increased absorption and scatter of low energy electrons by the air between the filter and the surface.

(iv) The mean square scattering angle of the recoil electrons produced in the filters increases with effective atomic number. Consequently there is a reduction in the numbers of electrons scattered toward the center of the field for lead acrylic and lead glass.

Under the above conditions ((ii),(iii),(iv)) build-up curves for lead acrylic and lead glass filters may be superior to open beam conditions for small and moderate field sizes. Reflecting a reduction in the collimator system and air scattered electrons reaching the surface due to absorption and scatter in the filters.

(v) As an electron filter, lead glass shows the strongest filtering action for all TSD and field sizes, at depth as well as on the surface. Lead acrylic is less effective than lead glass for reducing surface and build-up doses, but is far superior to acrylic.

(vi) As a shadow tray lead glass material is impractical because it is brittle. Due to their strength, acrylic and lead acrylic are eminently suitable for this prupose. However, the use of acrylic as a shadow tray results in excessive electron contamination especially for large field sizes, thus reducing the skin sparing effect of high energy photon beams. To try to overcome this problem, acrylic shadow trays are placed at large distances from the skin. Unfortunately, the advantage of this procedure is offset by penumbra considerations for which it is desirable to have the TSD as small as possible. It is also limited due to machine constraints. Replacement of acrylic shadow trays by lead acrylic is advantageous since shorter

TSD for equivalent changes in the build-up region can be achieved together with lower electron contamination.

(vii) A second method to overcome the reduction in skin sparing by the use of acrylic as a shadow tray is to place an electron filter such as copper or lead glass underneath it, However, this method is disadvantageous since metallic filters are opaque and interfere with the light localization of the beam. In addition, lead glass is operationally inconvenient and is an additional source for attentuation of the beam resulting in increased treatment time.

Chapter 6. Scattered Radiation Outside the Field Boundary from Supporting Trays

6.1 INTRODUCTION

Secondary photons and electrons scattered by the collimating system, the shadow tray, and the air volume will not be limited to the boundaries of the collimated field size. The existence of high surface doses outside the field has been noted by several workers for cobalt 60 beams (BH.), (SM.) for an 8 MV accelerator (PU.), (SC.) and for a 42 MV betatron (BH.). As pointed out by these authors, high doses in this region are often overlooked and may contribute unnecessary radiation to sensitive organs such as the eyes and the testes. This dose is increased when shadow trays are placed in the beam. Scrimger, 1979, (SC.) studied the magnitude and distribution of radiation scattered outside the beam by materials placed in the beam for cobalt-60 and 8 MV x-rays. He noted the reduction of dose levels with higher Z materials and increased TSD.

Using the Fermi-Eyges theory of multiple scattering, Nelsson and Brahme, 1979 (NI.) calculated the contribution to the surface dose outside the field from secondary electrons produced in the irradiated air volume for cobalt 60, 6 MV x-rays and 21 MV x-rays, concluding that about half of the dose outside the field originates from air-scattered electrons. They also calculated the effects of shadow trays placed in the beam and concluded that this is the major source of electrons scattered outside the field.

In this work, the radiation dose outside the field is compared for different shadow trays and electron filters.

6.2 MATERIAL AND METHODS

The magnitude of scattered radiation from acrylic and lead acrylic supporting trays outside the field boundary was measured for various parameters. These include distance outside field boundary, depth, field size, and tray-phantom surface distance. In addition the dose from scattered radiation to the eye lens has been estimated by simulation with both a Temex phantom and an anthropomorphic phantom.* The effectiveness of shielding with thin lead sheets was also investigated.

The experimental arrangement is shown in Figure 6.1. A Temex phantom was positioned at 100 cm distance from the target (SSD). The dimensions of the phantom extended well beyond the limits of the field sizes being studied.

A 1.18 gcm^{-2} acrylic sheet was placed on top of the phantom. This thickness was sufficient to produce maximum buildup for the reference point at the field center 'P'. Measurements were made at points 'M' outside field boundary and represented as a percentage of the maximum dose 'D_{max} at the point 'P'.

The following sets of measurements were made:

(i) Surface dose measurements (using LiF Teflon discs), as a function of distance from field boundary. These measurements were made for field sizes 5 x 5, 20 x 20, 37 x 37 cm, both without the

* Alderson Rando Phantom (male).

supporting trays and with the trays at 20 cm and 30 cm from phanton surface (see Figure 6.1).

(ii) Depth dose measurements using LiF Teflon discs placed underneath various thicknesses of acrylic sheets at 1,2 and 6 cm from field boundary (see Figure 6.1). The depth in phantom was taken to be relative to the front surface of the Teflon discs. The measurements were made for 20 x 20 and 37 x 37 cm fields with the trays at 20 cm from phantom surface.

(iii) Depth dose measurements using the thin window parallel plate ionization chamber embedded in a Temex phantom at the position indicated in Figure 6.2. The chamber center was at a distance of 4 cm from the boundary of 30 x 38 cm field at (160 cm SSD) at a height of 4 cm above the field center (see Figure 6.2). In this arrangement, the position of the chamber center simulates the position of the eyes of a patient during the treatment of a mantle field.

Successive layers of acrylic were added on top of the chamber, with depth in the phantom taken to be relative to the front plate of the chamber. Measurements were made both without the supporting trays and with the trays at 21, 30, 40.8 and 50 cm from phantom surface.

(iv) Eye dose measurements on a Rando phantom using LiF-100 chips for a field size of 30 x 38 cm and 160 cm SSD. The eyes of the phantom were at a distance of 4 cm from field edge. These measurements were repeated with the supporting trays placed in the field at a distance of 30 cm from the phantom surface, both with and

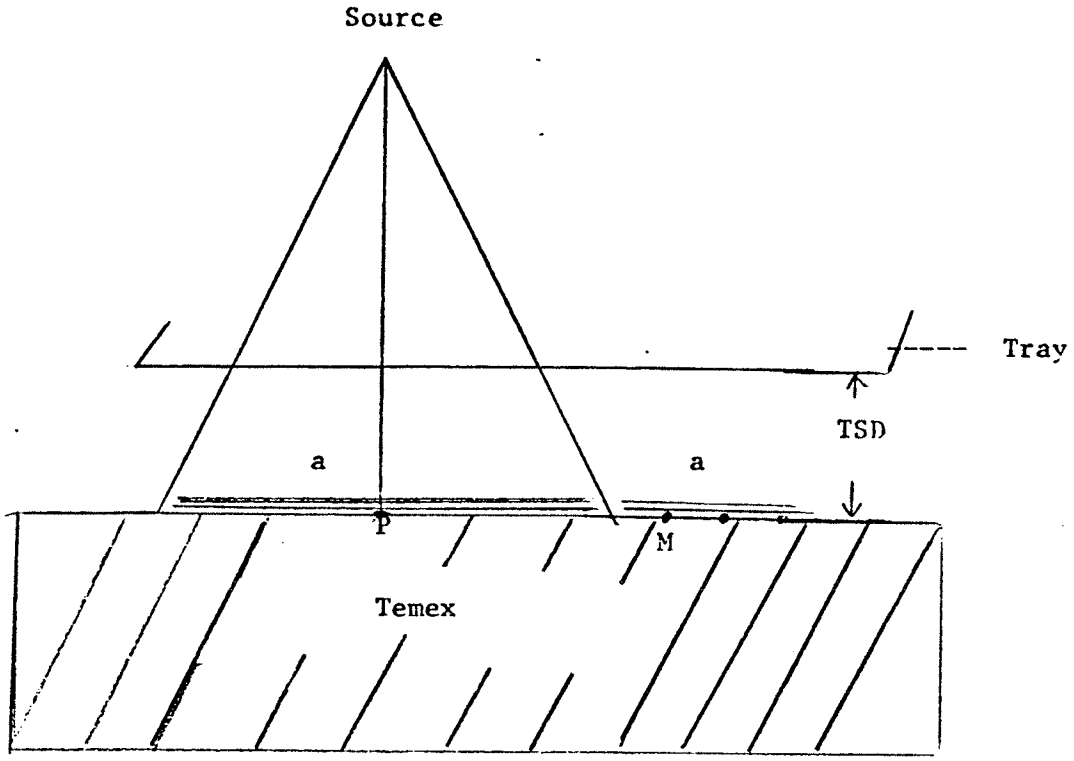

Figure 6.1

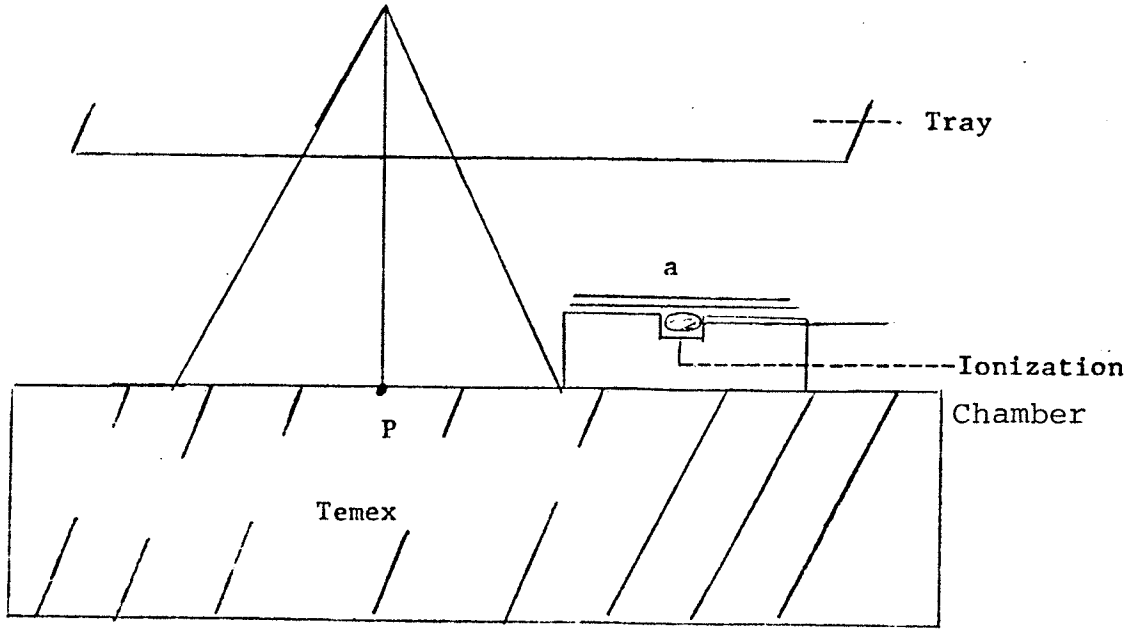

Figure 6.2 a Acrylic Sheets

without acrylic build-up caps (used to increase the effective depth of the TLD's surface to approximately 0.50 gcm^{-2}).

(v) Dose measurements using LiF-100 Chips and LiF Teflon discs placed on the eyes of two patients undergoing treatment with a mantle field.

(vi) Transmission measurements through various thicknesses of lead using LiF teflon discs placed at 2 and 6 cm from the boundary of 37 x 37 cm field at 120 cm SSD. These measurements were made with and without the supporting trays at 20 cm from the phantom surface.

Each absorbed dose measurement plotted on the curves represent the mean value of three LiF teflon discs or the mean value of two LiF-100 chips. Repeat measurements indicated a reproducibility of these results to within 5%.

6.3 RESULTS and DISCUSSION

6.3.1 Surface Dose outside the Field Boundary

Figures 6.3, 6.4 and 6.5 illustrate the surface dose as a function of distance from the field boundary for 5 x 5, 20 x 20 and 37 x 37 cm field sizes respectively. The intensity of scattered radiation can be seen to decrease as the distance from the field boundary increases. High energy photons transmitted through the collimator do not contribute to surface dose.

When acrylic and lead acrylic trays were introduced into the field an increase in the amount of scatter outside the field was observed, with acrylic producing higher scatter intensities than the lead acrylic. The main contribution to dose at the surface is due to secondary electrons produced by the trays.

SURFACE DOSE VS DISTANCE FROM FIELD BOUNDARY

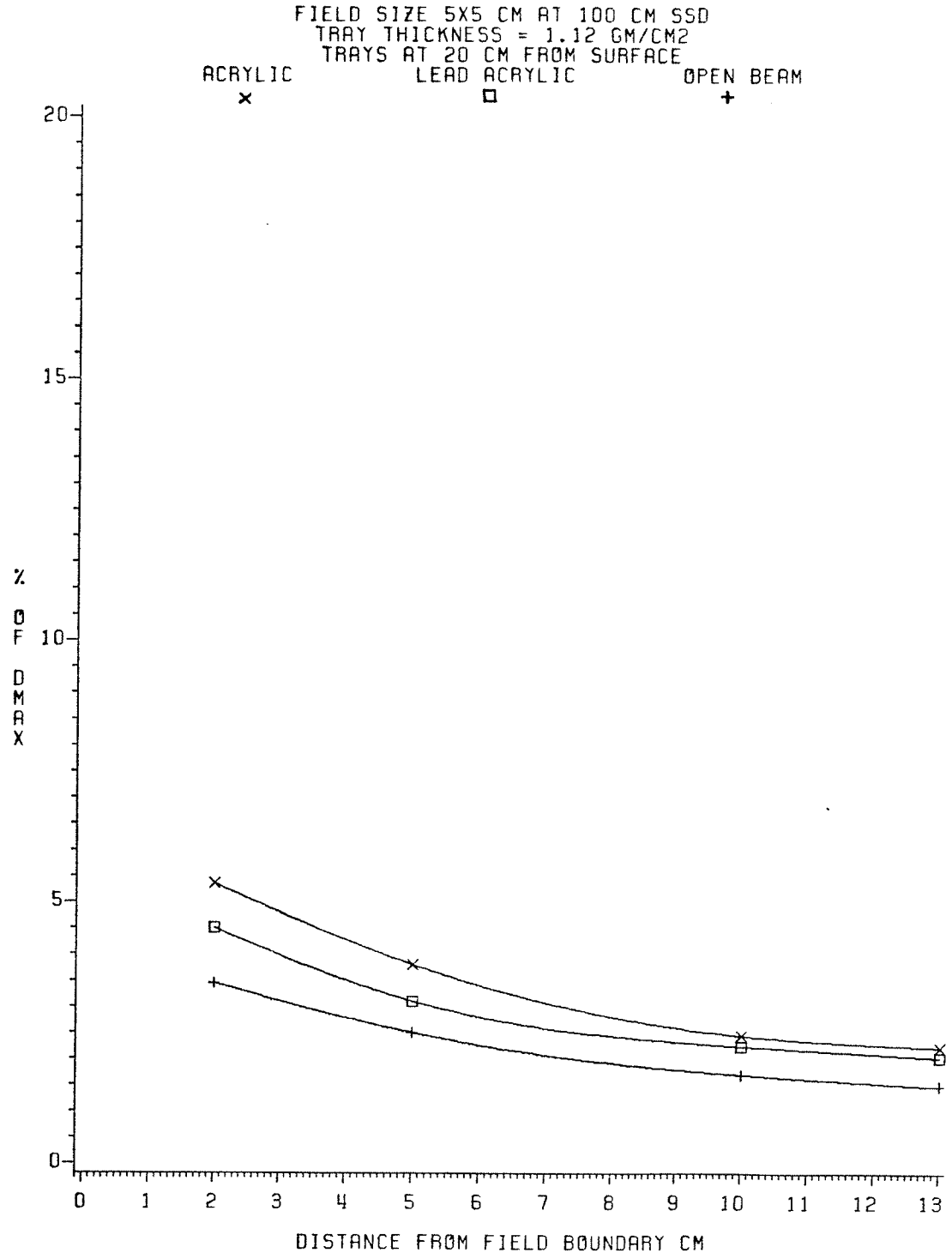

Figure 6.3

SURFACE DOSE VS DISTANCE FROM FIELD BOUNDARY

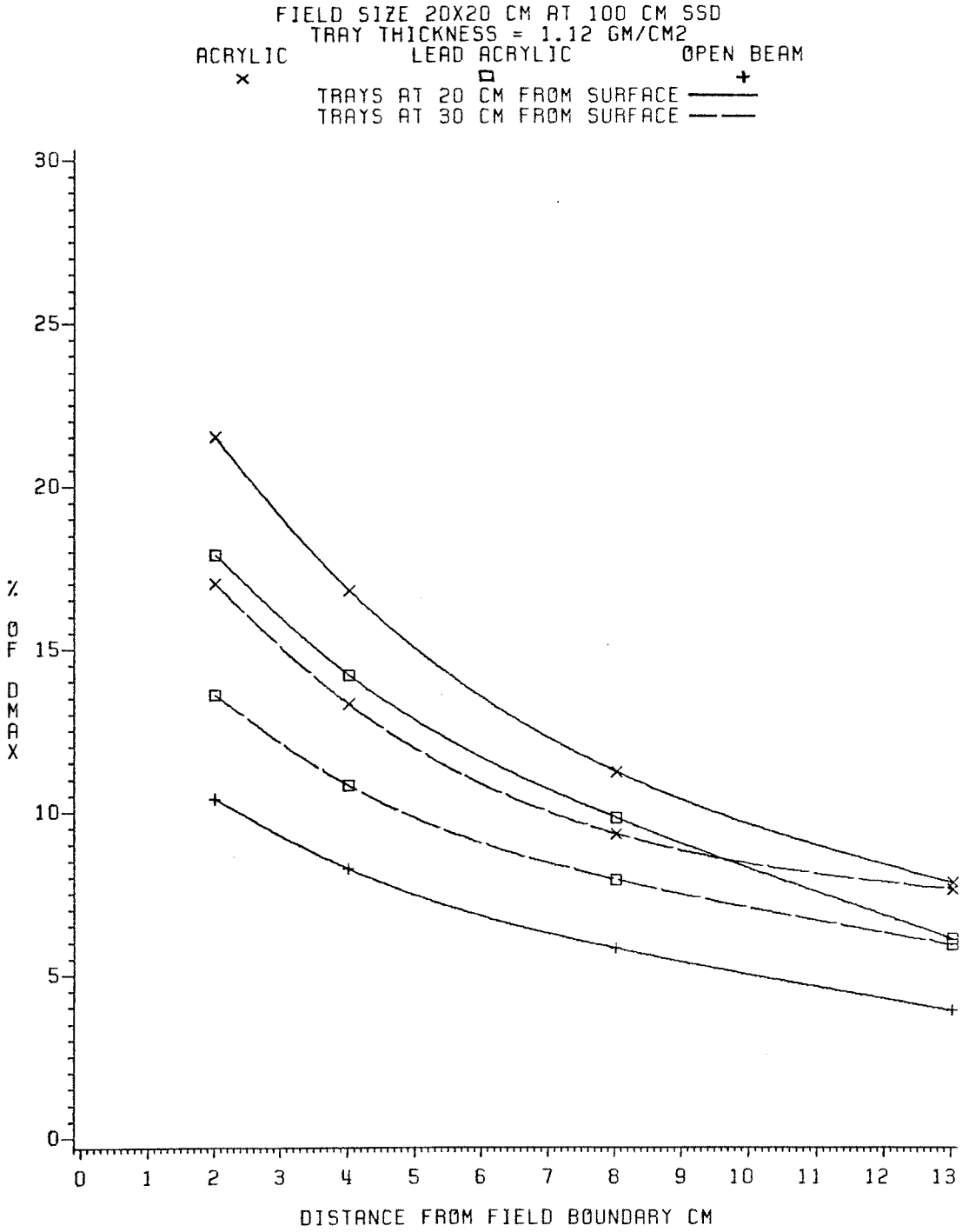

Figure 6.4

SURFACE DOSE VS DISTANCE FROM FIELD BOUNDARY

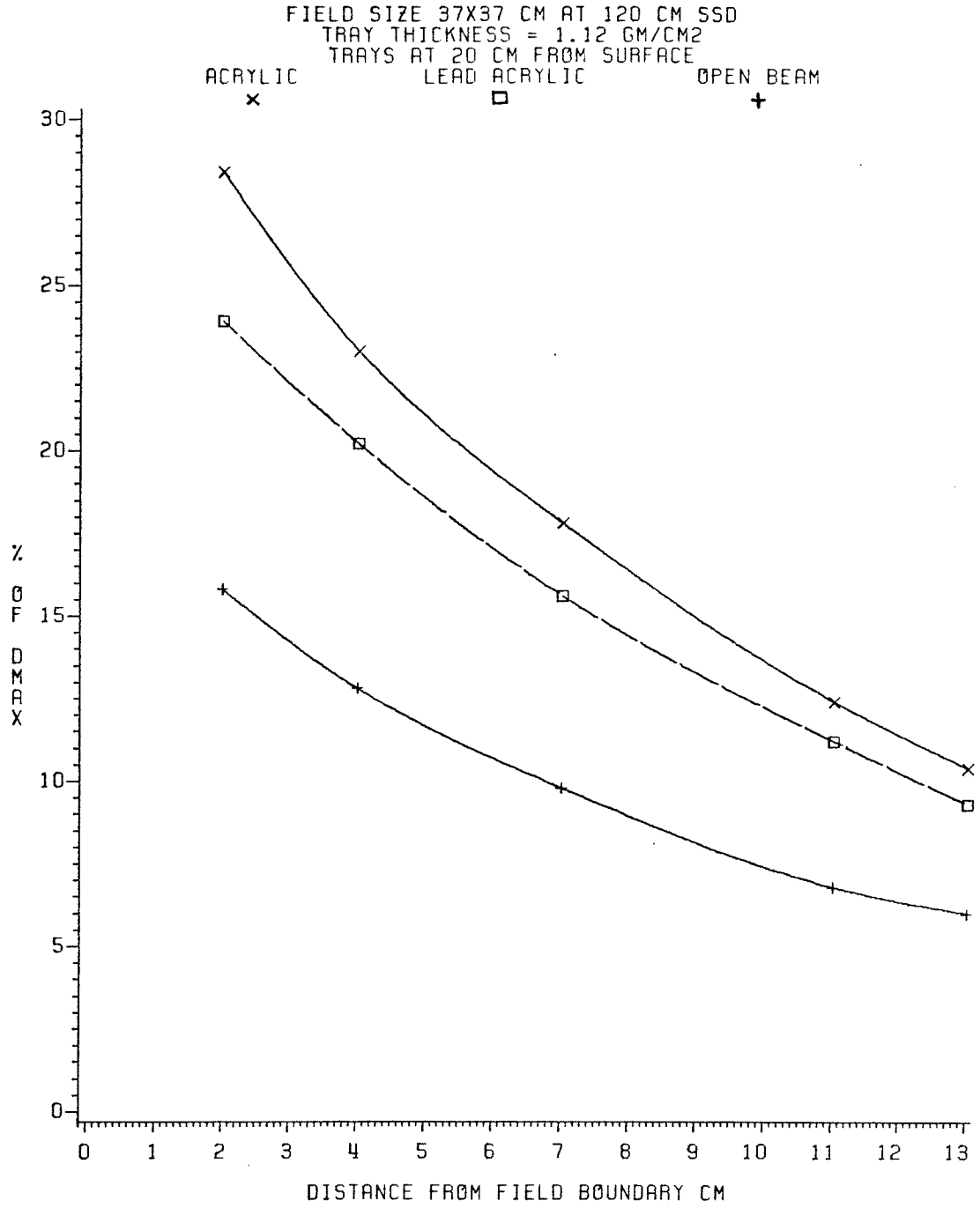

Figure 6.5

A reduction in tray-surface distance (TSD) results in significantly higher surface dose at points close to the field boundary, but has little effect at large distances from the boundary (Figure 6.4). Figure 6.6 shows the dependence of surface dose on TSD at 4 cm from 30 x 38 cm field boundary.

6.3.2 Depth Dose Outside the Field Boundary

Figures 6.7 - 6.10 illustrate the dose as a function of depth for distances of 1,2,4 or 6 cm outside the boundaries 20 x 20, 37 x 37, and 30 x 38 cm field. The dose initially falls off rapidly with depth and levels off at depths shallower than d_{max}. The presence of the trays in the field significantly increased the dose near the surface, with only small effects at depths greater than 0.5 gcm^{-2}. The shallow penetration of the elevated dose levels indicates that the main contributions to dose is secondary electrons produced by the trays. The residual dose at depths greater than the maximum range of the secondary electrons is due to high energy compton scattered photons from the trays and transmission through the collimators.

For a tray thickness of 1.2 gcm^{-2} the scattered photon contributions for acrylic and lead acrylic are almost identical. Increasing the thickness of the lead acrylic tray to 3.52 gcm^{-2} causes an increased scattered photon contribution to the depth dose (Figures 6.7, 6.8, 6.10).

The effect of TSD on depth dose is illustrated in Table 6.1 for 4 cm distance outside a 30 x 38 cm field boundary. Increase of the TSD from 20 to 30 cm produces a small increase in depth dose of

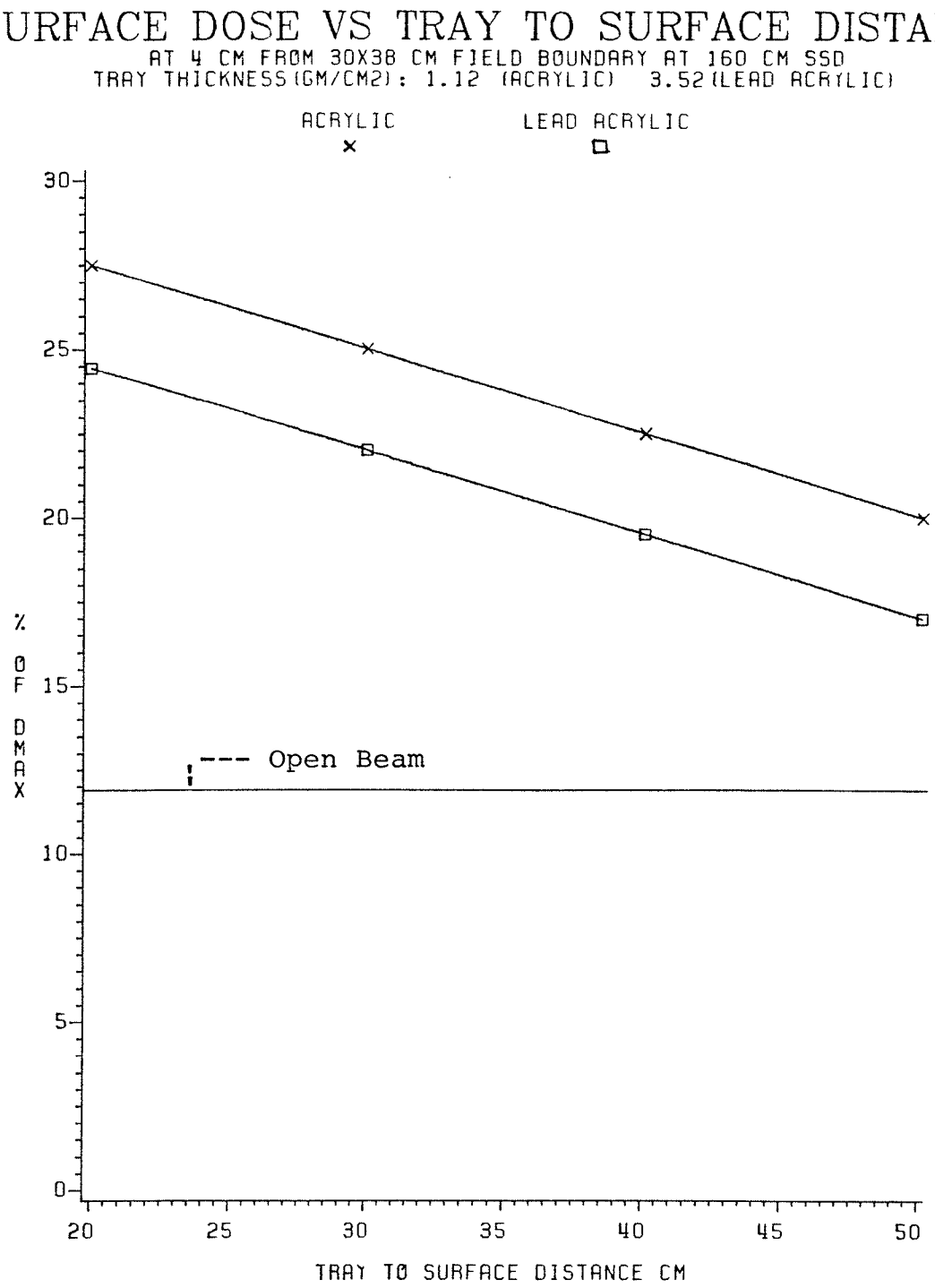
SURFACE DOSE VS TRAY TO SURFACE DISTANCE
AT 4 CM FROM 30X38 CM FIELD BOUNDARY AT 160 CM SSD
TRAY THICKNESS(GM/CM2): 1.12 (ACRYLIC) 3.52(LEAD ACRYLIC)
ACRYLIC
LEAD ACRYLIC
30
25
20
15
10
5
0
% OF DMAX
--- Open Beam
20
25
30
35
40
45
50
TRAY TO SURFACE DISTANCE CM

Figure 6.6

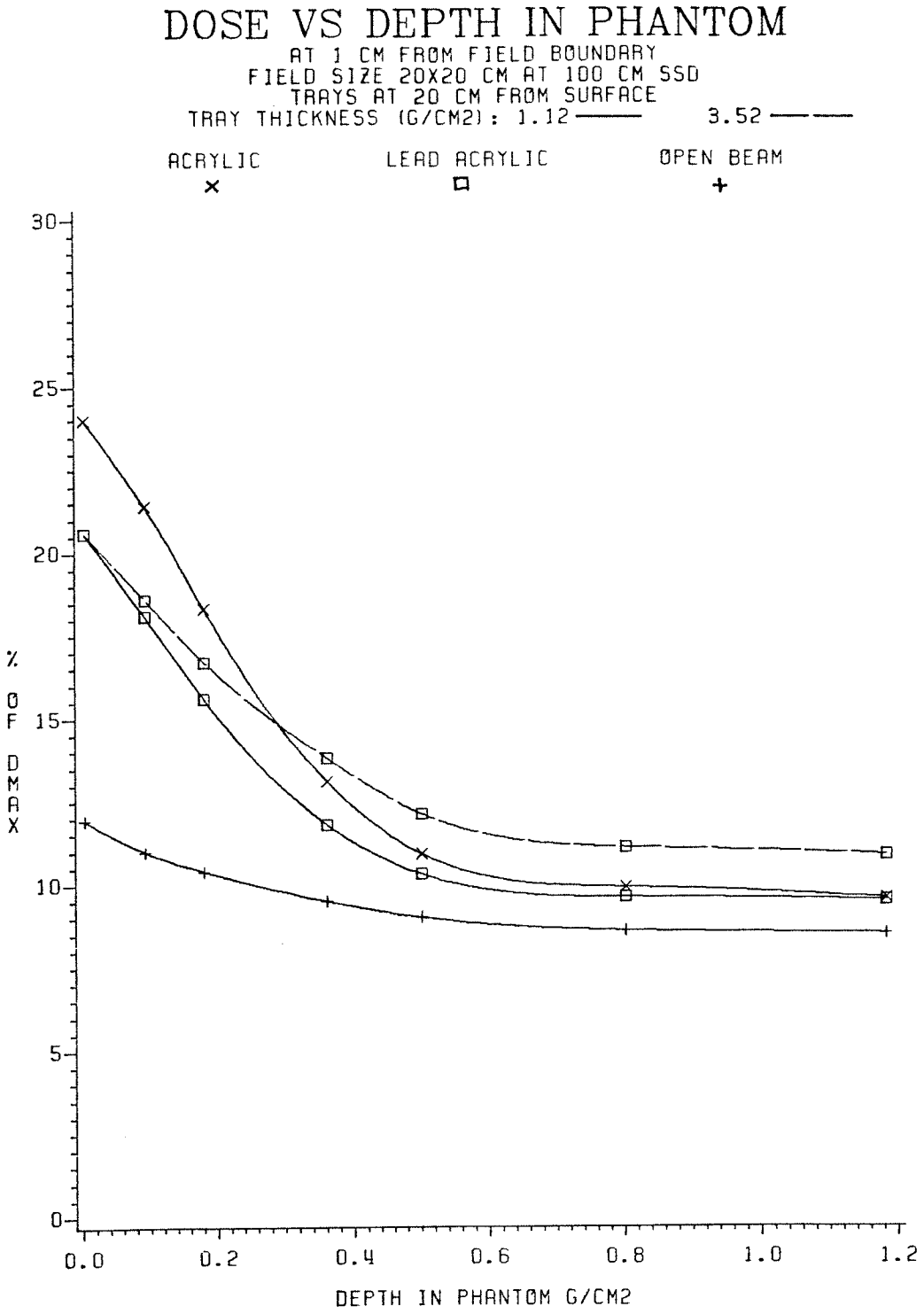
DOSE VS DEPTH IN PHANTOM
AT 1 CM FROM FIELD BOUNDARY
FIELD SIZE 20X20 CM AT 100 CM SSD
TRAYS AT 20 CM FROM SURFACE
TRAY THICKNESS (G/CM2): 1.12 —— 3.52 ——
ACRYLIC
LEAD ACRYLIC
OPEN BEAM
% OF DMAX
30
25
20
15
10
5
0
0.0
0.2
0.4
0.6
0.8
1.0
1.2
DEPTH IN PHANTOM G/CM2

Figure 6.7

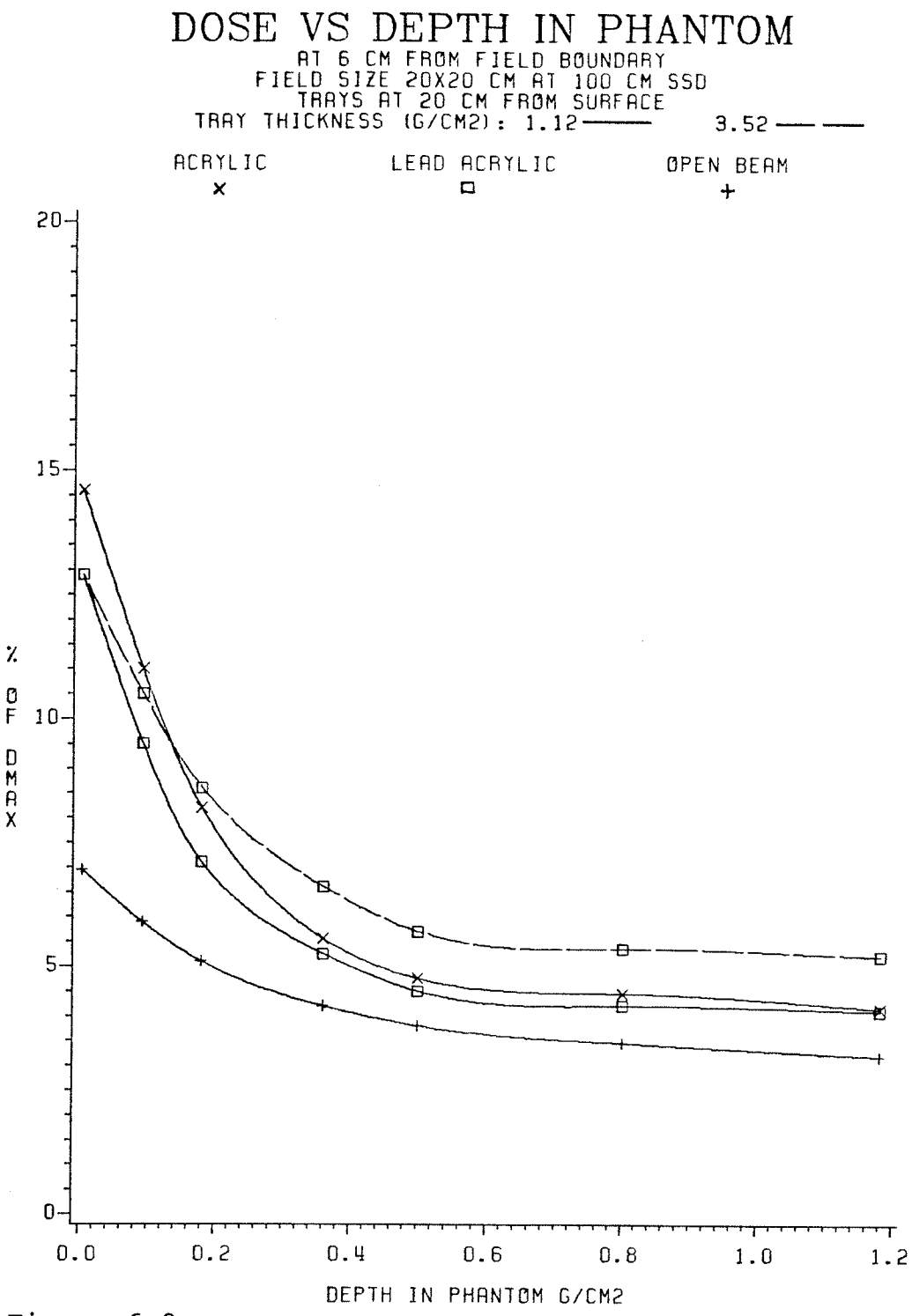
DOSE VS DEPTH IN PHANTOM
AT 6 CM FROM FIELD BOUNDARY
FIELD SIZE 20X20 CM AT 100 CM SSD
TRAYS AT 20 CM FROM SURFACE
TRAY THICKNESS (G/CM2): 1.12 3.52
ACRYLIC
LEAD ACRYLIC
OPEN BEAM
% OF DMAX
20
15
10
5
0
0.0
0.2
0.4
0.6
0.8
1.0
1.2
DEPTH IN PHANTOM G/CM2

Figure 6.8

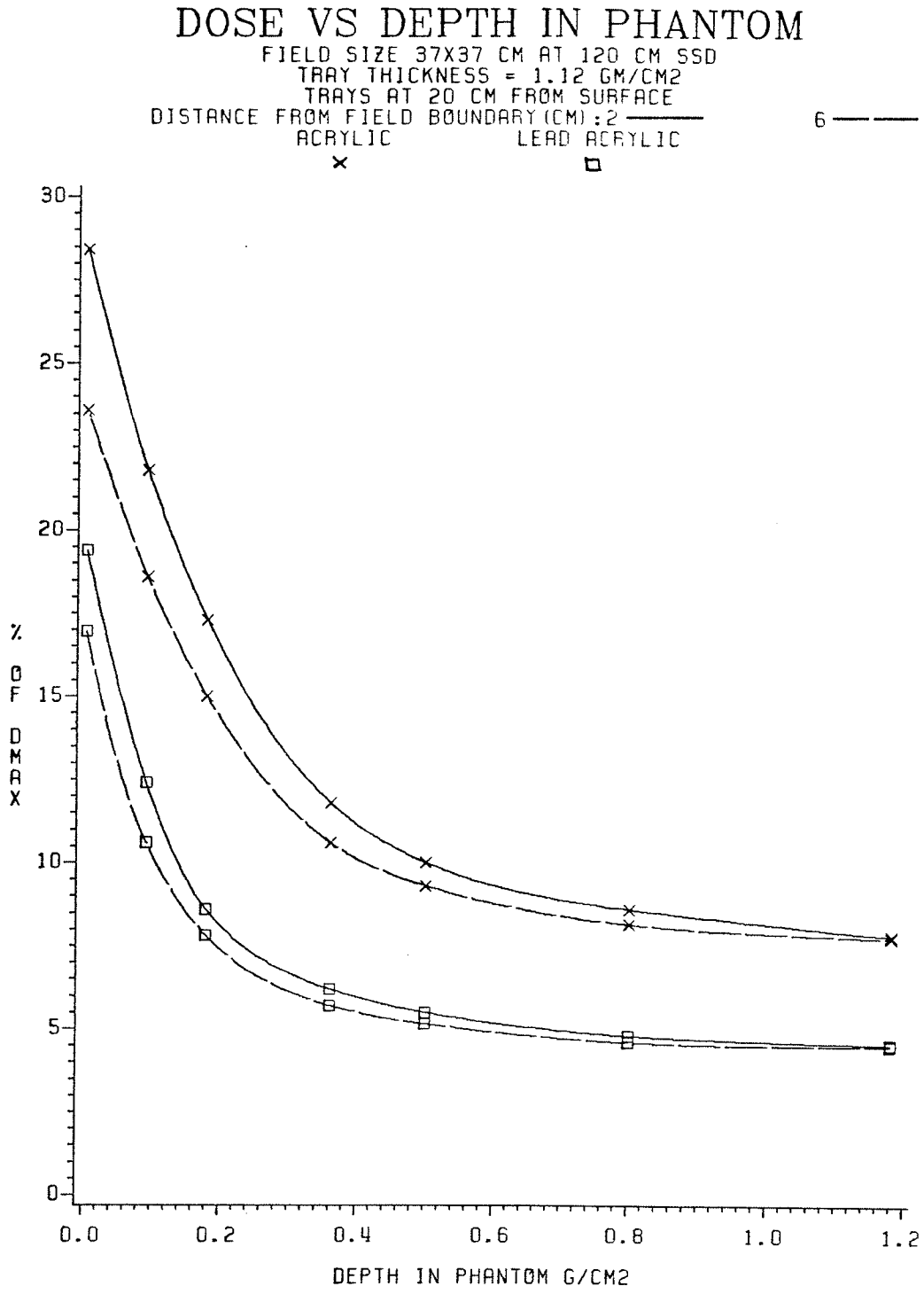
DOSE VS DEPTH IN PHANTOM
FIELD SIZE 37X37 CM AT 120 CM SSD
TRAY THICKNESS = 1.12 GM/CM2
TRAYS AT 20 CM FROM SURFACE
DISTANCE FROM FIELD BOUNDARY(CM):2
6
ACRYLIC
LEAD ACRYLIC
% OF DMAX
30
25
20
15
10
5
0
0.0
0.2
0.4
0.6
0.8
1.0
1.2
DEPTH IN PHANTOM G/CM2

Figure 6.9

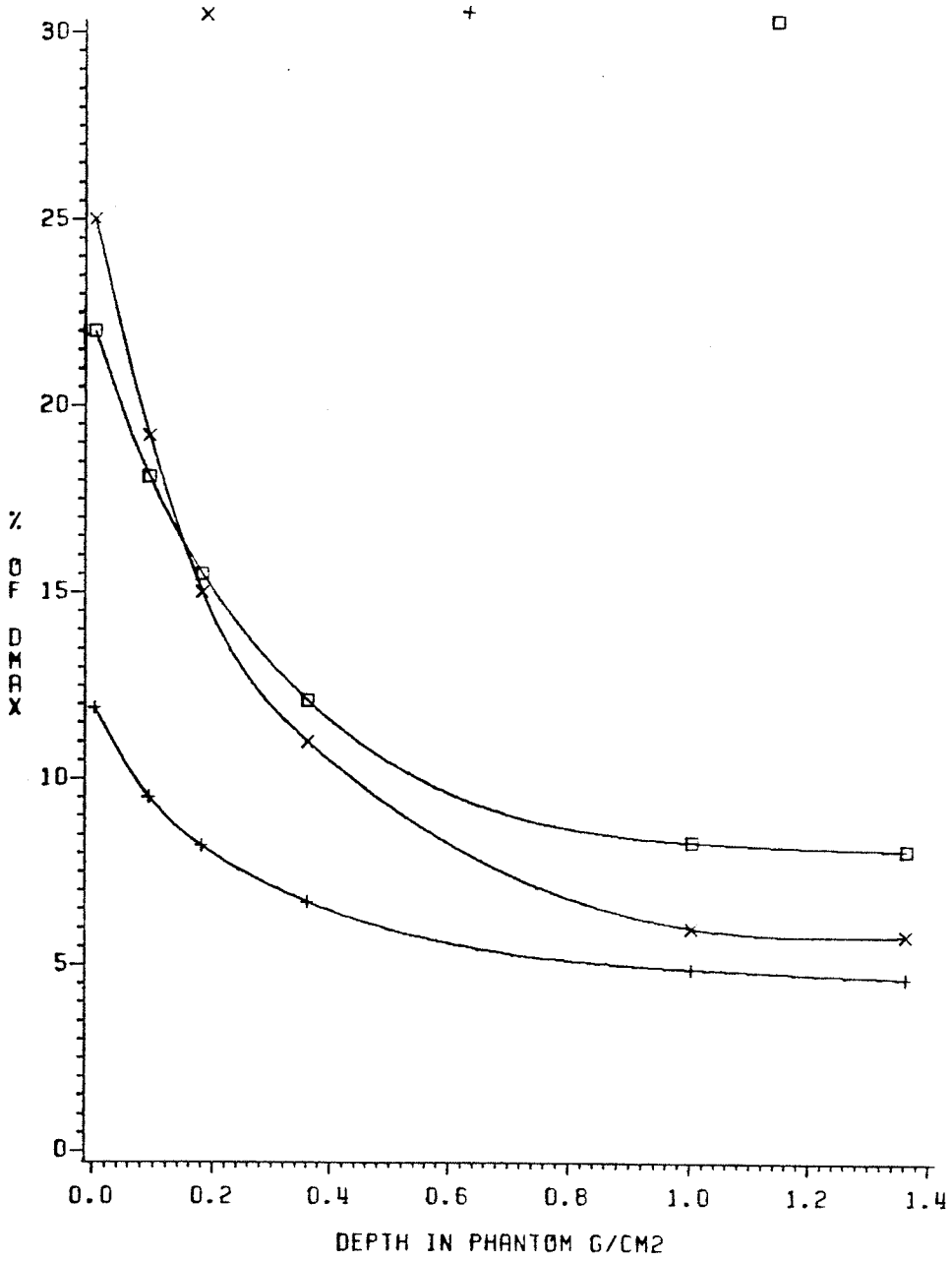
DOSE VS DEPTH IN PHANTOM
AT 4 CM FROM 30X38 CM FIELD BOUNDARY (160 CM SSD)
TRAYS AT 30 CM FROM SURFACE
TRAY THICKNESS (G/CM2):1.12 (ACRYLIC) 3.58(LEAD ACRYLIC)
ACRYLIC
LEAD ACRYLIC
OPEN BEAM
% OF DMAX
30
25
20
15
10
5
0
0.0
0.2
0.4
0.6
0.8
1.0
1.2
1.4
DEPTH IN PHANTOM G/CM2

Figure 6.10

$\leq$ 3% for both acrylic and lead acrylic trays. Decreases of TSD from 50 to 30 cm however, results in greater change in depth dose.

6.3.3 Transmission through Lead

Table 6.2 shows the percentage transmission of scatter radiation through varying thicknesses of lead at 6 cm and 2 cm distance from 37 x 37 cm field boundary. The intensity of scatter radiation is seen to drop sharply when a few millimeters of lead were added on top of the teflon discs. Thus the soft component of the scattered dose from a tray comprising approximately 2/3 of the total scatter may be removed by placing 1 mm of lead on the surface of the phantom. The addition of 3 mm of lead reduces the surface dose to 4.5 percent of D_{max} for both acrylic and lead acrylic trays (Table 6.3).

6.3.4 Eye Dose

Table 6.4 shows the results of eye dose measurements performed on the Alderson Rando phantom. The thickness of LiF TLD chips was approximately 0.23 gcm^{-2} (0.09 cm) and consequently, the effective depth of measurement with and without the build-up cap (0.5 gcm^{-2}) was taken to be 0.12 and 0.62 gcm^{-2} respectively. For 0.12 gcm^{-2} effective depth the acrylic tray (1.12 gcm^{-2}) showed an eye dose increase of about 9% over that of the lead acrylic tray (3.52 gcm^{-2}). However, at 0.62 gcm^{-2} effective depth the lead acrylic tray produced a dose increase of about 20% over that of acrylic.

Table 6.5 shows the results of eye dose measurements

% TRANSMISSION THROUGH VARYING THICKNESSES OF LEAD

Lead Thickness mm	Acrylic ($1.12\ g\ cm^{-2}$)		Lead Acrylic ($1.12\ g\ cm^{-2}$)		Open Beam	
	Distance from field boundary (cm) #					
	2	6	2	6	2	6
0	100	100	100	100	100	100
1	33 ± 2	28 ± 1	38 ± 2	31 ± 1.5	53 ± 2.5	41 ± 1.5
2	29 ± 1	26 ± 1.5	34 ± 1	28 ± 1	48 ± 1	36 ± 2
3	27 ± 2	25 ± .5	32 ± 1.5	27 ± 1.5	45 ± 1.5	35 ± 1
4	26 ± 0.8	24 ± 1	31 ± .9	26 ± 1.5	43 ± 2	34 ± 2

TABLE 6.2

TRANSMISSION THROUGH 3mm LEAD AT THE SURFACE (% of D_{MAX})

Distance From Field Boundary #	Acrylic ($1.12\ g\ cm^{-2}$)	Lead Acrylic ($1.12\ g\ cm^{-2}$)	Open Beam
2	7.6 ± .1	7.6 ± .2	7.4 ± .2
6	4.5 ± .2	4.5 ± .2	4.3 ± .1

Field size 37 x 37 cm at 120 cm SSD
Trays at 20 cm TSD

TABLE 6.3

EYE DOSE TO RANDO PHANTOM

Effective Depth of Measurement g cm^{-2}	Percent of D_{max} .12	0.62
Open Beam	8.9 ± .1	4.8 ± .2
Acrylic tray (thickness=1.12 g cm^{-2})	17.5 ± .3	6.8 ± .2
Lead Acrylic tray (thickness=3.52 g cm^{-2})	16 ± .3	8.5 ± .1

TABLE 6.4

Patient Eye Dose from Anterior Mantle Field

Patients	Open Field Size at 150 SSD (cm)	Tray-Skin Distance (cm)	Distance of Eye from Field Boundary (cm)	% of D_{max} at depth .014 g/cm^{-2}		% of D_{max} at depth .12g/cm^{-2}	
	Tray			Acrylic	Lead acrylic	Acrylic	Lead Acrylic
	Tray Thickness			0.9 g/cm^{-2}	1.12 g/cm^{-2}	0.9 g/cm^{-2}	1.12 g/cm^{-2}
1	28 x 34 cm	33	9	10.6 $\pm$ .3	9.2 $\pm$ .3	7.2 $\pm$ .25	6.4 $\pm$ .1
2	31 x 36 cm	34.2	6	12.6 + .2	10.7 + .2	9.5 + .25	8.4 + .2

TABLE 6.5

DEPTH DOSE FOR VARIOUS TRAY-SURFACE DISTANCES*

(% of D_{max})

Depth g cm^{-2}	TSD cm	Lead Acrylic Tray (3.52 g cm^{-2} thickness)	Acrylic Tray (1.12 g cm^{-2} thickness)	Open Beam
0.18	50	13	14	8.2
0.36	50	10	10	6.7
1.00	50	7	5.2	4.8
0.18	30	15.5	15	8.2
0.36	30	12.1	11	6.7
1.00	30	8.2	6	4.8
0.18	20	15.7	15.2	8.2
0.36	20	12.2	11.2	6.7
1.00	20	8.4	6.1	4.8

* Field size 30 x 38 cm at 160 cm SSD. Ionization chamber was at a distance of 4 cm from field boundary.

TABLE 6.1

performed on two patients undergoing treatment with an anterior mantle field, the thicknesses of lead acrylic and acrylic trays used were 1.12 and 0.9 gcm^{-2} respectively. LiF Teflon discs and chips were placed on both eyes of the patient and the average dose at both eyes was calculated. The acrylic tray produced an increased dose of about 15% at the surface and 12% at a depth equal to 0.12 gcm^{-2} over that of lead acrylic.

The clinical significance of the scattered dose to the eye may be evaluated as follows:-

The contribution of scattered radiation arriving at the eyes of a patient eye treated by an anterior mantle field is approximately 12.6 and 10.7% of D_{max} for acrylic and lead acrylic respectively with the eye positioned at 6 cm from the field boundary (Table 6.2). The eye dose from the posterior field was measured to be 2.3% of D_{max} for both trays. The given dose for both the anterior and posterior fields is commonly 2540 cGy. Hence the patient's eye would receive a total dose of 378 and 330 cGy for acrylic and lead acrylic respectively.

The epithelial cells in the equatorial region of the eye's lens are responsible for cataract formation. In normal adults (20 - 65 years) the minimum depth of the epithelial cells is 0.23 ± 0.04 gcm^{-2} (CH.). The scatter contribution at a minimum cell depth (0.19 gcm^{-2}) varies from about 60 to 47% of the surface dose for 2 and 6 cm distant from field boundary respectively. Thus the anterior field contribution to the lens dose would be reduced to 150 cGy (47% of 320) and 128 cGy (47% of 272) resulting in a total dose of 208 and 186 cGy for acrylic and lead acrylic respectively. A 3 mm lead sheet thickness

placed on the eyes would reduce the anterior field contribution to 114 cGy (4.5% of D_{max}, Table 6.3), which coupled with the posterior contribution of 58 cGy would be a total of 172 cGy for both trays. Without attenuation of the incident radiation, the 378 cGy for an acrylic tray exceeds the nearly 350 cGy set by Marriam and Focht (ME.) as the lower limit for cataract formation. For a typical mantle field, with the field boundary at least 6 cm from the eye, the dose to the lens is probably less than 210 cGy, and Merriam's data suggest that this level is above the threshold for cataract formation. Although no cases of radiation-induced cataracts in patients treated with mantle fields are known, scattered radiations to the eye may approach the low limit reported by Merriam. Fortunately, this risk can be reduced by simply applying external eye shields (lead) during treatment of the anterior mantle field.

Chapter 7. Blocking Considerations in Large Irregular Fields

7.1 INTRODUCTION

Radiation therapy of large partially blocked irregular fields is currently employed for special radiotherapeutic situations. For example, the entire supradiaphragmatic lymph node region may be treated in the malignant Hodgkin's disease in a field commonly referred to as the 'mantle' field. In treatment of this disease, individually designed lead blocks are placed in a large radiation field to shield radiation sensitive structures (such as lungs), from the incident photon beam (see Figure 1.3). Sometimes lymph nodes lie very close to the lungs. Since underdosing may lead to recurrence of tumor (MAR.) shielding blocks must be accurately positioned to protect lung tissue and yet provide the prescribed radiation dose to be delivered to these lymph nodes.

In order to achieve dose uniformity in the treated area with minimized dose to surrounding normal tissue, the penumbra formed by the edge of the shielding blocks must be reduced to the minimal width. This could be achieved by a small block skin distance BSD. However, placing the shielding blocks closer to the patient surface will result in an increased number of secondary electrons, produced in the block supporting tray, reaching the patient surface and result in a reduced skin sparing effect.

Present radiotherapy treatment strategies designed to overcome this problem involve either:

(i) the use of lead blocks having edges sloped to match the beam divergence, placed on shadow trays at large BSD. This is thought to be advantageous with linacs due to their small source size (usually 0.3 cm).

or (ii) the use of straight edged lead blocks placed on a bridge at shorter BSD.

In order to determine which of the above two strategies is best, penumbra width was measured as a function of BSD using both diverging and straight edge cut lead blocks. In addition, the measured beam profiles across the penumbra regions were fitted to semi-empirical expressions used in the calculation of dose distributions for irregular shaped fields at the Manitoba Cancer Treatment and Research Foundation (TH.).

7.2 EFFECTS ON THE BEAM PROFILE

The beam profile at the edge of the field is determined by the geometrical penumbra, transmission penumbra and decreased contribution of scattered radiation at the edge and beyond the edge of the field.

The geometrical penumbra width P, formed by the edge of the block, is affected by BSD, SSD and the source size S (Figure 7.1), (IC2.)

$$P = S \frac{BSD}{(SSD-BSD)} \qquad (7.0)$$

Transmission penumbra is affected by the angle of the lead block

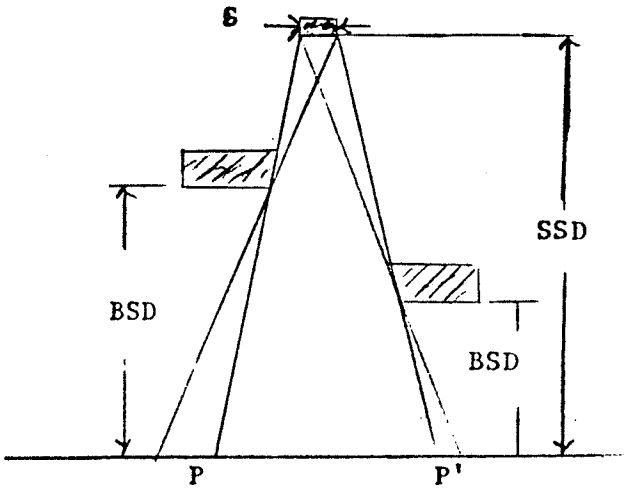

Figure 7.1 Geometrical penumbra formed by the edge of the block.Penumbra width P given by equation 7 is dependent on source size S,distance of the block from the skin BSD,and SSD.Decreasing BSD results in smaller penumbra width P'.

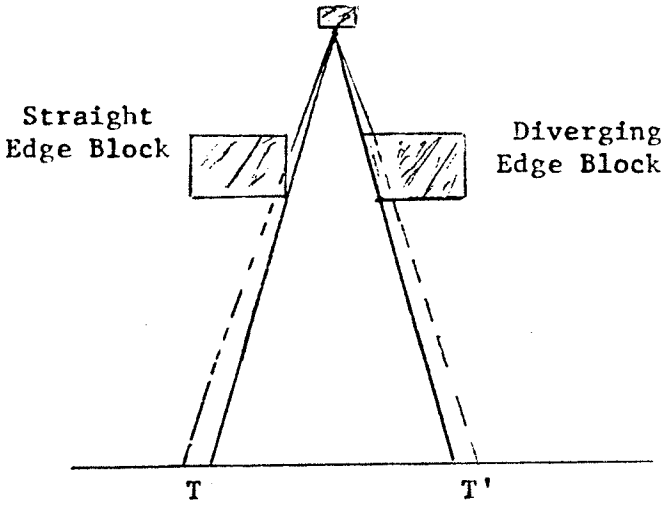

Figure 7.2 Shows the effect of block shape on Transmission penumbra.A diverging block with its face paraller to the rays from the source of radiation causes less transmission T' than the straight edge block.

edge facing the beam. If this edge follows the divergence of the beam the transmission penumbra is reduced. Detailed illustration of this effect is given in Figure 7.2.

The beam profile may be characterized by the penumbra width which may be defined as the distance between the 90 and 30% relative dose and the separation distance between the geometrical edge of the beam and the 50% relative dose.

7.3 MATERIALS AND METHODS

7.31 Beam profiles across the inside edge of the block

Figure 7.3 shows the experimental set up used to measure the beam profiles across the inside edge of a lead shielding block. A 30 x 37.5 cm field was collimated by placing 5 cm thick lead blocks on an acrylic tray. The light field projected on the surface of a Temex phantom was 30 x 20 cm at 150 cm SSD. A specially designed aluminum wedge placed underneath the outside edge of the block was used to ensure that the block edge facing the central axis was correctly aligned with the beam divergence. Beam profiles in the direction of XX' were measured at depths of 4 and 10 cm. The edge of the illuminating light field (0) was set at distance d, 5 and 15 cm from the central axis at the level of the phantom surface (Figure 7.30). This was used to define the geometrical edge of the beam. The above measurements were repeated under the same geometrical conditions with the block edge straight and parallel to the central axis.

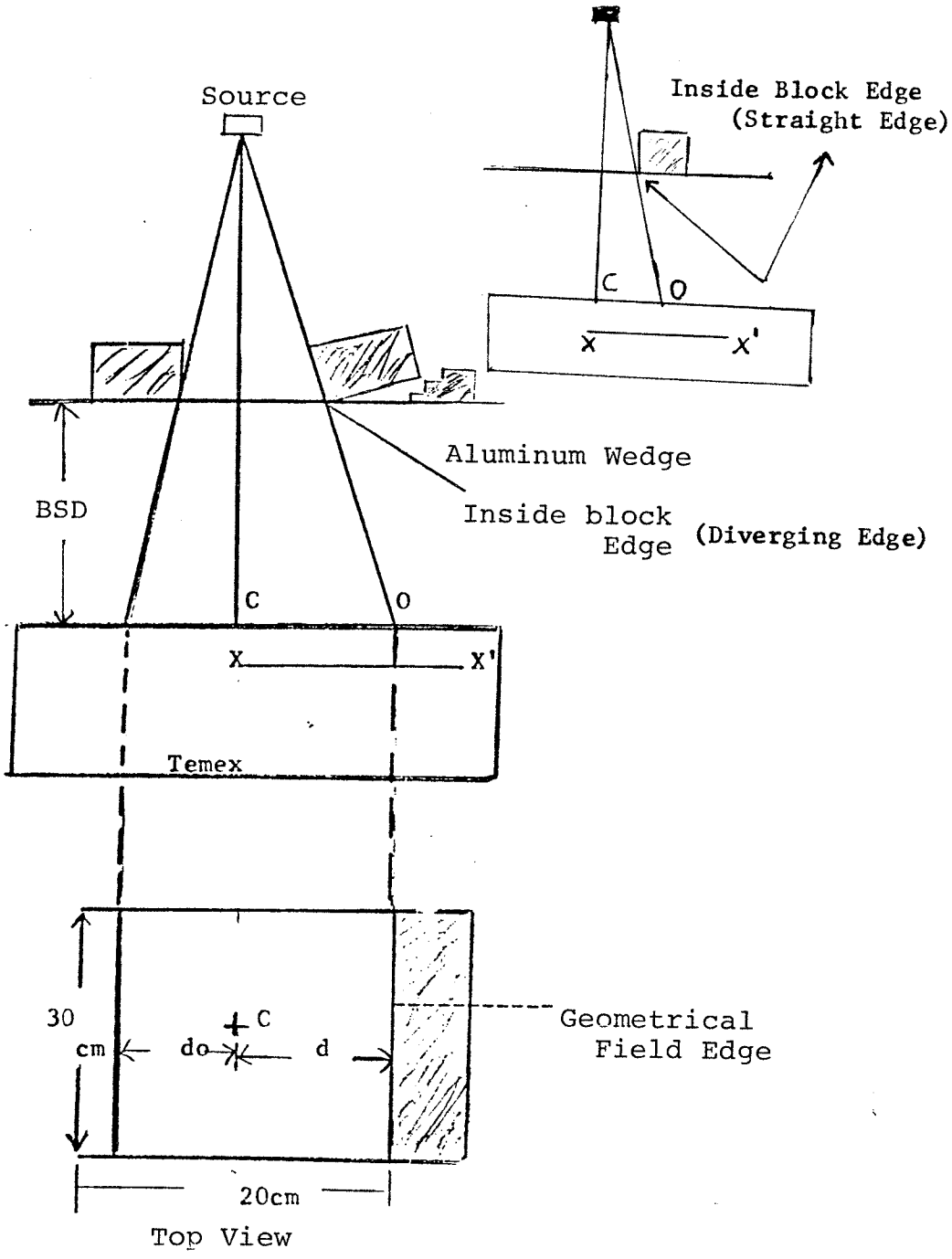

Figure 7.3 Experimental set-up to measure beam profile across the inside block edge.

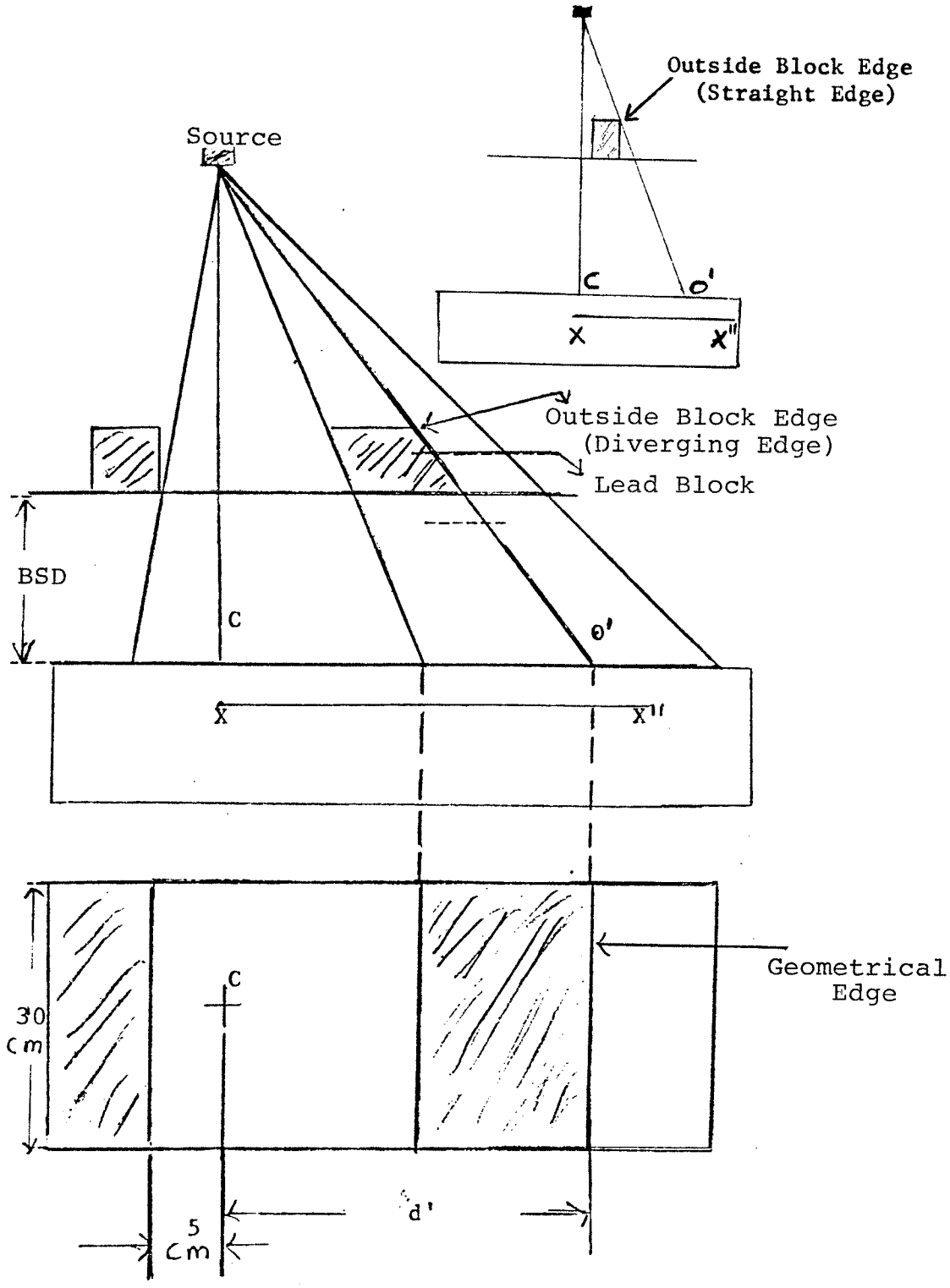

Figure 7.4 Experimental set-up to measure beam profile across the outside block edge.

7.32 Beam profiles across the outside edge of the block

Figure 7.4 shows the experimental set up used to measure beam profiles across the outside edge of a 5 cm thick lead block. The edges of the block were cut to match beam divergence. A field size of 30 x 39.5 cm at 150 cm SSD was collimated as shown in Figure 7.4. Beam profiles were measured along the direction XX'' at 4 and 10 cm depth with the edge of the illuminating light field (0') at a distance d', 10 and 15 cm from central axis at the phantom surface. The above meauremenents were repeated with the block edge parallel to the central axis. Beam profiles of penumbra for inside and outside edges of the block were measured with LiF extruded rods of 1 mm diameter with the blocks placed at 100.1, 40 and 20 cm distance from the phantom surface. All dose data measured was normalized to the central dose in the same plane.

7.4 RESULTS

7.41 Beam Profiles

Figures 7.5 - 7.8 show typical beam profiles across the field edge formed by diverging and straight block edges at 100.1 cm BSD. A rapid dose gradient across the field edge was observed for both inside and outside edges of the block. Within experimental error, no difference in penumbra width was observed between 90 and 30% relative dose for the diverging and straight block edges (Tables 7.1 and 7.2). The main difference noted was a shift in the position of the measured profiles. The geometrical edge of the beam was seen to be coincident with the 50% relative dose of the beam profile for the

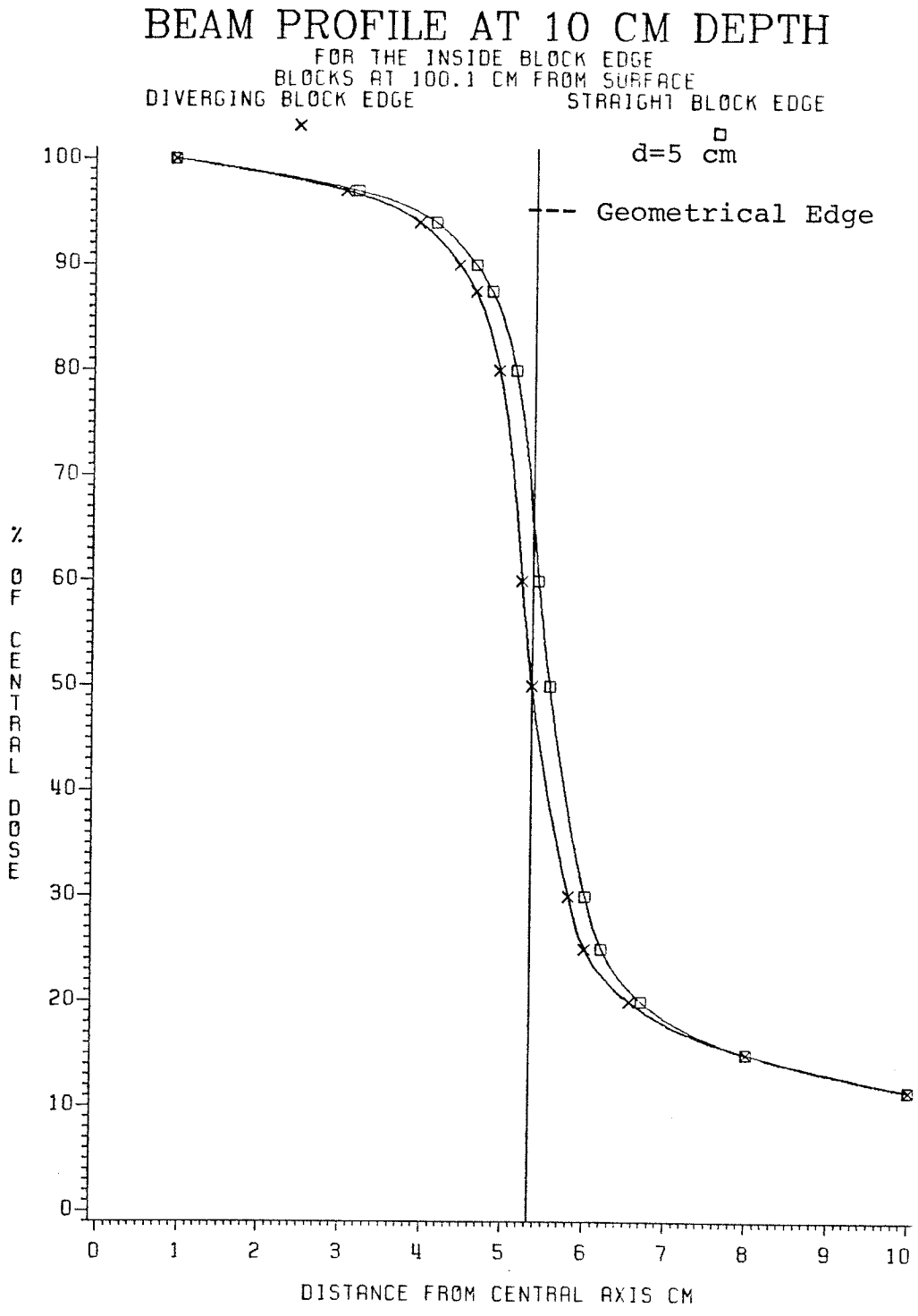
BEAM PROFILE AT 10 CM DEPTH
FOR THE INSIDE BLOCK EDGE
BLOCKS AT 100.1 CM FROM SURFACE
DIVERGING BLOCK EDGE
STRAIGHT BLOCK EDGE
d=5 cm
Geometrical Edge
% OF CENTRAL DOSE
DISTANCE FROM CENTRAL AXIS CM
100
90
80
70
60
50
40
30
20
10
0
0
1
2
3
4
5
6
7
8
9
10

Figure 7.5

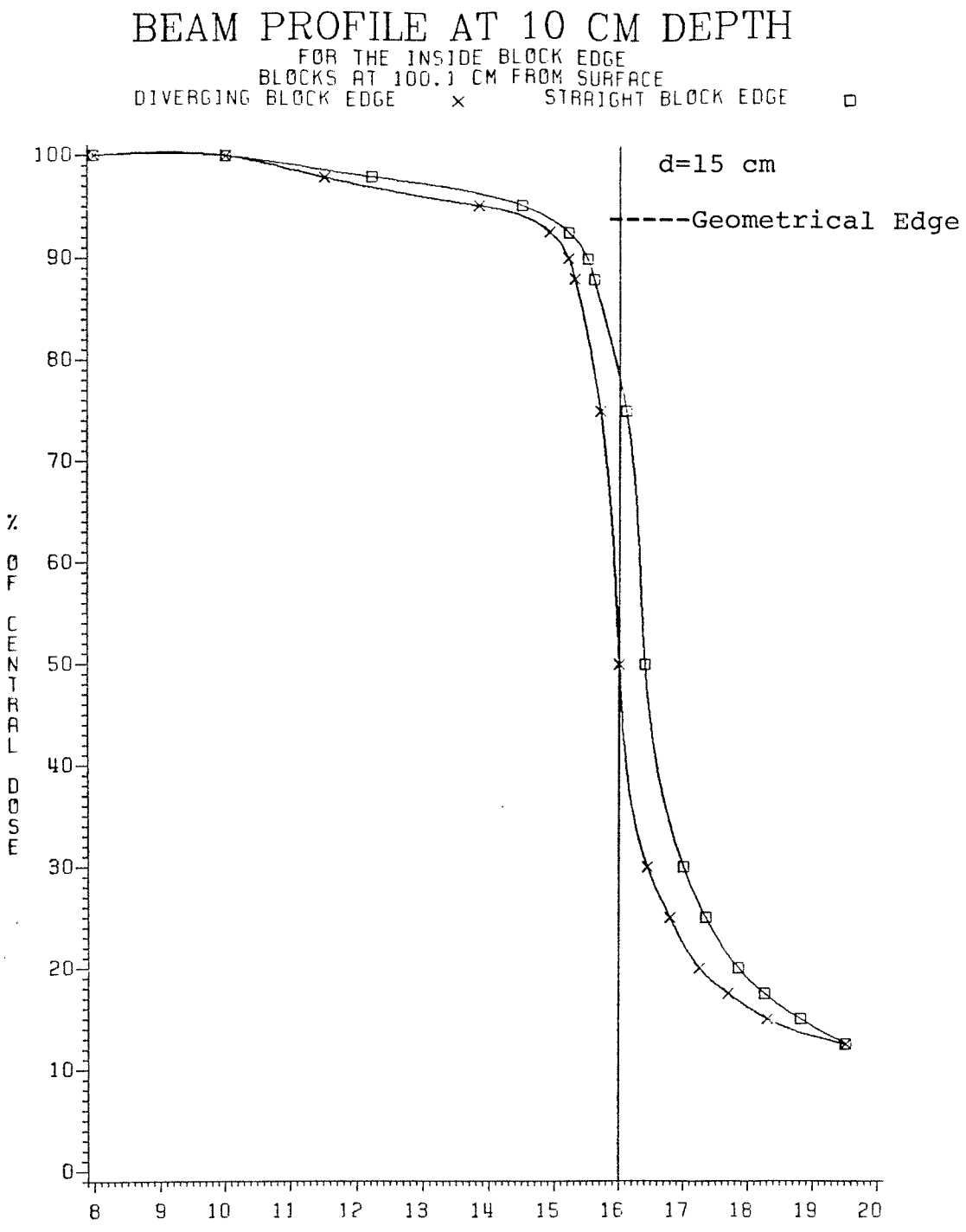
BEAM PROFILE AT 10 CM DEPTH
FOR THE INSIDE BLOCK EDGE
BLOCKS AT 100.1 CM FROM SURFACE
DIVERGING BLOCK EDGE ×
STRAIGHT BLOCK EDGE □
d=15 cm
----Geometrical Edge
% OF CENTRAL DOSE
100
90
80
70
60
50
40
30
20
10
0
8
9
10
11
12
13
14
15
16
17
18
19
20
DISTANCE FROM CENTRAL AXIS CM

Figure 7.6

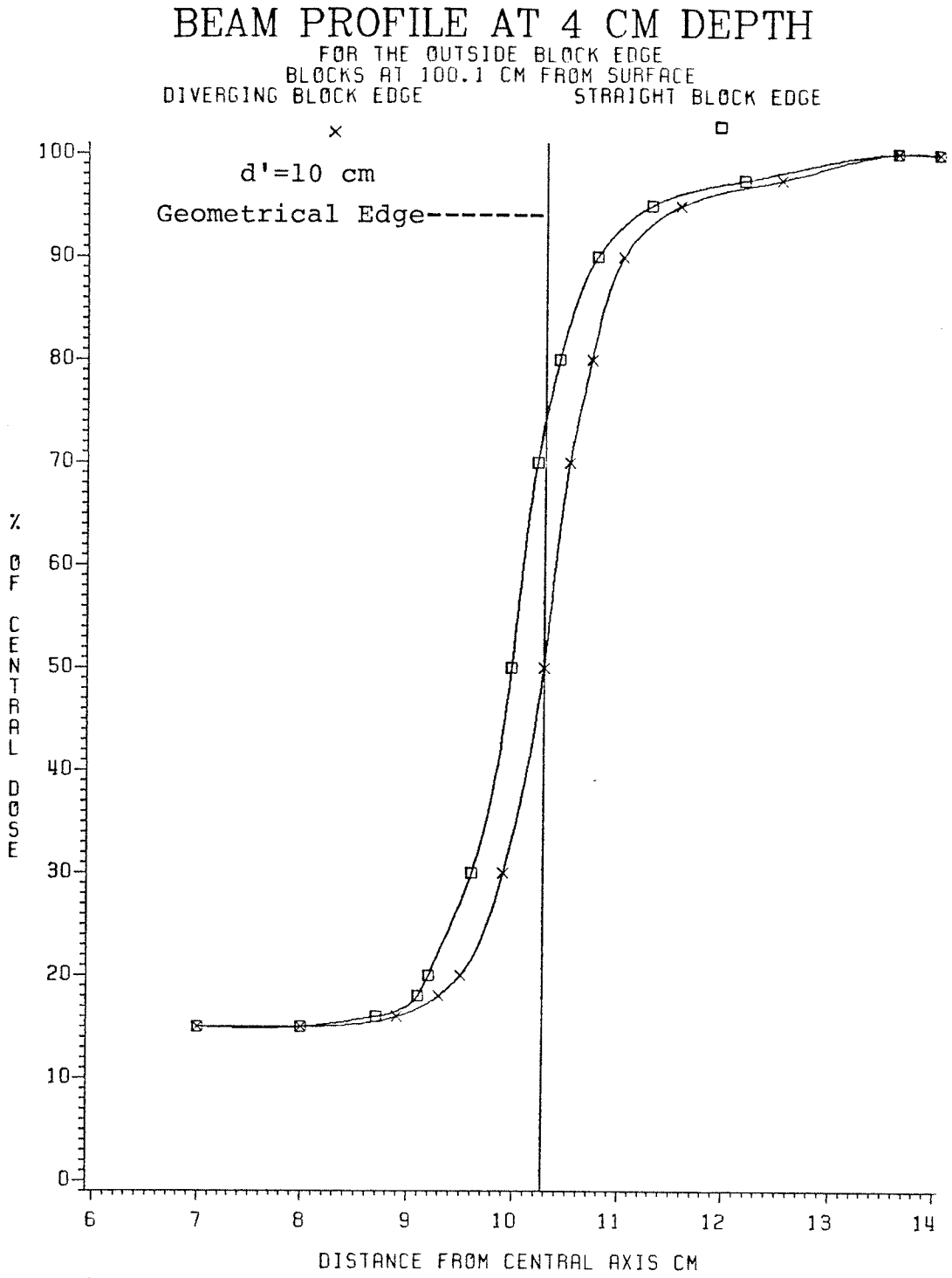
BEAM PROFILE AT 4 CM DEPTH
FOR THE OUTSIDE BLOCK EDGE
BLOCKS AT 100.1 CM FROM SURFACE
DIVERGING BLOCK EDGE
STRAIGHT BLOCK EDGE
d'=10 cm
Geometrical Edge-------
% OF CENTRAL DOSE
100
90
80
70
60
50
40
30
20
10
0
6
7
8
9
10
11
12
13
14
DISTANCE FROM CENTRAL AXIS CM

Figure 7.7

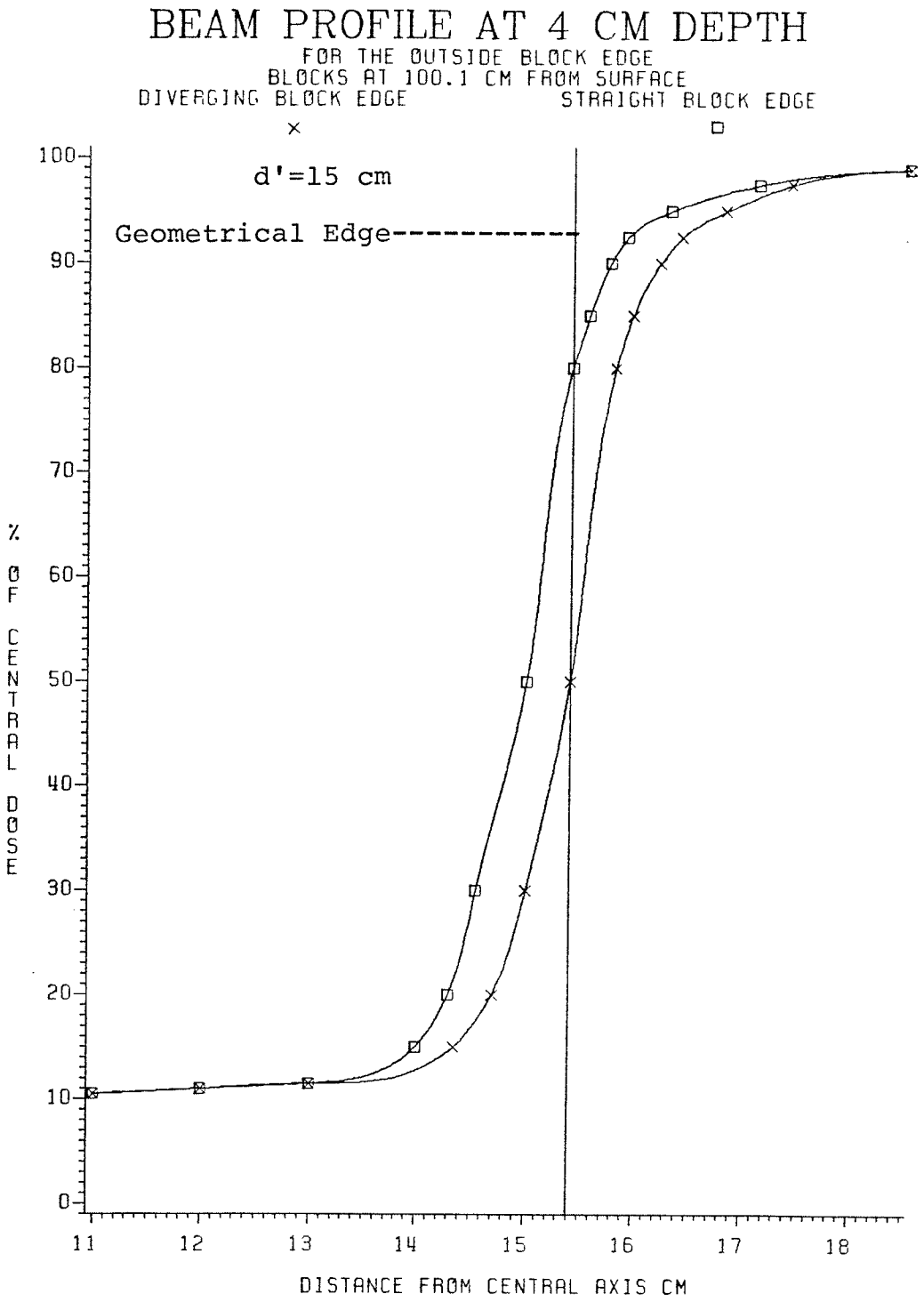
BEAM PROFILE AT 4 CM DEPTH
FOR THE OUTSIDE BLOCK EDGE
BLOCKS AT 100.1 CM FROM SURFACE
DIVERGING BLOCK EDGE
STRAIGHT BLOCK EDGE
d'=15 cm
Geometrical Edge----------
% OF CENTRAL DOSE
100
90
80
70
60
50
40
30
20
10
0
11
12
13
14
15
16
17
18
DISTANCE FROM CENTRAL AXIS CM

Figure 7.8

DIMENSION OF PENUMBRA FORMED BY INSIDE BLOCK EDGE

DISTANCE OF FIELD EDGE FROM CENTRAL AXIS AT THE PHANTOM SURFACE CM	DEPTH CM	BLOCK TO PHANTOM SURFACE DISTANCE CM	WIDTH OF 90 TO 30% DOSE CM ± .2 CM	
			BLOCK SURFACE STRAIGNT	DIVERGING
5	4	100.1	1.2	1.2
5	10	100.1	1.5	1.4
5	4	40	0.7	0.7
5	10	40	0.9	0.9
5	4	20	0.65	0.65
5	10	20	0.8	0.8
15	4	100.1	1.3	1.1
15	10	100.1	1.6	1.3
15	4	40	0.8	0.7
15	10	40	1.0	0.6
15	4	20	0.7	0.6
15	10	20	0.9	0.8

TABLE 7.1

DIMENSION OF PENUMBRA FORMED BY OUTSIDE BLOCK EDGE

DISTANCE OF FIELD EDGE FROM CENTRAL AXIS AT THE PHANTOM SURFACE CM	DEPTH CM	BLOCK TO PHANTOM SURFACE DISTANCE CM	WIDTH OF 90 TO 30% DOSE CM ± .2 CM BLOCK SURFACE STRAIGNT	DIVERGING
5	10	100.1	1.6	1.4
5	10	40	0.9	0.8
5	10	20	0.8	0.8
15	10	100.1	1.6	1.3
15	10	40	1.0	0.9
15	10	20	0.8	0.7

TABLE 7.2

diverging block edge (inside and outside). However in the case of the straight block edge a shift occurs between the geometrical edge of the beam and the 50% relative dose. This is further discussed in section 7.42.

7.42 Effect of BSD

Figures 7.9 - 7.12 show the changes in the beam profiles when the shielding blocks were moved closer to the phantom surface. At shorter BSD the dose gradient across the field edge is steeper for all measured conditions, results in smaller penumbra width. The change in penumbra width between 40 and 20 cm BSD was very small for both diverging and straight edges. In addition, the separation distance between the straight and diverging block edge profiles was smaller at shorter BSD, becoming negligible under certain conditions (Figure 7.9).

Figures 7.13 and 7.16 show the effect of BSD on the distance of the 90, 50 and 30% relative dose from the geometrical beam edge. The 50% relative dose of the diverging block edge (inside and outside) coincides with the geometrical beam edge for all BSD's used. However, in case of the straight block edge the separation distance between the 50% relative dose and the geometrical edge is seen to decrease with smaller BSD.

7.43 Calculated Beam Profiles

Figure 7.17 shows the measured and calculated beam profiles for 4 cm and 10 cm depth at 100.1 cm BSD and 150 cm SSD.

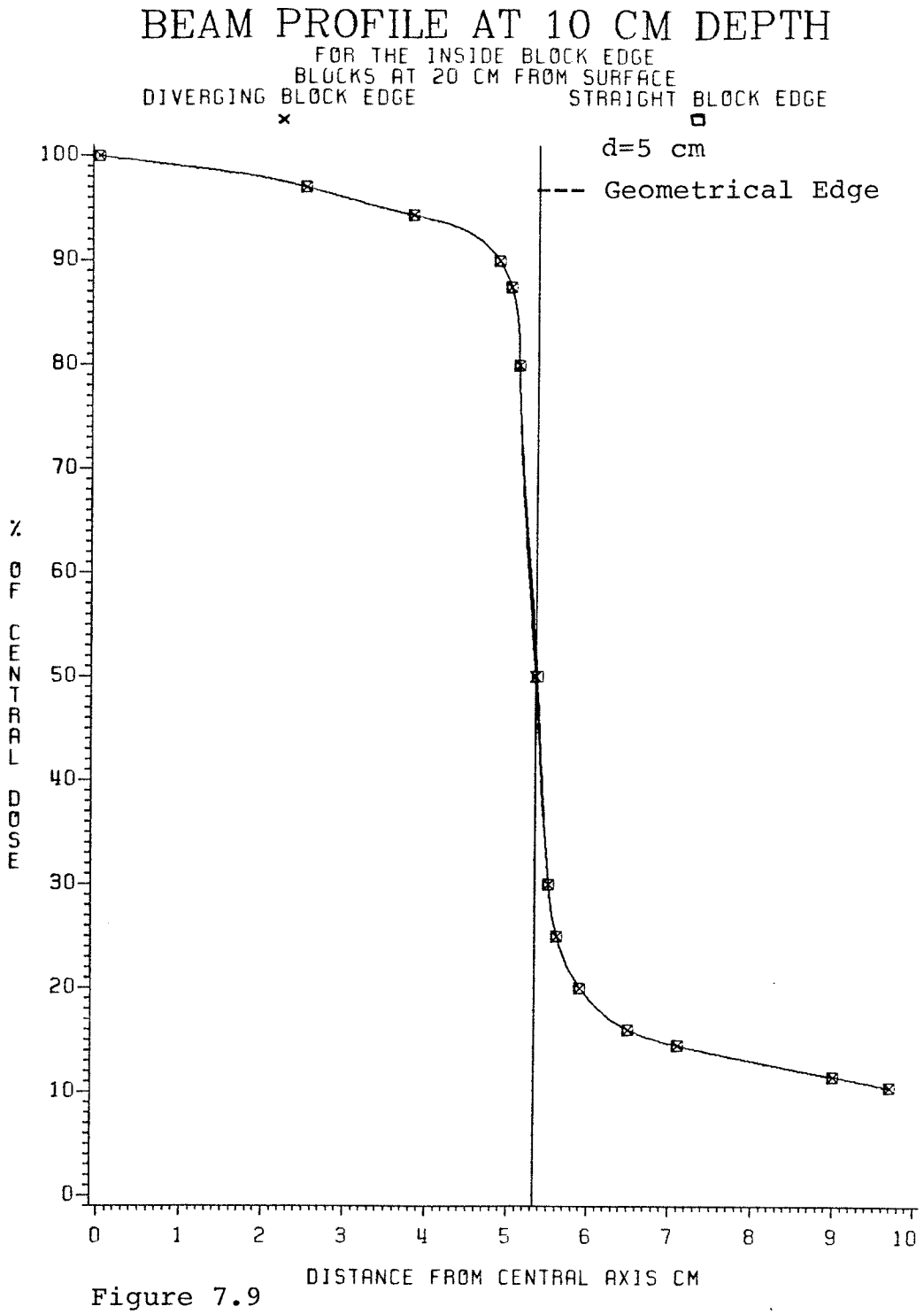
BEAM PROFILE AT 10 CM DEPTH
FOR THE INSIDE BLOCK EDGE
BLOCKS AT 20 CM FROM SURFACE
DIVERGING BLOCK EDGE
STRAIGHT BLOCK EDGE
d=5 cm
--- Geometrical Edge
% OF CENTRAL DOSE
DISTANCE FROM CENTRAL AXIS CM
0
10
20
30
40
50
60
70
80
90
100
0
1
2
3
4
5
6
7
8
9
10

Figure 7.9

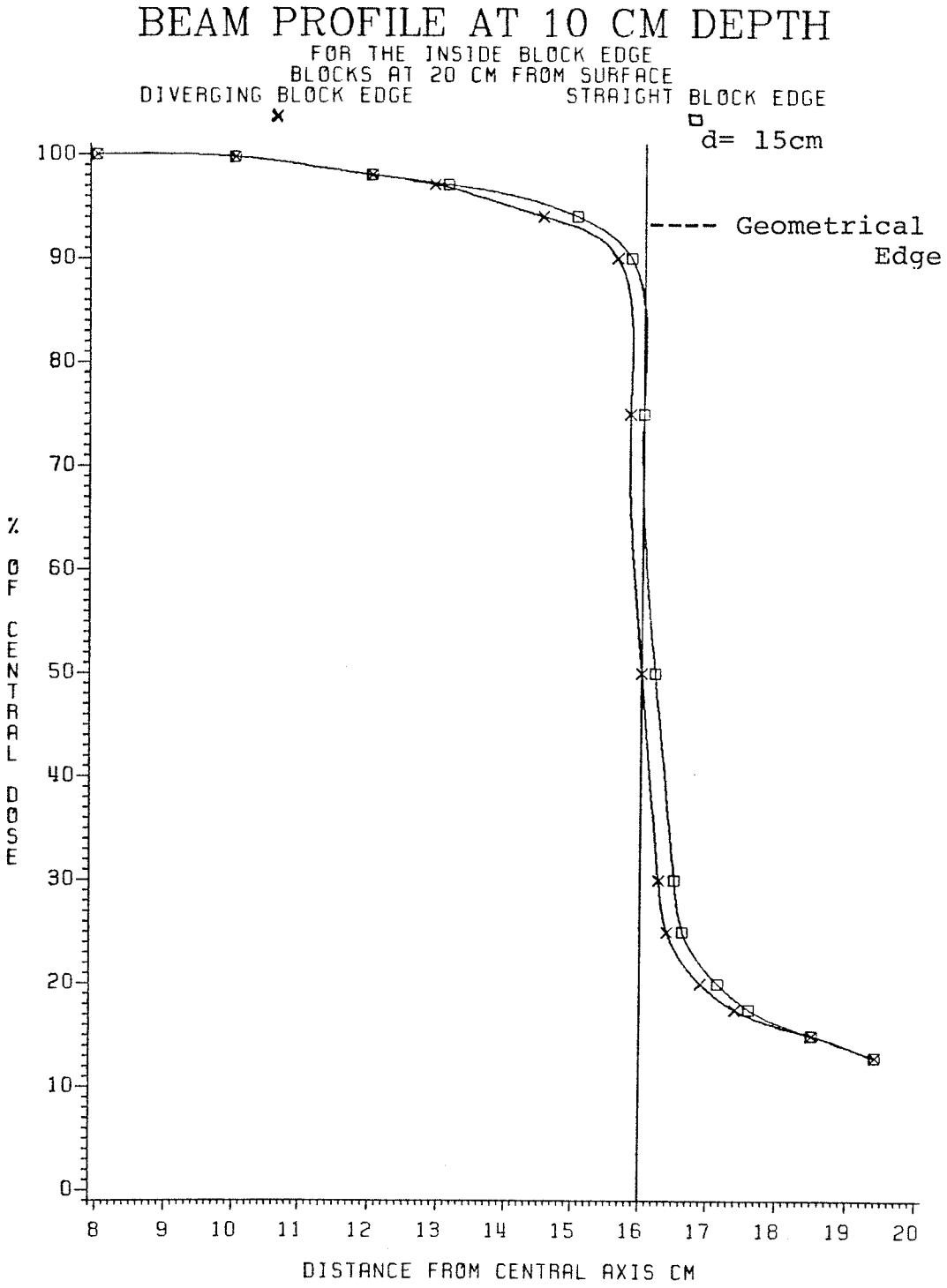
BEAM PROFILE AT 10 CM DEPTH
FOR THE INSIDE BLOCK EDGE
BLOCKS AT 20 CM FROM SURFACE
DIVERGING BLOCK EDGE
STRAIGHT BLOCK EDGE
d= 15cm
---- Geometrical Edge
% OF CENTRAL DOSE
100
90
80
70
60
50
40
30
20
10
0
8
9
10
11
12
13
14
15
16
17
18
19
20
DISTANCE FROM CENTRAL AXIS CM

Figure 7.10

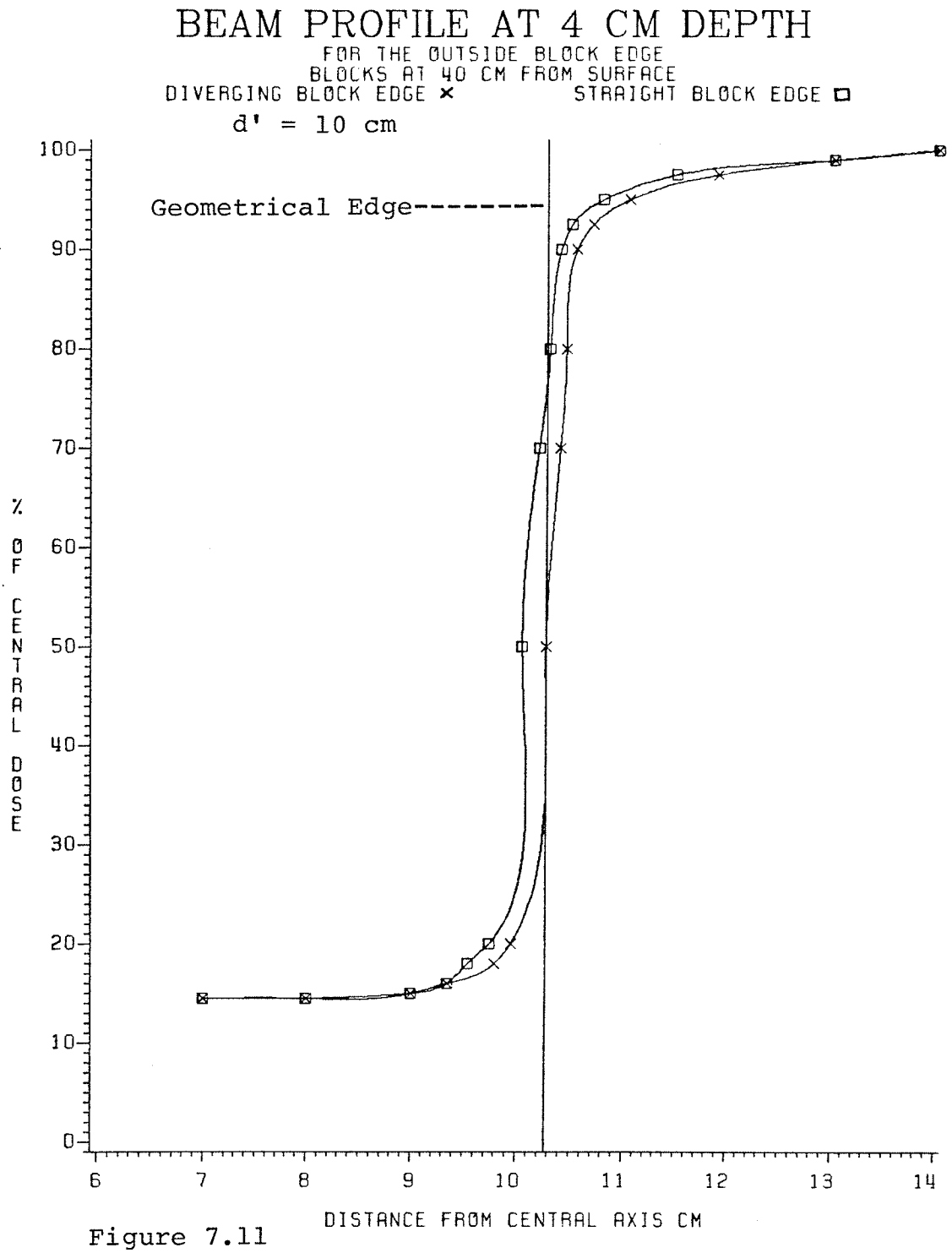
BEAM PROFILE AT 4 CM DEPTH
FOR THE OUTSIDE BLOCK EDGE
BLOCKS AT 40 CM FROM SURFACE
DIVERGING BLOCK EDGE ×
STRAIGHT BLOCK EDGE □
d' = 10 cm
Geometrical Edge--------
% OF CENTRAL DOSE
100
90
80
70
60
50
40
30
20
10
0
6
7
8
9
10
11
12
13
14
DISTANCE FROM CENTRAL AXIS CM

Figure 7.11

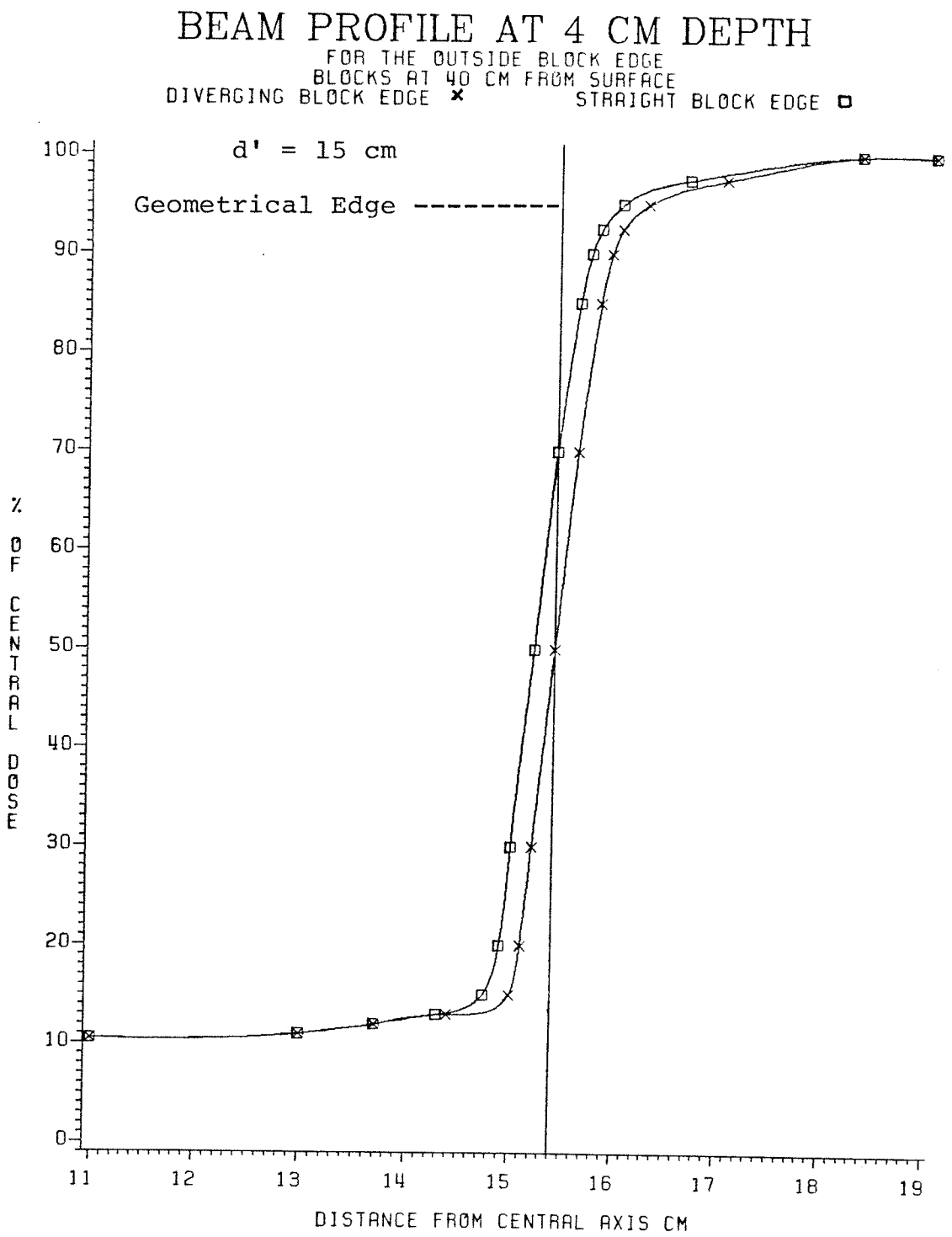
BEAM PROFILE AT 4 CM DEPTH
FOR THE OUTSIDE BLOCK EDGE
BLOCKS AT 40 CM FROM SURFACE
DIVERGING BLOCK EDGE ×
STRAIGHT BLOCK EDGE □
d' = 15 cm
Geometrical Edge ---------
% OF CENTRAL DOSE
100
90
80
70
60
50
40
30
20
10
0
11
12
13
14
15
16
17
18
19
DISTANCE FROM CENTRAL AXIS CM

Figure 7.12

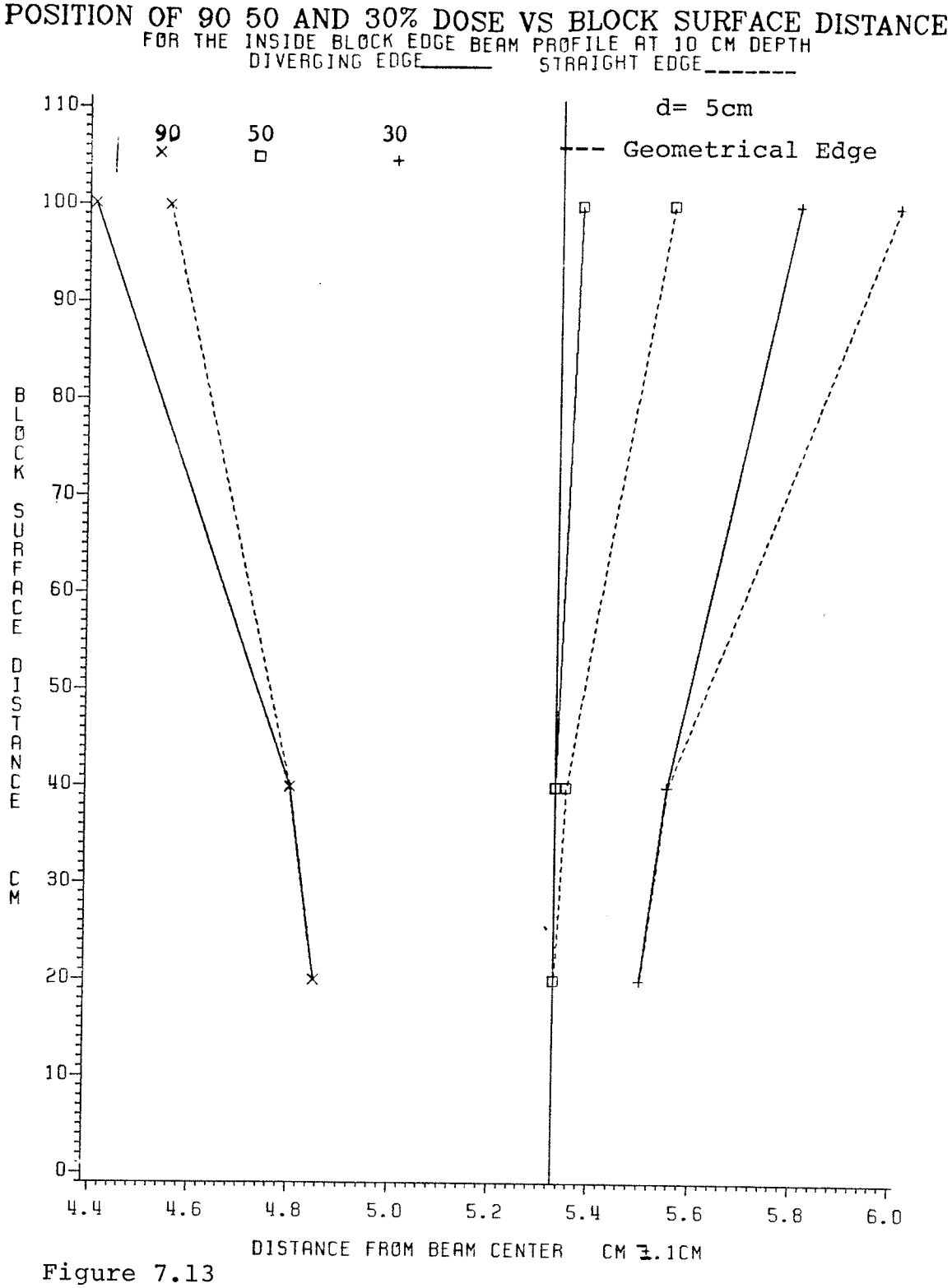
POSITION OF 90 50 AND 30% DOSE VS BLOCK SURFACE DISTANCE
FOR THE INSIDE BLOCK EDGE BEAM PROFILE AT 10 CM DEPTH
DIVERGING EDGE_____ STRAIGHT EDGE_____
d= 5cm
--- Geometrical Edge
90
50
30
BLOCK SURFACE DISTANCE CM
110
100
90
80
70
60
50
40
30
20
10
0
4.4
4.6
4.8
5.0
5.2
5.4
5.6
5.8
6.0
DISTANCE FROM BEAM CENTER CM 5.1CM

Figure 7.13

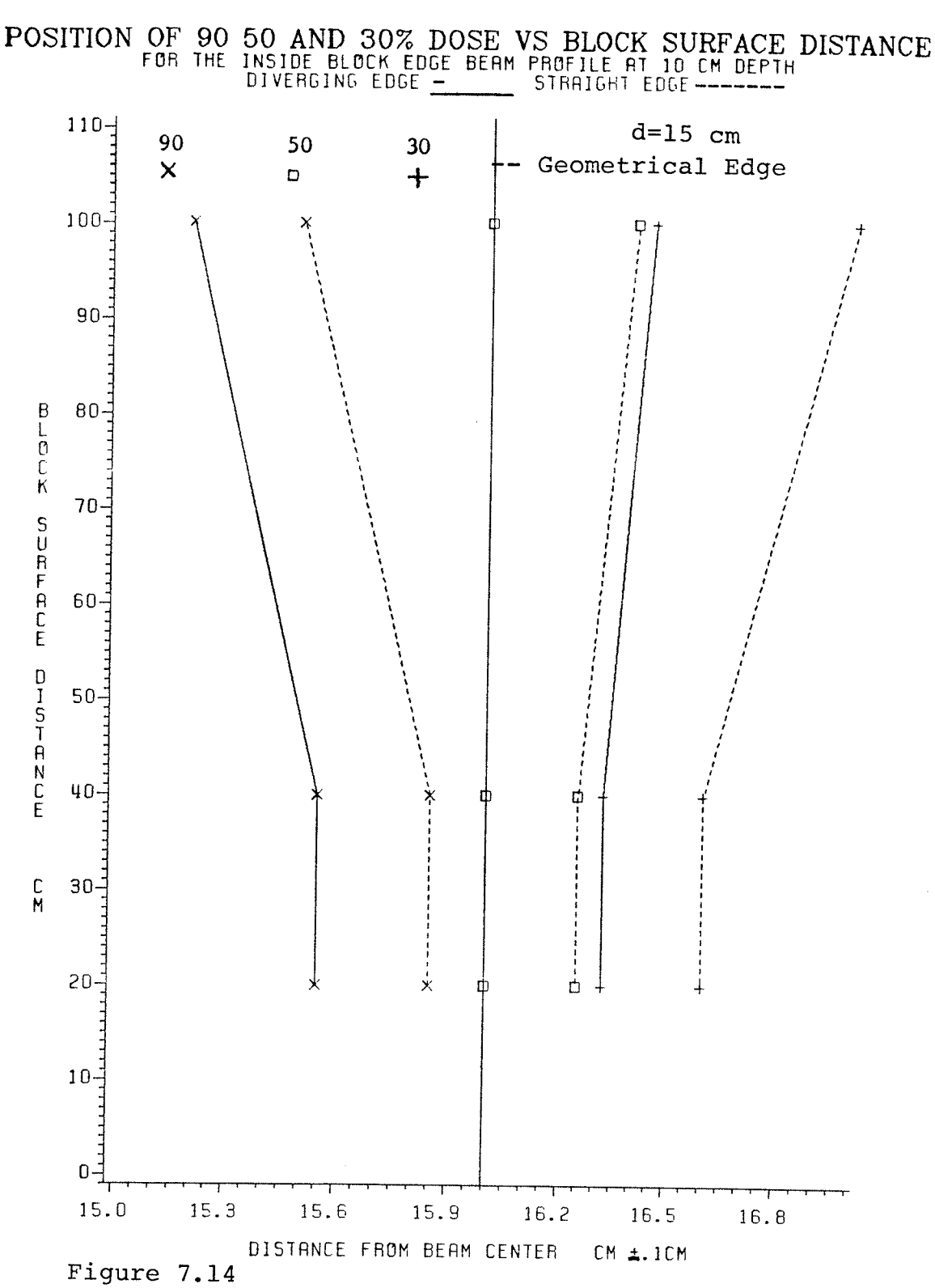
POSITION OF 90 50 AND 30% DOSE VS BLOCK SURFACE DISTANCE
FOR THE INSIDE BLOCK EDGE BEAM PROFILE AT 10 CM DEPTH
DIVERGING EDGE ——— STRAIGHT EDGE -------
90
50
30
d=15 cm
Geometrical Edge
BLOCK SURFACE DISTANCE CM
110
100
90
80
70
60
50
40
30
20
10
0
15.0
15.3
15.6
15.9
16.2
16.5
16.8
DISTANCE FROM BEAM CENTER CM ±.1CM

Figure 7.14

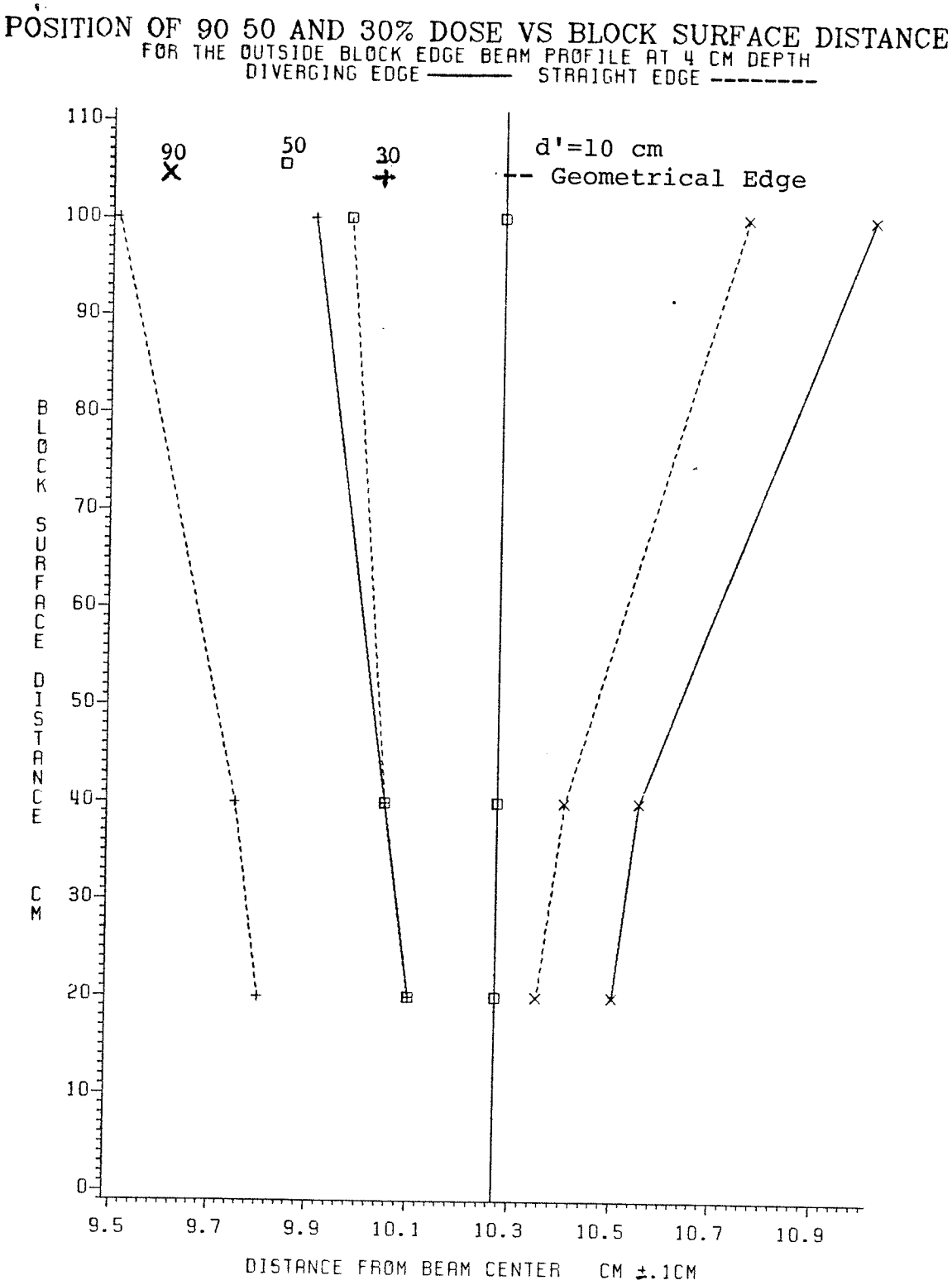
POSITION OF 90 50 AND 30% DOSE VS BLOCK SURFACE DISTANCE
FOR THE OUTSIDE BLOCK EDGE BEAM PROFILE AT 4 CM DEPTH
DIVERGING EDGE ——— STRAIGHT EDGE --------
90
50
30
d'=10 cm
-- Geometrical Edge
BLOCK SURFACE DISTANCE CM
110
100
90
80
70
60
50
40
30
20
10
0
9.5
9.7
9.9
10.1
10.3
10.5
10.7
10.9
DISTANCE FROM BEAM CENTER CM ±.1CM

Figure 7.15

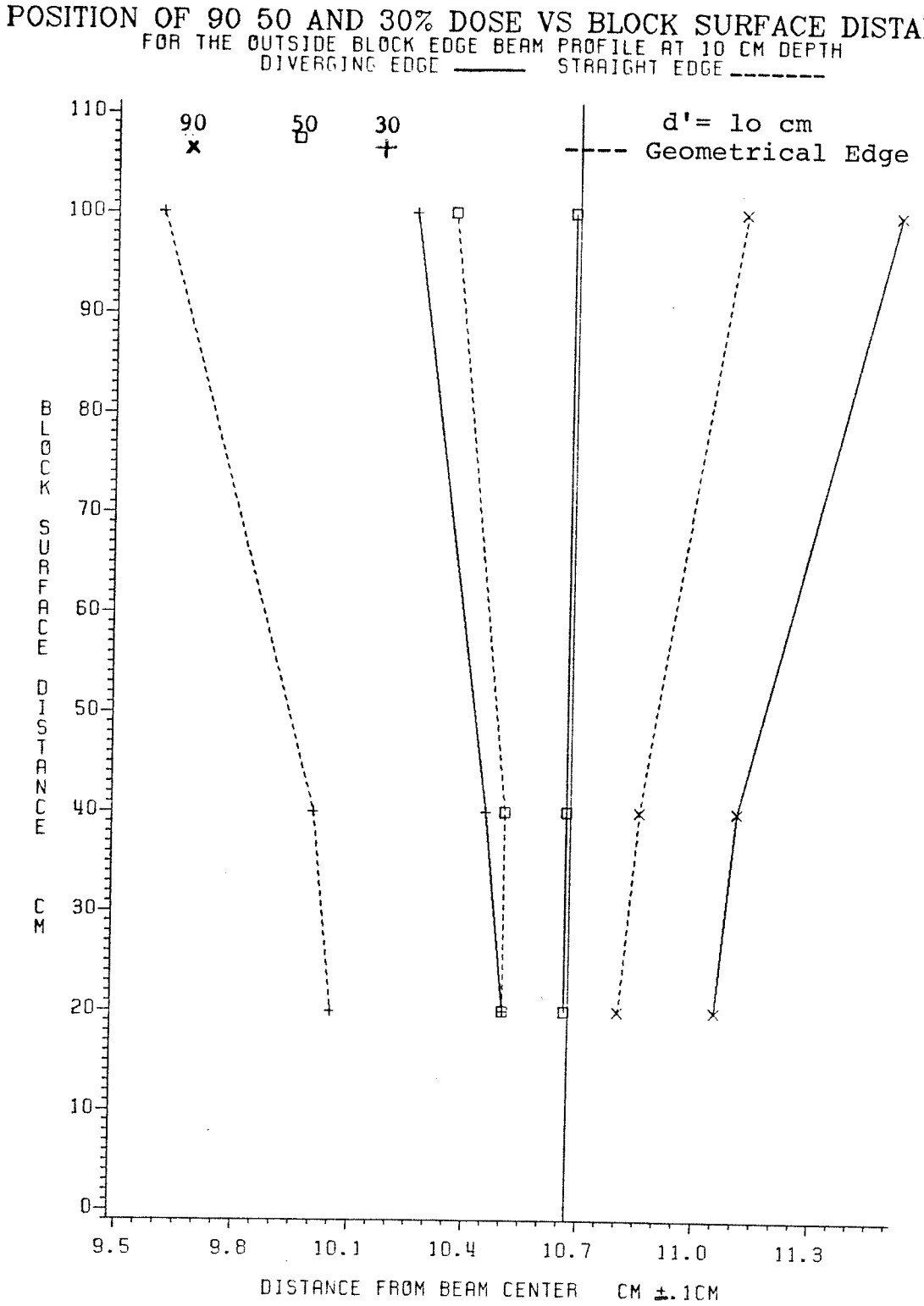
POSITION OF 90 50 AND 30% DOSE VS BLOCK SURFACE DISTANCE
FOR THE OUTSIDE BLOCK EDGE BEAM PROFILE AT 10 CM DEPTH
DIVERGING EDGE ——— STRAIGHT EDGE -------
90
50
30
d'= lo cm
--- Geometrical Edge
BLOCK SURFACE DISTANCE CM
110
100
90
80
70
60
50
40
30
20
10
0
9.5
9.8
10.1
10.4
10.7
11.0
11.3
DISTANCE FROM BEAM CENTER CM ±.1CM

Figure 7.16

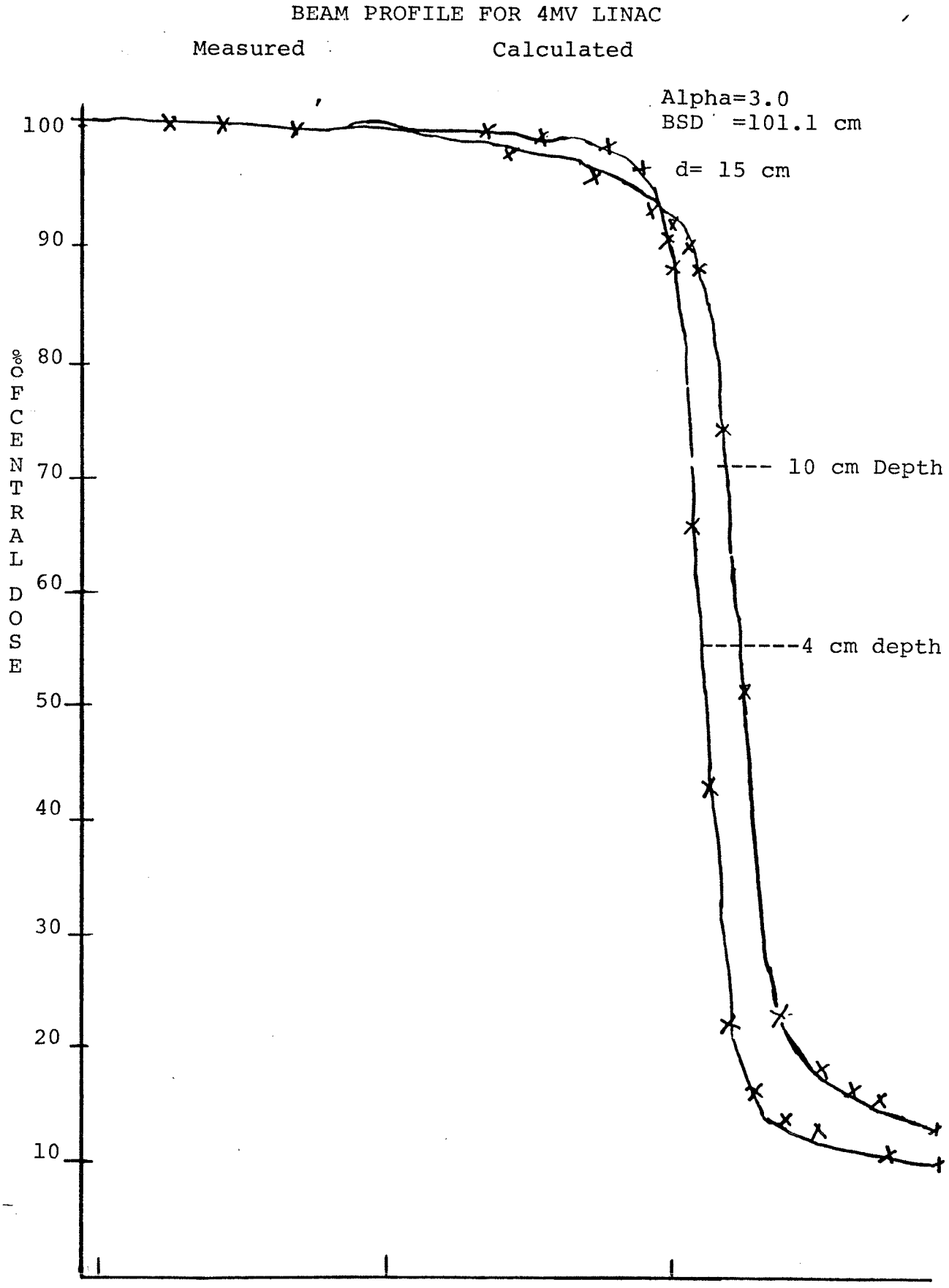
BEAM PROFILE FOR 4MV LINAC
Measured
Calculated
Alpha=3.0
BSD =101.1 cm
d= 15 cm
--- 10 cm Depth
-------4 cm depth
%OF CENTRAL DOSE
100
90
80
70
60
50
40
30
20
10
5
10
15
Distance From Central Axis
(cm)

Figure 7.17

diverging block edge (inside and outside). However in the case of the straight block edge a shift occurs between the geometrical edge of the beam and the 50% relative dose. This is further discussed in section 7.42.

7.42 Effect of BSD

Figures 7.9 - 7.12 show the changes in the beam profiles when the shielding blocks were moved closer to the phantom surface. At shorter BSD the dose gradient across the field edge is steeper for all measured conditions, results in smaller penumbra width. The change in penumbra width between 40 and 20 cm BSD was very small for both diverging and straight edges. In addition, the separation distance between the straight and diverging block edge profiles was smaller at shorter BSD, becoming negligible under certain conditions (Figure 7.9).

Figures 7.13 and 7.16 show the effect of BSD on the distance of the 90, 50 and 30% relative dose from the geometrical beam edge. The 50% relative dose of the diverging block edge (inside and outside) coincides with the geometrical beam edge for all BSD's used. However, in case of the straight block edge the separation distance between the 50% relative dose and the geometrical edge is seen to decrease with smaller BSD.

7.43 Calculated Beam Profiles

Figure 7.17 shows the measured and calculated beam profiles for 4 cm and 10 cm depth at 100.1 cm BSD and 150 cm SSD.

variations in BSD and consequently an error in the values of the geometrical penumbra 'P' (see equ. 7.0) is introduced. This in turn results in dose calculation errors across the field edge. To overcome this problem, the alpha values were changed to account for the various BSD. Table 7.3 presents the value of alpha necessary to predict the measured profiles for the lead blocks at the BSD used.

7.5 DISCUSSION

(i) The dominant factor affecting penumbra size is the block skin distance (BSD). The shape of the block edge has no significant effect.

(ii) The major effect of the block edge shape is in determining the position of the 50% dose level relative to the geometrical edge of the field, as a result of the increased transmission that occurs for the straight edge.

(iii) The widely accepted concept that diverging edge lead blocks at large BSD produce smaller penumbra than a straight edge lead blocks at shorter BSD is shown to be unfounded. Therefore a straight edged block may be used for shielding, simplifying the production of these blocks.

(iv) Minimum penumbra width, formed by lead shielding blocks in large irregular fields, can be achieved by placing the blocks on a bridge at short BSD. However, this will result in an increased skin dose and decreased skin sparing effect.

In order to optimize the shielding parameters, the bridge must

be placed at the greatest distance from the skin possible while still maintaining a small penumbra width. It can be concluded from the measured data that the appropriate bridge-to-skin distance lies between 30 and 40 cm. Between these distances the penumbra width is small and varies only slightly with BSD. At this BSD, even for large field size, the surface dose does not increase by more than 10% over that of the open beam when a lead acrylic bridge or a lead glass filter is used. Where for acrylic the surface dose is increased up to 21% over the open beam values (figures 5.13).

Alpha Values for Varying BSD

BSD (cm)	Alpha
100.1	3
40	8
20	10

TABLE 7.3

Chapter 8. Conclusions

(i) The effectiveness of lead acrylic as an electron filter has been demonstrated for a 4MV photon beam. It has been shown to be less effective than lead glass for reducing doses at the surface and in the build-up region but far superior to acrylic. Lead glass is a brittle material, whereas lead acrylic is transparent, machinable and exhibits a structural strength comparable with acrylic. These properties of lead acrylic make it possible to combine the dual functions of electron filter and shadow tray (or bridge).

For small and moderate field sizes a lead acrylic tray placed at the appropriate tray to skin distance, will produce superior build-up curves than open beam conditions. For large field sizes similar build-up curves to open beam conditions can be achieved at shorter tray to skin distance than acrylic.

(ii) The magnitude of scatter radiation from acrylic and lead acrylic supporting trays outside the field boundary has been found to be dependent on field size, tray to surface distance, tray thickness, depth in phantom and distance from field boundary. For some tray thicknesses, an acrylic tray has been observed to elevate the dose, on the surface and at shallow depth, outside field boundary to greater levels than lead acrylic. The contribution of the scattered radiation from the tray to the patient's eyes outside a typical mantle field may be clinically significant. This risk can be reduced by simply applying an external lead shield a few millimeters thick, during the patient treatment.

(iii) The penumbra formed by the edge of lead blocks used for shielding in large irregular fields has been investigated for various parameters. These include, block edge shape, block-skin distance and distance of block edge from central axis. The dominant factor affecting penumbra size has been shown to be the block-skin distance. The major effect of the block edge shape is in determining the position of the 50% dose level relative to the geometrical edge. These findings contradict the widely accepted concept that diverging edge lead blocks produce smaller penumbra at large BSD than a straight edge lead block placed at shorter BSD. Consequently a straight edge block may be used for shielding simplifying the production of these blocks.

The requirement of small penumbra width during treatment with a large irregular field can be satisfied by placing the bridge supporting the lead blocks closer to the patient surface. The optimum bridge to patient surface distance has been determined to lie between 30 and 40 cm. Between these distances the penumbra width is small and varies only slightly with BSD. With the lead acrylic bridge so positioned and for any field size, the surface dose does not exceed the open beam values by more than 10%.

References

AM. Ames T.E., Saylor W. and Dillard M.,INT. J. Radiat. Oncol. Bio. and phys. 2, 1027 (1977)

AT. ATTIX F.H., Lopez, S. Owolabig and Paliwol B.R., Med. Phys 10, 301 (1983).

BH. Bhatnagar J.P., Brit. J. Radiol. 50, 449 (1977).

BI. Biggs P.J. and Ling C.C., Med. Phys. 6, 291 (1979)

CA. Cameron, J.R., Sun Maralingam N. and Kenny G.N. Thermoluminescent Dosimetry Uni. of Wisconsin Press (1968).

CAI. Cameron J. R., Zimmerman D., Kenny G., Buch R., Bland R. and Grant R., Health Phys, 10, 25 (1964)

CH. Charles M. W. and Brown N., Phys. Med. Biol. 20, 202 (1975)

EV. Evans R.D., X-Ray and -Ray Interactions in Radiation Dosimetry, ATTIX, Vol 1, Academic Press 1968

GR. Gray L. Radiology 109, 437 (1973).

HI. Hine G.J., Phys. Rev. 82, 755, (1951)

HI1. Hine G.J. and Brownell G.L. 'Radiation Dosimetry', Academic Press (1956).

HO. Howarth J.L., Jones J.L. and Miller H., Br. J. Radiol. 24 665 (1951).

HOR. Horowitz Y.S. Phy. Med. Biol., 26, 765 (1981).

HU. Hubbell J.H., 'Photon cross sections attenuation coefficients and energy absorption coefficients from 10 KeV to 100 GeV' NSRD - NBS 29. Washington, D.C. (1969).

HUA. Huang D.H., Kase, K.R. and Bjarngard B.E., Med. Phys. 8, 368 (1981)

IB. Ibbott G.S. and Hendee W.R. Am. J. Roet. 108, 168 (1970)

IC. ICRU Report 33 (1980)

IC1. ICRU Report 14 (1969)

IC2. ICRU Report 23 (1973)

JA. Jackson W., Br. J. Radiol. 44 109, (1971).

JO. Johns H.E. and Cunningham J.R. 'The Physics of Radiology', C.C. Thomas, (1966).

JO1. Johns H.E. and Cunningham J.R., 'The Physics of Radiology' C.C. Thomas, (1982).

JO2. Johns, H.E., Cormack D.V. and Fedoruk S.O., Br. J. Radiol., 25, 302 (1952).

LE. Leung D.M.K. and Johns H.E., Med. Phys. 4, 441 (1977)

LI. Ling C.C., Schell M.C. and Rustgi S.N. Med. Phys. 9, 20 (1982)

MAR. Marks J.E., Haus A.G., Sutton H.G. and Griem M.L., Cancer 34, 83 (1974).

MA. Marbach J.R. and Almond P.R. Med Phys. 4, 310 (1977)

NI. Nilsson B.O. and Brahme A., Phys. Med. Biol. 24, 401 (1979).

PA. Padikal P.A. and Deye J.A., Phys. Med. Biol. 23, 1086, (1978)

PA. Pages L., Bertel E., Joffre H. and Sklavenihs L. Atomic Data 4, 1 (1972).

PU. Purser P.R., Phys. Med. Biol. 16, 700 (1971).

RA. Rao P.J., Pillai K. and Gregg E.C., Am. J. Roent. 117, 168, (1973).

SC. Scrimger J.W., Radiology 105, 421 (1972)

SC. Scrimger J.W. and Kolitsi Z., Radiology 130, 233 (1979)

SM. Smith C.W. and Sutherland W.H., Br. J. Radiol, 49 562 (1976).

TH. Theraplan Computer Manual, A.E.C.L.

VE. Velkley D.E., Manso D.J., Purdy J.A. and Oliver G.R. Jr., Med. Phys 2, 14 (1975)

WE. Webb G.A.M., Health Physics 13, 814 (1967).

WH. White D.R., Med. Phys. 5, 467 (1978).

WHI. Whitton J., Health Physics, 24 1, (1973).

Appendix

1. Annealing Procedure for LiF-100

The TLDs were placed in an aluminum tray and the following annealing procedure was used:

(i) Pre-irradiation anneal at 400° for 1 hour followed by 100°C for two hours and then cool at room temperature. Post-irradiation anneal at 100°C for 10 minutes and cool at room temperature prior to readout.

The high temperature anneal restores the original TLD characteristics by erasing accumulated radiation effects.

The lower temperature pre and post irradiation anneal reduce the low temperature peaks to a negligible level (CA.) compared to the more table dosimetric peaks. By this means, fading of the TLD's response with time is minimal.

The 400°C and 100°C anneals were performed in Huppert's Deluxe (model 4396) and Precision Scientific furnaces respectdively. All the TL dosimeters were read on a Harshaw 2000 (A & B) reader system.

2. Annealing Procedure for LiF-Teflon Discs

The annealing procedure previously described cannot be used for the LiF-Teflon dosimeters due to the low melting point of Teflon. To overcome this problem an alternative annealing was used. This procedure is described as follows: (WE.):

a) Pre-irradiation anneal at 300°C for 15 minutes followed by two hours at 80°C.

b) Post-irradiation anneal at 100° for 5 minutes. This

annealing procedure is successful in restoring the original background reading and sensitivity of Teflon disc dosimeters after irradiation in the range .03 cGy to 30 cGy (WE.).